DEVELOPMENT OF LIGHTWEIGHT, COMPACT, STRUCTURALLY-INTEGRATED ACOUSTIC LINERS FOR BROADBAND LOW-FREQUENCY NOISE MITIGATION

By

ANDREW T. CHAMBERS

Bachelor of Science in Mechanical Engineering

Oklahoma State University

Stillwater, OK

2015

Submitted to the Faculty of the
Graduate College of the
Oklahoma State University
in partial fulfillment of
the requirements for
the Degree of
MASTER OF SCIENCE
May, 2017

DEVELOPMENT OF LIGHTWEIGHT, COMPACT, STRUCTURALLY-INTEGRATED ACOUSTIC LINERS FOR BROADBAND LOW-FREQUENCY NOISE MITIGATION

Thesis Approved:

Dr. James M. Manimala

Thesis Adviser

Dr. Richard J. Gaeta

Dr. Andrew S. Arena Jr.

ACKNOWLEDGEMENTS

First, I would like to acknowledge the support for this research provided by the Oklahoma Center for the Advancement of Science and Technology's (OCAST) OARS Grant No. AR-15-070.

The work done for this thesis was conducted under the guidance and supervision of Dr. James Manimala. I would like to thank Dr. Manimala for his support and patience throughout the entirety of this project. His knowledge and experience with acoustics along with the administrative aspects of conducting research was vital to my success in completing this work. I am thankful for the opportunity to learn and study under the tutelage of Dr. Manimala.

I would like to thank Dr. Gaeta for teaching me the fundamentals of acoustics and providing valuable resources for the literature review portion of this thesis. I would also like to thank Dr. Arena for being a part of my defense committee.

I would like to thank Dr. Good for encouraging me to pursue a Master's degree at Oklahoma State University, and for teaching me the intricacies of Finite Element Analysis. I would also like to thank Dr. Kidd and Dr. Jin for their support, and for teaching me valuable knowledge that will be useful throughout my engineering career.

Special thanks to Michael Jones for providing valuable insight and resources throughout this research. Also for allowing me to utilize the NASA Langley Liner Technology Facility to test my designs. I am also thankful to Brian Howerton, Martha Brown, and Larry Becker for their help conducting experiments at NASA. It was a pleasure learning from and working with the best acoustic liner people in the world.

I would also like to express sincere thanks to my colleagues at Oklahoma State University. Thanks to Alexander Svetgoff, Ryan Aiken, and Miklyas Afework for their work with ensuring the accuracy and consistency of the 3D printing process. Special thanks to Alexander for his help with the many experiments conducted in the impedance tube. Thanks to Anuj Rekhy for being willing and able to help with many experimental and acoustic related questions. Anuj was a tremendous help to me throughout the work conducted for this thesis. I would also like to thank Prateek Kulkarni and Dr. Jeff Callicoat for their help with my research as well.

Lastly, I would like to express gratitude to my family. Without the support and love from you all, none of this would have been possible.

Name: ANDREW T. CHAMBERS

Date of Degree: MAY, 2017

Title of Study: DEVELOPMENT OF LIGHTWEIGHT, COMPACT, STRUCTURALLY-INTEGRATED ACOUSTIC LINERS FOR BROADBAND LOW-FREQUENCY NOISE MITIGATION

Major Field: MECHANICAL AND AEROSPACE ENGINEERING

Airborne noise with a low dominant frequency content (<~500 Hz) has detrimental effects in many applications, but is as yet beyond the scope of conventional acoustic noise mitigation techniques using liners, foams or claddings owing to mass and volume considerations. Its low evanescence contributes significantly to environmental noise pollution, and unwanted structural vibrations causing diminished efficiency, comfort, payload integrity and mission capabilities. An alternative approach using liner configurations with realistic mass and volume constraints having innovative 'folded' core geometries is investigated to ascertain its low-frequency noise absorption characteristics. In contrast to mass-driven approaches, the folded core approach relies on tailoring interactions between acoustic resonances to tune the liner's impedance to suit the dominant low-frequency content of the source. This allows to keep non-structural mass-addition to a minimum, while retaining an overall thickness comparable to conventional liners for these low-frequency liner designs. The relative acoustic performance of various candidate folded core designs is evaluated by means of a new composite metric termed the Low-Frequency Performance (LFP) factor, which is educed from the absorption coefficient spectrum obtained using Zwikker-Kosten Transmission Line (ZKTL) theory-based numerical studies. An LFP-based software tool is developed to determine optimal 3D cavity packing for a prescribed liner volume and target frequency range. ZKTL-based parametric studies on core dimensions and face sheet porosity are utilized for detailed design of test articles. Experimental verification of absorption coefficient spectra conducted using 3D printed test articles in a normal incidence acoustic impedance tube yield good correlation with simulations. More than 100 Hz of continuous bandwidth with an absorption coefficient greater than 0.6 is shown to be possible in the 300 to 400 Hz range with a 38.1-mm (1.5-inch) thick liner. Further, the influence of face sheet type, Mach number, and sound pressure level on the attenuation across folded core liners is evaluated using grazing flow impedance tube tests. Up to 20 dB of attenuation is observed in the targeted frequency range in these tests indicating potential for performance retention in an operational scenario. With current additive and hybrid manufacturing techniques attaining critical commercial maturity, lightweight and compact acoustic liners employing folded cores could provide a promising practical solution to mitigate low-frequency airborne noise, especially in aerospace applications.

TABLE OF CONTENTS

Chapter Page

LIST OF TABLES

Table Page

LIST OF FIGURES

Figure Page

SYMBOLS AND ABBREVIATIONS

α	Absorption Coefficient
A_l	Surface Area of Liner
β	Bandwidth of Absorption
β_c	Individual Channel Admittance
β_t	Total Admittance
c	Speed of Sound
d	Resonator Neck Diameter
d_c	Cavity Diameter
EPNdB	Effective Perceived Noise in Decibels
f	Frequency
Δf	Frequency Increment
FRF	Frequency Response Function
g	Distance from Liner Face to Microphone
Γ	Propagation Constant
h_o	Overall Liner Height
H_{1r} ; H_{2r} ; H_{1i} ; H_{2i}	Real (r) and Imaginary (i) Part of the FRF
H_{11} ; H_{22}	Complex form of the FRF
J_0; J_2	Bessel Function of the First Kind
k	Free-Space Wave Number
K_{bar}	Reduced Frequency
L	Resonator Neck Length
L'	Resonator Effective Neck Length
l_c	Cavity Length

LFP	Low-frequency Performance Factor
λ	Wavelength
M	Peak Absorption Coefficient
μ	Coefficient of Viscosity
n_c	Number of Cavities
p_n; p_{n+1}	Acoustic Pressure
ρ	Density
R	Acoustic Resistance
RC	Reflection Coefficient
s	Shear Wave Number (Stokes Number)
S	Resonator Neck Area
σ	Square Root of Prandtl Number
σ_c	Porosity
t_{ij}	Forward Transmission Matrix Variables
t_w	Internal Wall Thickness
u_n; u_{n+1}	Particle Velocity
γ	Specific Heat Ratio
V	Resonator Cavity Volume
ω	Angular Frequency
X	Acoustic Reactance
z_c	Characteristic Impedance
z_{tot}	Total Impedance
ζ	Lower Bound of the Bandwidth of Absorption

CHAPTER 1

INTRODUCTION

1.1 Motivation

Airborne noise with a dominant low-frequency content can have detrimental effects in many applications. Low-frequency noise can excite structural vibration modes, causing increased fatigue and even catastrophic failure. It can cause discomfort to passengers on commercial and military aircraft, and could lead to hearing impairment or psychological problems. Low-frequency noise can restrict military mission capabilities when stealth is essential to the success of the mission. It can also negatively affect payload integrity as well as cause interference with sensitive electronic equipment. Environmental noise pollution is another major issue when considering the problems caused by low-frequency noise. These problems have led organizations such as the Environmental Protection Agency (EPA) [1], European Environment Agency (EEA) [2], and the Federal Aviation Administration (FAA) [3] to impose strict noise emission regulations on a variety of machines such as road work equipment, trains, and perhaps most notably, aircraft.

One of the most common ways to mitigate airborne noise is through the use of acoustic liners. They are used extensively in aircraft engine inlet and exhaust ducts, and on airframe structures. Typically, acoustic liners that use foam or resonating chambers are used to create destructive interference with the incoming sound wave. The material and geometric properties of each acoustic liner determine the specific target range of frequencies that will get absorbed by the

liner. By changing these specific liner properties, the amount of sound absorbed at specific desired frequencies can be tuned. The majority of acoustic liners being used today are ineffective at absorbing sound with dominant frequency content below 500 Hz. Typical liners can't reach these low frequencies because of design constraints that restrict the allowable weight of the liner, and the amount of available space available for the liner to occupy. Another major restriction on traditional acoustic liners is the limited number of feasible manufacturing options available. There has been recent progress in developing new liners that are somewhat effective at absorbing lower frequencies than conventional, but the manufacturing complexities of these designs cause them to be too expensive for widespread commercial use. Thus, there exists a real need to develop a lightweight, compact, cost effective acoustic liner that can effectively mitigate low-frequency noise.

1.2 Noise Source Characteristics and Control

Before determining the best way to absorb low-frequency noise below 500 Hz, we first need to understand the noise source and its characteristics. Although low-frequency noise is a problem for various applications for various domains. The primary target application for this research is the aerospace industry. Therefore, this thesis will focus primarily on sources of noise from typical commercial aircraft. The two main aircraft components that are a source of low-frequency noise are the engines, and the airframe [4]. The engine noise can further be categorized into noise from the fan, and noise from the jet exhaust. Typically, during takeoff, the engine exhaust and the engine fan are the dominant noise contributors. While during landing, the engine fan and the airframe are the dominant noise sources.

Jet engine exhaust noise is caused by the mixing of exhaust gasses with the atmosphere. Turbulence created near the exhaust exit causes small eddies which produce a high frequency noise, while turbulence further downstream from the exhaust exit causes large eddies which produce low-frequency noise. Most of this high frequency exhaust noise is quickly dissipated by the atmosphere, but the low-frequency exhaust noise on the other hand, is not. In order to reduce the low-frequency exhaust noise, new engines have been developed over the years that reduce the mixing region at the exhaust exit. One way this can be achieved is by increasing the contact area between the atmosphere and the exhaust stream using corrugated or lobe-type mixer structures at the exhaust exit [5]. This method has a downside however, the same overall exhaust exit area must be kept to keep the same engine performance, therefore by adding these mixers, the overall diameter of the engine must be increased. This causes an increase in both weight and drag. Another way to reduce exhaust noise is to reduce the exhaust velocity of the engine. High by-pass-ratio engines such as the JT9D, CF6, and RB211 in the 1970's were able to reduce noise from the jet exhaust by eliminating inlet guide vanes, having wide axial spacing between the rotor and stator, and lastly by selecting the rotor-blade and stator-vane number to provide cutoff of blade-passing tones caused by wake interaction [6].

For high by-pass ratio engines like the ones listed above, the dominant source of engine noise is the fan. The different characteristics of fan noise depend upon whether the fan is operating at subsonic, or supersonic tip speed. At subsonic tip speeds, the noise is dominated by the blade-passing frequency and the higher harmonics of that frequency. At supersonic tip speeds on the other hand, the noise is dominated by multiple tones correlated with the rotational frequency of the shaft. Figure 1 shows the sound pressure level (SPL) experienced at subsonic and supersonic

tip speeds. The main method used to suppress the low-frequency noise generated by the engine fan is to add acoustic liners to the inlet side walls of the engine nacelle. Some typical liners used in engine nacelles today are discussed later in this chapter.

Significant improvement in overall noise (fan and exhaust) emitted from jet engines was seen when high by-pass ratio engines were introduced. Figure 2 shows this improvement in overall noise emitted between 1960 and 2010, as well as sources of engine noise for a typical 1960's engine compared to a typical modern engine.

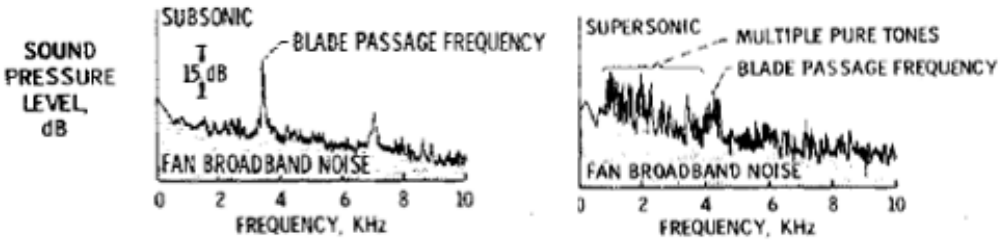

Figure 1: Fan noise spectrum at subsonic and supersonic tip speeds.[6]

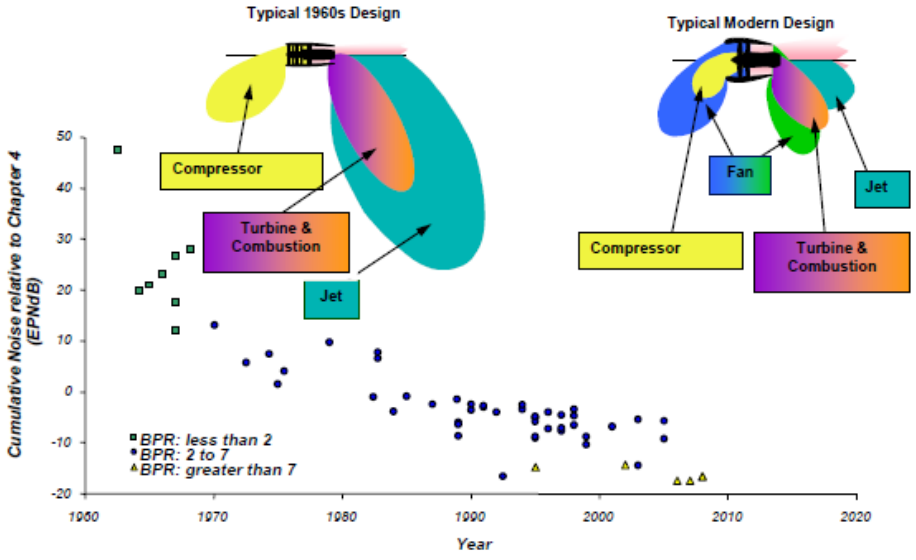

Figure 2: Progress made in reducing jet noise over time. [7]

Airframe noise is typically the dominant noise source heard from the ground when an aircraft is landing. It is characterized by sharp, low-frequency peaks typically less than 1,000 Hz. High speed air moving past the structures extending from the aircraft during landing such as the landing gear shaft, wing trailing edge flaps, wing leading edge slats, and other undercarriage elements, are the main source of airframe noise. However, these aren't the only source of airframe noise. Unsteady flow from wing and tail trailing edges, turbulent boundary layers on the fuselage and wing, vibrations from panels, and airflow past cutouts can also contribute to airframe noise [4]. Figure 3 shows how contributions from different noise sources in a typical jet engine can be compared.

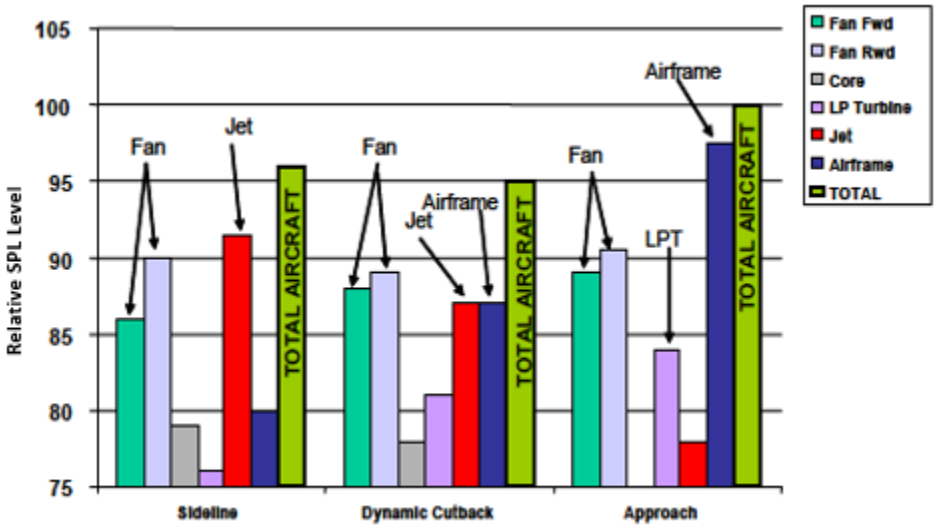

Figure 3: Contributions from different noise sources for a typical jet engine. [8]

1.3 Background

The study of acoustics, and acoustic wave propagation can be traced back to the mid to late 1800s. Pioneers such as Helmholtz, Kirchhoff, and Rayleigh all made significant contributions to

the field around that time. In 1863, Helmholtz published "*On the Sensations of Tone as a Physiological Basis for the Theory of Music,*" which was later translated from German to English and published by Dover Publications in 1954 [9]. Helmholtz was able to construct a precise mathematical description of sound vibrations in an open cylindrical tube [10]. In order to deconstruct these vibrations, Helmholtz created what would later be known as a "Helmholtz resonator." Using this device, shown in Figure 4, he was able to find that its primary tone is determined by its own composition and by the vibrations of the ear. If sound other than the primary tone is played, the sound is muffled. But when the primary tone is played through the resonator, that tone is heard quite powerfully.

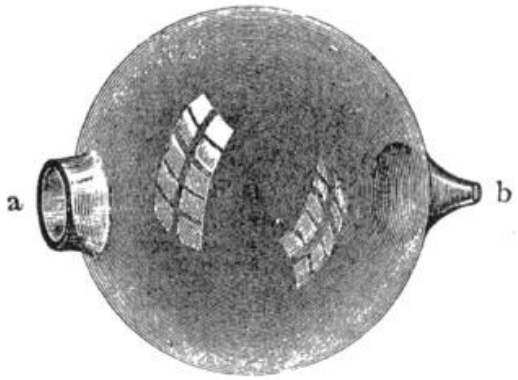

Figure 4: Helmholtz resonator, typically made from glass or metal. End "b" was inserted into the ear as end "a" was exposed to the source. [9]

Just 5 years later, Kirchoff developed an analytical solution to the problem of sound propagation through gasses in cylindrical tubes [11]. Building off of Helmholtz's work, Kirchoff was able to include thermal and viscous effects to the solution, making it the first more or less complete solution to this problem. Using a complex transcendental equation, Kirchoff was able to develop an approximate solution that holds for "wide" tubes, in which viscous dissipation becomes negligible. For more "narrow" tubes, viscous dissipation of the channel can't simply be neglected.

In 1896, Lord Rayleigh developed an approximate solution for these "narrow" tubes using Kirchoff's full analytical solution [12]. Later on, in 1953, Weston divided up the problem into 3 main types, 'narrow' tube, 'wide' tube, and 'very wide' tube, and developed higher order approximations for each of these cases [13]. Just 4 years prior to Weston's solutions, Zwikker and Kosten were able to derive analytical solutions to the simplified basic equations for the low-reduced-frequency case [14]. These solutions obtained for the first time by Zwikker and Kosten, can completely illustrate sound propagation through a cylindrical tube, as long as the low-reduced-frequency criteria ($K_{bar}<<1$ and $K_{bar}/s<<1$) is satisfied.

In 1975, Tijdeman summarized these early analytical approaches and solutions to the problem of propagation of sound in gasses contained in cylindrical tubes, and was able to rewrite the analytical solutions for the propagation constant Γ as a simple function of two specific parameters [15]. Those parameters are the shear wave number (s) (also referred to as the Stokes number), and the reduced frequency (K_{bar}). It was also shown that the entire problem of sound propagation through cylindrical tubes is governed by four dimensionless parameters: the shear wave number, the reduced frequency, the square root of the Prandtl number (σ), and the ratio of the specific heats (γ). Tijdeman also solved the Kirchoff equation in terms of those four parameters to eliminate the reduced frequency restriction imposed by Zwikker and Kosten. The low-reduced-frequency case is valid for the designs discussed in this study, so the solution obtained by Zwikker and Kosten was used to numerically predict liner performance. This numerical tool is discussed in greater detail in Chapter 2.

In the late 1960s, noise pollution emerges as a significant environmental issue in the United States. Inadequately controlled noise started to present a growing danger to the health and welfare

of the citizens. This growing concern led to the implementation of the Noise Control Act of 1972 [1]. Because of this growing public concern, engineers began to look for viable noise suppression and control techniques, especially for aircraft engines. In 1970, Mangiarotty was one of the first to classify different types of acoustic liners as a solution to the aircraft engine noise emission problem. Mangiarotty concluded that there were three basic types of acoustic lining suitable for acoustically treated engine ducts, the absorber type, the resonator type, and an absorber/resonator combination type.

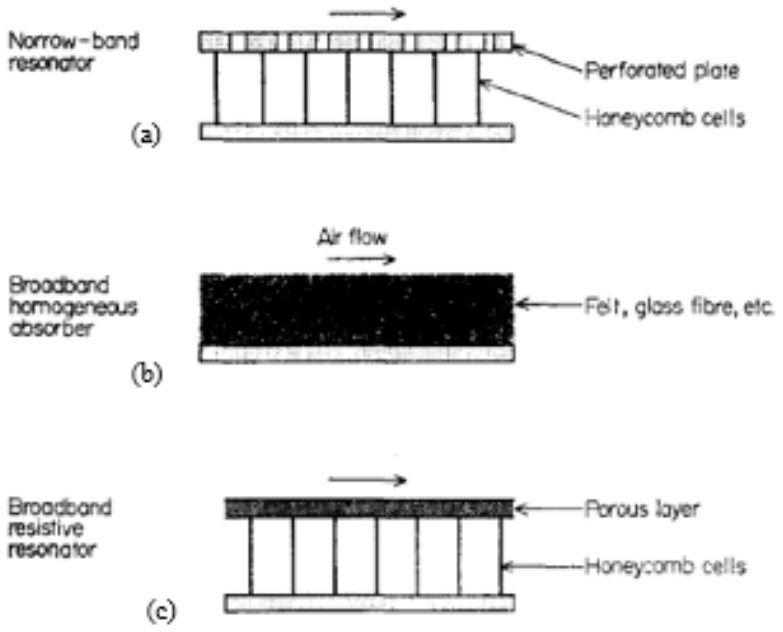

Figure 5: Types of duct liners described by Mangiarotty. [17]

It was concluded that the most important acoustic factors of the lining were found to be the acoustic impedance of the lining, and the depth of the lining cavity. It was shown that the application of acoustic linings on a Pratt and Whitney JT3D engine resulted in a noise reduction

of over 15 EPNdB in the approach-landing phase, with little measurable loss in the overall performance of the aircraft.

These three basic types of liners shown in Figure 5 could also be described as locally reacting, non-locally reacting, or a combination of both. The resonator type liners are locally reacting, which means that they permit propagation only in the direction normal to the duct wall [18]. The absorber type liner on the other hand, is non-locally reacting, meaning that they permit propagation in multiple directions. Locally reacting liners are the most common in practice, because they are easy to manufacture and possess desirable mechanical properties such as stiffness and serviceability. They are typically made as a three layer sandwich composite, where the bottom layer is an acoustically rigid plate (typically aluminum or fiber-epoxy composite), the middle layer is comprised of an aluminum or composite honeycomb core, and the top layer is a perforated plate. Each of the individual honeycomb cells combined with the perforated face sheet, act as Helmholtz resonators, which were briefly introduced earlier in this chapter, and will later be fully discussed in Chapter 2. Non-locally reacting liners are less commonly used as external structures because of their poor mechanical properties, and their tendency to absorb fluids. They are however commonly used for indoor sound absorbers or interior paneling on vehicles. Non-locally reacting liners are made from various types of soft material such as fiber glass or different types of foam. They typically have better broadband absorption performance

In 1975, Pratt and Whitney conducted a study to evaluate a new means for increasing the effectiveness of acoustic liners for low-frequency applications by coupling locally reacting Helmholtz resonators together with non-locally reacting concepts [19]. The study, conducted under the supervision of NASA, looked at three different coupled resonator schemes with the aim

of effectively attenuating noise over a frequency range of one to two octaves centered at 400 Hz. All comparisons were made holding to strict liner volume limitations specified by a baseline liner, which is shown in Figure 6.

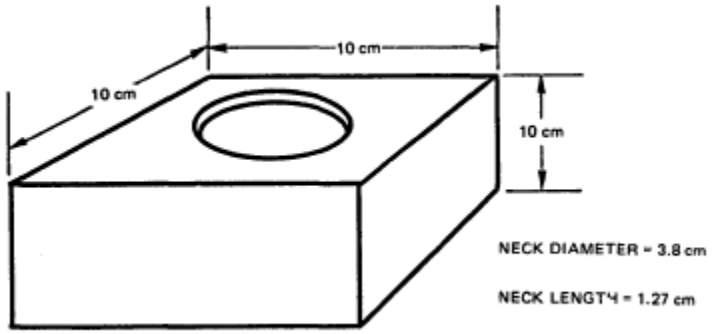

Figure 6: Pratt & Whitney baseline liner. [19]

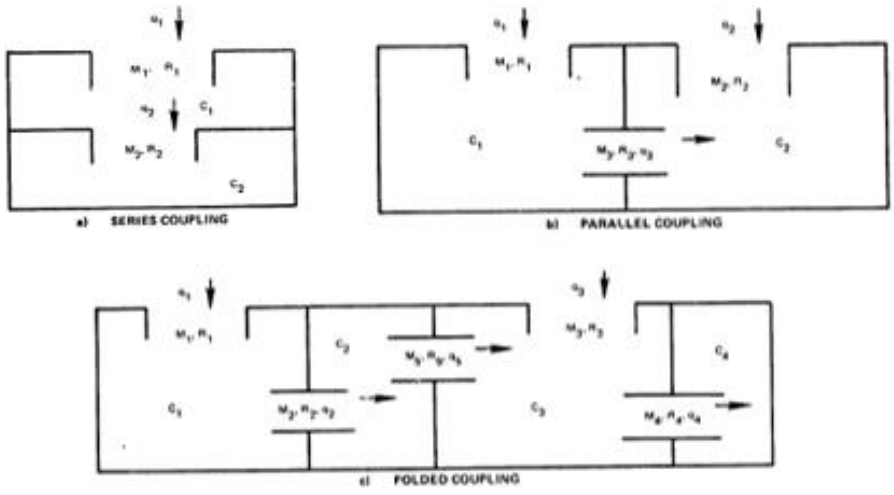

Figure 7: The three coupled resonator schemes compared in the Pratt & Whitney study. [19]

It was found that the most promising coupling scheme was the parallel coupling scheme, shown in Figure 7 b). The optimized parallel coupling design had an increase in peak attenuation of 50%

and an increase in attenuation bandwidth of 1/3 octave over the best uncoupled design tested. The design was optimized by varying the design parameters to minimize the perceived noise level of a typical low-frequency noise spectrum. The derivation of impedance models for all three types of coupled resonators by using the governing equations of motion and the single resonator equation parameters was also shown. Then, good agreement between the predictions from those models and the measured impedance for the different designs is presented. The conclusion that the coupled resonator concept was more effective than the uncoupled concept for attenuation of low-frequency broad spectrum noise was reached. Although this non-typical design showed promising improvement, the 10 cm (approx. 4 in) liner thickness used in these designs is significantly greater than current state-of-the-art liner thicknesses.

Pratt & Whitney were not the only ones exploring out-of-the-box acoustic liner designs in the late 1970s. Baumeister performed a study on optimized multi-sectioned (or phased) liners in hopes of increasing the attenuation of a liner in 1979 [20]. The idea was to take a certain liner with a uniform fixed cavity depth, and subdivide that liner into several different segments that are jointly optimized to maximize the noise attenuation over that of a uniform optimized liner. He was able to show that axially segmented liners show a theoretical increase in the attenuation compared to a uniform liner with straight cavities of the same length. Segmenting the liner was found to be most effective at high frequencies with relatively long duct lengths. Baumeister was also able to determine that very little advantage existed in using more than two segments per cavity. Study of attenuation bandwidth of the segmented liners also show little advantage compared to the bandwidth of a uniform liner. Lastly, multi-element liners studies showed a large decrease in performance due to changes in the input modal structure. Baumeister concluded from this study

that for low-frequencies, the segmented liner designs failed to offer a sufficient improvement in performance to justify their replacement of a uniform liner.

Another early liner concept called a silator was developed in the hopes of reducing the overall volume needed by a traditional Helmholtz style liner [21]. This was done by evacuating air from an acoustically non-rigid lentiform made from aluminum sheet metal, creating a vacuum chamber in the middle. A sketch of a cross section of a silator, along with a photograph of its components can be seen in Figure 8.

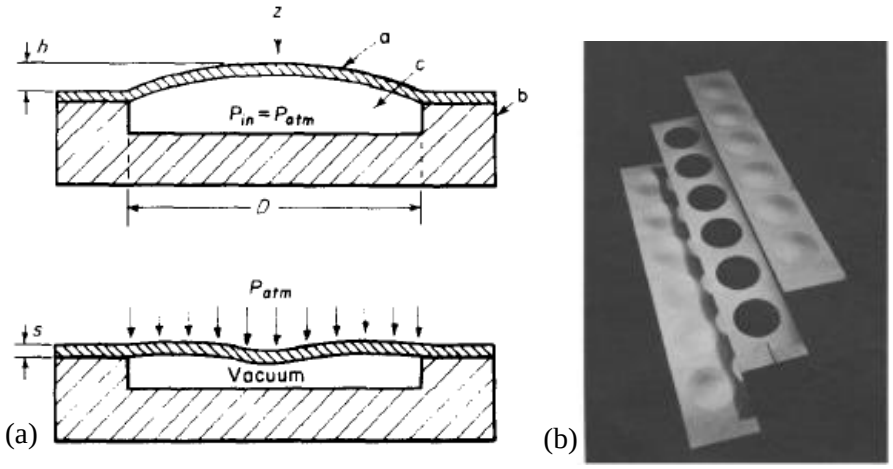

Figure 8: (a) Silator cross section before and after air evacuation, and (b) photograph of silator components (right). [21]

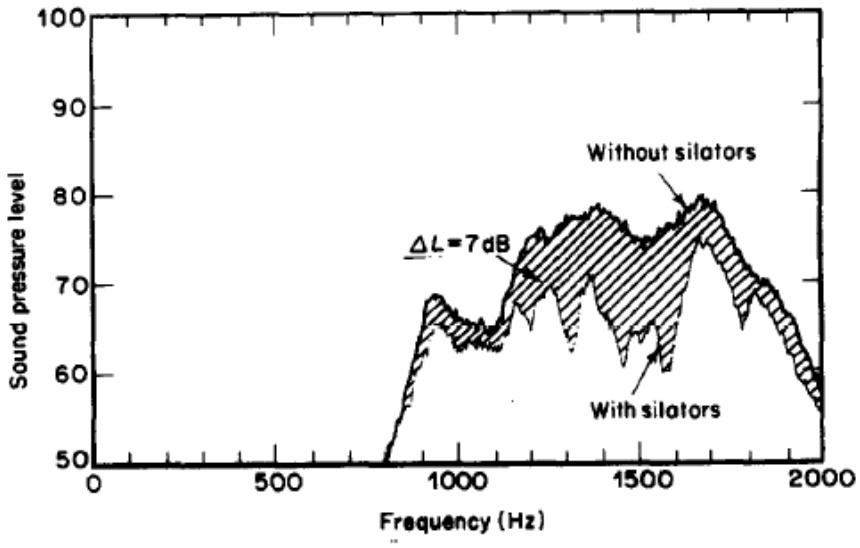

Figure 9: Experimental silator performance. SPL in dB. [21]

It was found that the silator performed similarly to a Helmholtz resonator, but with only occupying a hundredth of its volume. As you can see from Figure 9, this design was effective at reducing the SPL over a large bandwidth of high frequencies. Manufacturing complexities of the silator, along with no noise reduction in the low-frequency range, make this design not viable to solve the low-frequency noise problem that this thesis is concerned with.

1.4 State-of-the-Art

Recently, many attempts have been made at creating new acoustic liners capable of mitigating noise in frequency ranges less than 500 Hz. Some of these attempts have been for very specific applications, such as the attempt made by the Goodrich Aerostructures Group in 2006 [22]. Their objective was to design an effective acoustic liner for a hot nozzle center plug, using a folded cavity Helmholtz resonator concept. They wanted to target noise in the frequency range of 400-630 Hz. This frequency range was determined from GE ground test data for combustion noise in

a high power approach flight condition. Figure 10 shows the magnitude of combustion noise in relation to other noise sources during both arrival and departure conditions. The combustion noise is about 10 dB lower than the other dominant noise sources, but with increased focus on reducing fan and jet noise, combustion noise could be a primary source of noise in the near future.

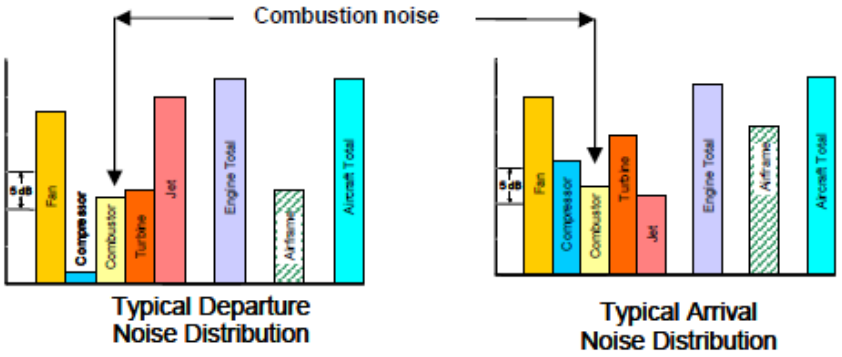

Figure 10: Typical noise contributions to total aircraft noise for modern turbofan aircraft. [22]

Their design featured eight total folded chambers divided up using four axial solid dividers, which act as acoustically rigid boundaries to prevent sound from acoustic interaction. Large open area perforated plates are then used to divide up each section into two chambers. This design provides structural support as well as prevents higher sound wave modes from propagating into the two chambers. Figure 11 shows a detailed CAD model of the design.

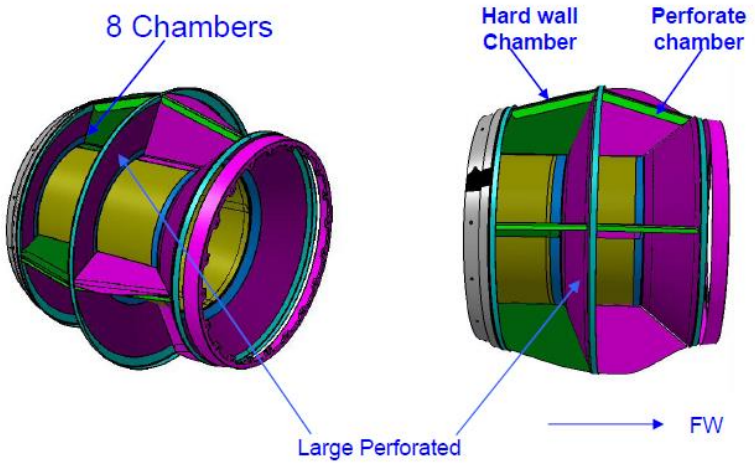

Figure 11: Eight-chamber folded cavity liner for hot nozzle center plug. [22]

The static engine test results showed that a reduction in 11 dB in combustion noise reduction at 400 Hz can be achieved at flight idle conditions. At approach conditions, the combustion noise was reduced by 3-4 dB. They discovered that the liner performance decreased as the power to the engine increased. This can be attributed to the increase in liner resistance as the flow Mach number increased with power. The results from this study show that a folded cavity Helmholtz design can be effective at attenuating sound around the 400 Hz frequency range.

In 2010, Sugimoto et al. published a paper in which they explored a new acoustic liner design that implemented 2D single folded cavities [8]. Typical acoustic liner thicknesses are approximately up to one to two inches. In order to target lower frequencies while keeping the same overall liner thickness, the liner cavities are folded into L-shaped geometry in order to increase the cavity length. This relationship between cavity length and target frequency is discussed in further detail in Chapter 2. To determine the effectiveness of this L-shaped geometry, typical single degree of freedom (SDOF) and double degree of freedom (DDOF) liners were used for comparison. A

SDOF liner is typically an aluminum honeycomb composite with a thin porous face sheet overlaid on top, like the narrow band resonator in Figure 5. A DDOF liner is essentially two SDOF liners stacked on top of each other with a porous septum in between them. Sugimoto analyzed four different SDOF liners like the one shown in Figure 12 via a finite element analysis program, to see how different cavity depths effected the absorption coefficient spectrum.

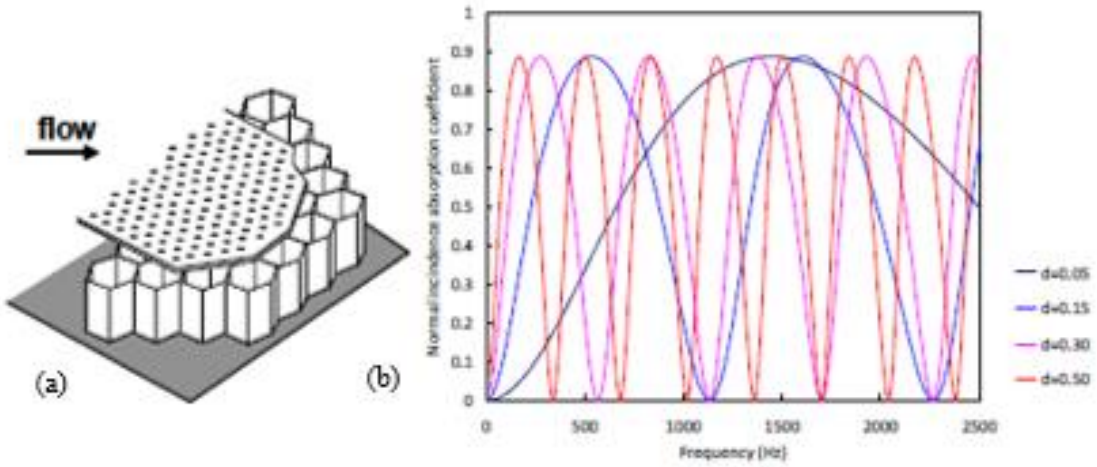

Figure 12: (a) Typical construction of a SDOF acoustic liner. (b) Normal incidence absorption coefficient of SDOF liners of varying depths (meters). [8]

As can be seen from Figure 12 b), the cavities must be extremely long in comparison to the one to two inch overall liner thickness available in order to effectively absorb frequency content below 500 Hz. So in a attempt to decrease the overall liner thickness, performance of different L-shaped liners (Figure 13) was compared to the SDOF liners.

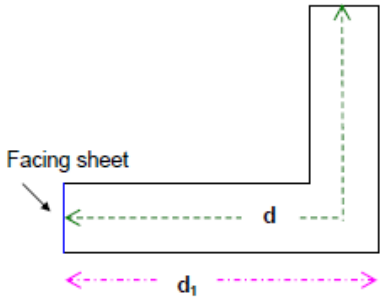

Figure 13: Folder liner, total path length d and liner depth d_1. [8]

By keeping the overall path length at 0.5 m, but changing the liner depth d_1, they were able to directly compare the folded cavity results to the results from the 0.5 m deep SDOF liner. The results showed that at low frequencies, the L-shaped liners behaved the same way as the SDOF liners, but as the frequency became larger, the L-shaped started to behave as if the total path length was that of d_1 instead. Results from the recent study are in agreement with this behavior.

Other passive liner designs, such as the three examined by Jones et al. in 2012, emphasized the need for alternate approaches for low-frequency noise absorption [23]. The first of these designs consists of multiple parallel, variable-depth, narrow chambers that act as quarter wave resonators (Figure 14).

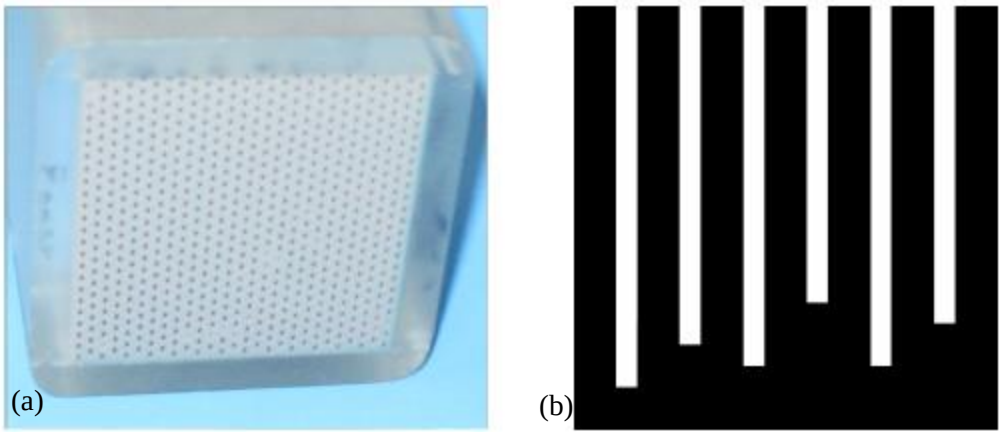

Figure 14: (a) Narrow chamber liner photo and (b) sketch (right). [23]

Results from this design were first presented by Parrott and Jones (1995) [24], and are utilized in the 2012 study to determine whether similar results can be achieved from other concepts. This design (Figure 14) showed very promising results, but the ceramic material used is very heavy and brittle, making the design not practical for use in aircraft engine nacelle liners. The results are well understood and can be predicted with great accuracy, so NASA continues to use these liners to validate impedance eduction processes. Each 2 inch x 2 inch sample of the narrow chamber design contains 177 chambers, each with a diameter of 0.07 inches. Nine unique depths ranging from 1.12-2.41 inches are used in the variable depth design (NC2), while the uniform design has 177 chambers of equal 1.69 inches of depth (NC1).

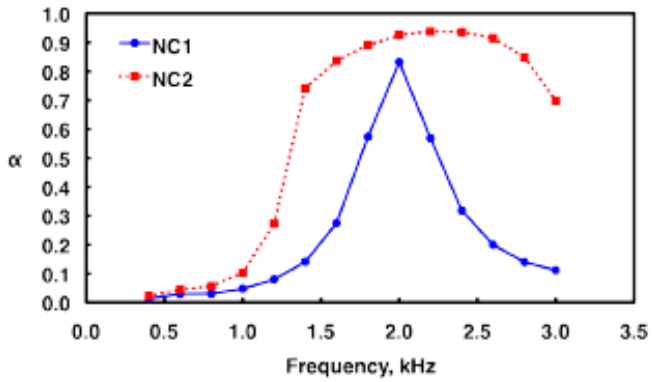

Figure 15: Comparison of measured absorption coefficient spectrum for two narrow-chamber liners. [23]

The wide chamber design is very similar to this narrow chamber design, but the narrow chambers are replaced with much wider chambers (Figure 15). A face sheet is a required addition to this second design to inhibit mean flow from entering into the chambers. Each 2 inch x 2 inch sample of this wide-chamber design contained 25 cells with a 0.375 inch x 0.375 inch cross sectional area. Like the narrow-chamber design, the wide-chamber was made with both uniform constant depth cavities (WC1) and variable depth cavities (WC2) with cavity depths ranging from 1.14 inches to 3.39 inches (Figure 16 a)). The 25 cell count of these designs led to the 25 cell count in the Quarter Wave Baseline design discussed in Chapter 2 of this document.

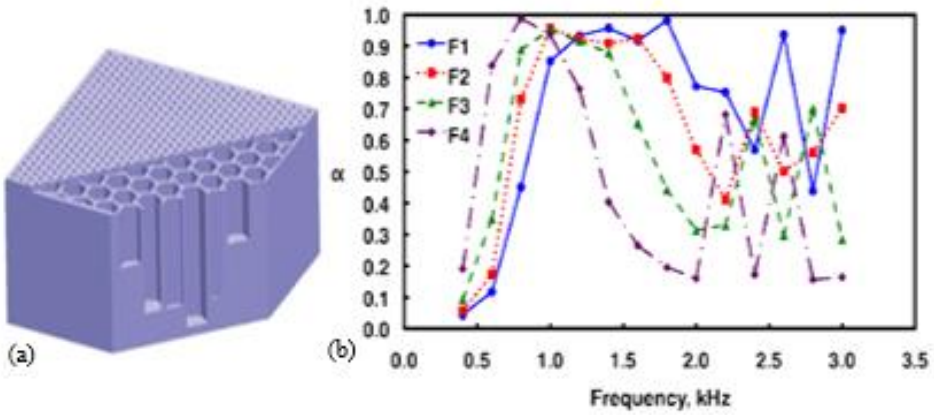

Figure 16: (a) Cutaway view of a variable-depth, wide-chamber liner with included face sheet. (b) Absorption coefficient spectrum comparison of variable depth core WC2 with different face sheet specifications (Table 1). [23]

Facesheet #	F1	F2	F3	F4
Hole Diameter (inches)	0.035	0.035	0.035	0.035
Sheet Thickness (inches)	0.025	0.500	0.100	0.200
Porosity (%)	10	10	10	10

Table 1: Face sheets for wide-chamber test liners. [23]

The next design in the study by Jones el al., is a multi-layer liner that includes mesh-caps embedded into a honeycomb core (Figure 17). The mesh-caps are from Hexcel's Acousti-Cap® technology that is designed to support individual cell treatments [25]. A single mesh-cap is inserted into each 0.375 inch diameter honeycomb cell at either a uniform, or variable cavity depth. A face sheet is then added to the top of the honeycomb. Two mesh-cap test articles are tested, MC1 which is a two layer configuration at 1.5 inches thick, and MC2 which is a 1.5 inches thick three layer configuration.

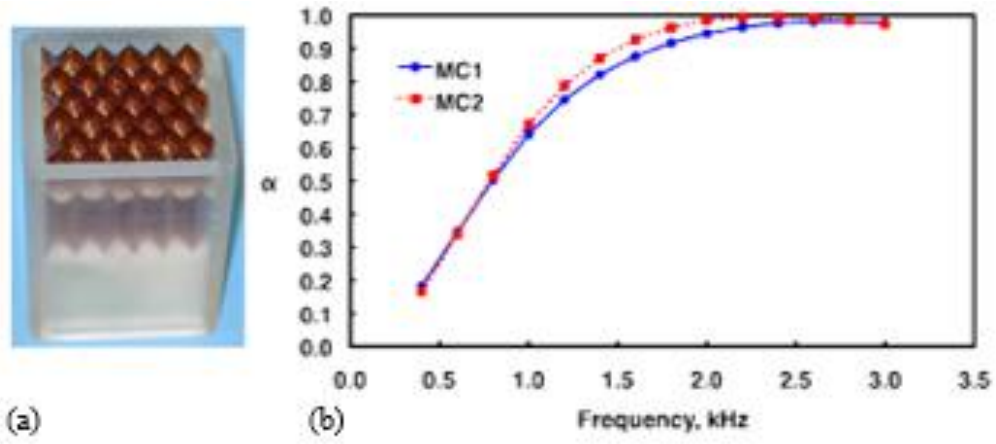

Figure 17: (a) Photographs of mesh-cap sample, face sheet not shown. (b) Absorption coefficient spectrum comparison for the two mesh-cap designs. [23]

The results from the three different concepts (Figures 15, 16, 17) show that none of them are have significant absorption below 500 Hz. Thus, further exploration of design ideas must take place in order to find a viable solution.

A new concept developed by Beck et al. in 2014, sought to reach low-frequency noise by combining the idea of a Helmholtz resonator metamaterial with a traditional quarter-wave acoustic liner [26]. Any engineered material is considered to be a metamaterial if is it built of individual elements of small conventional materials that exhibit properties not found in nature. This new metamaterial inspired liner was designed to increase the low-frequency noise reduction while minimizing liner thickness. A design schematic along with a photograph of the sample can be seen in Figure 18.

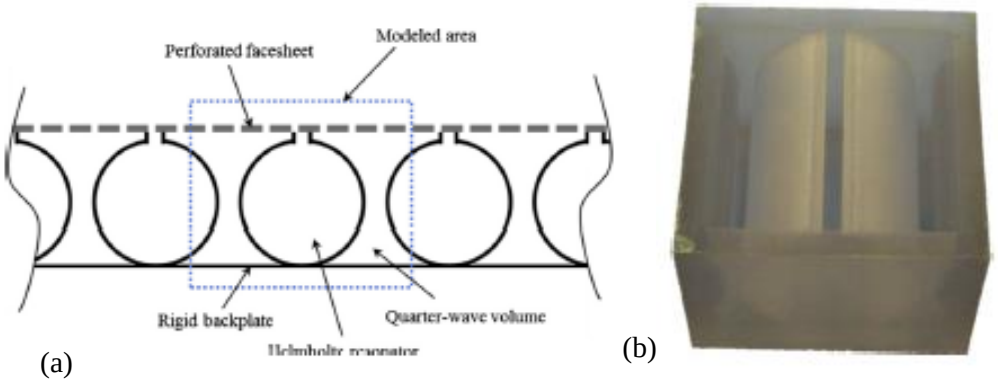

Figure 18: (a) Dual-resonance metamaterial design schematic and (b) photograph shown without perforated face sheet (right). [26]

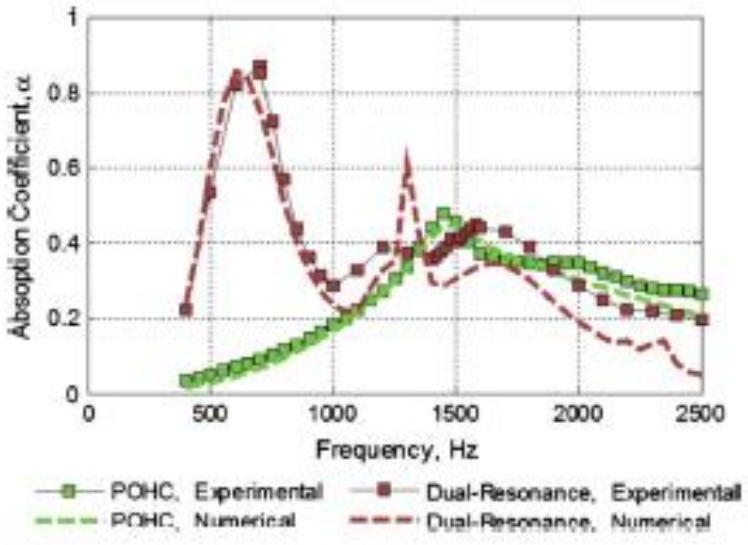

Figure 19: Absorption coefficient spectrum shown comparing the Dual-resonance liner design with a traditional perforated face sheet over honeycomb (POHC) design. [26]

Results in Figure 19 show that the dual-resonance design has significantly improved performance below 1000 Hz compared to the traditional honeycomb liner. This is a result of the incorporation of a Helmholtz resonator to the design. The results also show that the dual-resonance liner has similar performance to the POHC design at frequencies above 1000 Hz. This is due to the quarter-wave resonator aspect of the design. The total liner thickness is 1.54 inches, so the dual-

resonance design is effective at reducing the liner thickness while absorbing noise at a much lower frequency range. However, the lowest frequency at which the absorption coefficient is at least 0.6 is 500 Hz. So the problem of absorbing sound at a minimum of 0.6 absorption at frequencies below 500 Hz remains unsolved by this design. Structural integrity may also be diminished for this case relative to conventional designs.

Other recent acoustic metamaterial designs have attempted to target these frequencies below 500 Hz using flexible membranes. One such design presented by Fan et al. [27] featured stacked membrane coated perforated plates. This particular design showed promising low-frequency sound insulation, but was only examined using finite element simulations and theoretical analysis. The manufacturing complexity and the long term durability of the membranes could be potential challenges to overcome for making this design into a practical liner. Ma et al. [28] also showed that a membrane-type acoustic metamaterials (MAMs) can be effective at reaching frequencies below 500 Hz. The design from Ma et al. features four locally resonant MAMs arranged around a circular orifice with a radius of 12 mm. Each of the four MAMs consist of a 12 mm radius latex membrane that is 0.2 mm thick. A circular rigid disk weighing 70 mg is attached to the center of each membrane. This configuration can be seen in Figure 20.

Figure 20: MAMs device developed by Ma et al. [28]

This design was shown to be effective as a narrow-band acoustic filter for low-frequency applications. The narrow bandwidth of effectiveness, along with its manufacturing complexity could make this design impractical for commercial use in aircraft engine liners. Also, this device was design for transmission loss, and not absorption.

Another research project in 2014 by Slagle [29], also sought to improve sound absorption of noise in the frequency range below 500 Hz. He studied poro-elastic acoustically heterogeneous (HG), and microperforated (MPP) acoustic metamaterials in an attempt to solve this problem. HG metamaterials consist of a poro-elastic material with periodically arranged embedded masses. MPP metamaterials consist of periodic layers of micro-porous panels embedded in a poro-elastic material. Results show good absorption below 500 Hz, with a significantly wide bandwidth of absorption. The problem with the practicality of these designs is the overall thickness needed to reach frequencies below 500 Hz (2" at the minimum), the manufacturing complexity with adding embedded masses, the additional weight from the embedded masses, and lastly the potential degradation of performance of the foams in the presence of fluids such as rain.

Moving away from metamaterials, there are other recent low-frequency liner designs have also attempted to absorb frequency content below 500 Hz. Wu et al. [30] in June 2016 published a paper describing a low-frequency liner design that utilizes split tube resonators. Each split tube resonators is composed of two 180° twisted ellipse shaped split tubes and manufactured using 3D printing (Figure 21).

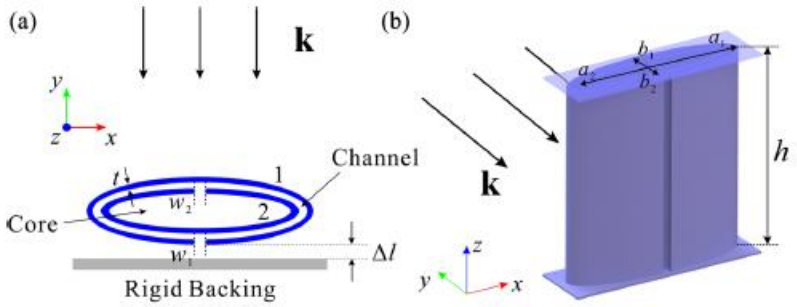

Figure 21: (a) cross sectional sketch with (b) 3D render of the resonator with incident wave K shown with direction). [30]

Experimental results of three different dimensional variances of this design show a narrow band absorption peak at low frequencies below 500 Hz. The three different absorption peaks for the three separate designs were shown to be centered at approximately 420 Hz, 330 Hz, and 280 Hz. Each of these peaks had a continuous bandwidth of absorption at 0.6 of 55 Hz, 30 Hz, and 48 Hz respectively. Although these designs show absorption peaks below 500 Hz, the small bandwidth of absorption would be inefficient for practical use. The mechanical properties of these resonator structures could also be a disadvantage, specifically the stiffness of the liner in the y direction. The height h of the liner in the z direction is also rather large, at 8.6 cm (3.4 in) for the low-frequency it intends to absorb.

Another 3D printed low-frequency design is presented by Li and Assouar [31], which shows the potential to reach low frequencies with minimal overall thickness. The design utilizes 3D printing to make a single planar coiled chamber tuned to reach low frequencies (Figure 22).

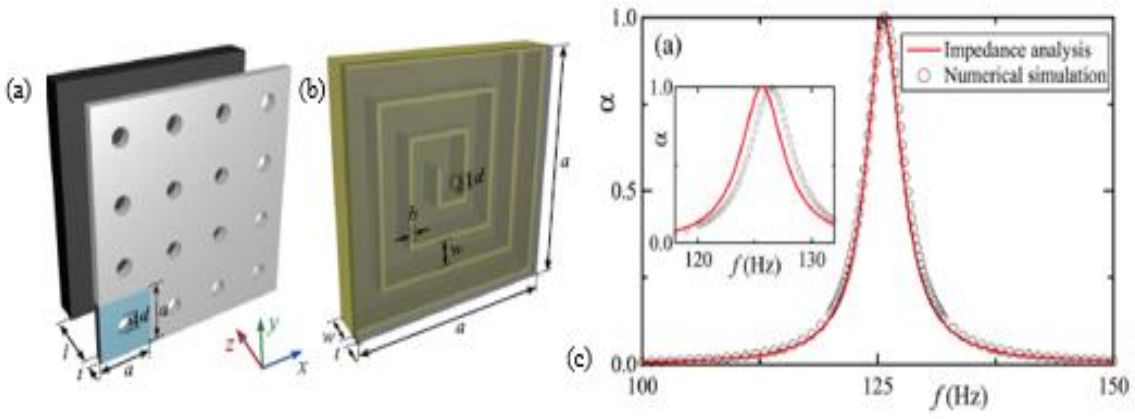

Figure 22: (a) & (b) Coiled chamber design schematic. (c) Comparison of absorption coefficient spectrum for a numerical simulation and analytical prediction of the liner design. [31]

This design is coiled in the sense that it is able to reach a very low-frequency, while keeping the overall liner thickness under 0.5 inches. However, there are several potential disadvantages in this design that could make it impractical to implement for commercial use. First, the overall surface area that an incident wave would see for a single cavity is rather large, at approximately 4 inches x 4 inches. Thus, not many total cavities would be able to fit in a given area. Secondly, the common methods of 3D printing could prove incompatible for manufacturing this design as a single component unless certain special processes or special steps are undertaken.

While considerable headway has been made in designing low-frequency liners, a commercially practical, broadband, tunable solution is yet to be achieved. Thus, the research done in this thesis is aimed at making contributions to this goal.

1.5 Definition of Objectives

Motivated by the need to develop a practical passive acoustic liner capable of absorbing noise with a dominant frequency bandwidth below 500 Hz, the objectives of this study have been established as follows.

- Define and down select candidate lightweight, compact, structurally-integrated acoustic liner design for further investigation.
- Investigate the possibility of developing folded cavity cores made feasible by emergent manufacturing processes.
- Employ numerical and analytical models to predict absorption performance of candidate acoustic liner designs with sufficient accuracy.
- Create a comprehensive software tool to optimize liner designs for prescribed source specifications, and mass and volume constraints.
- Develop a non-dimensionalized metric to compare low-frequency absorption performance of different candidate liner designs.
- Utilize additive and hybrid manufacturing techniques to construct prototype test articles.
- Perform experimental verification of prototype liner designs using normal incidence impedance tube, and grazing flow impedance tube.
- Minimize weight addition to new liner designs in comparison to current in-service acoustic liners.

1.6 Chapter Overviews

Chapter 1 discussed the motivation behind the research performed for this thesis along with a detailed description of past work in the area of low-frequency acoustic noise mitigation. It also gave examples of current state-of-the-art acoustic liner designs that were aimed at absorbing frequencies below 500 Hz.

Chapter 2 provides a review of analytical terminology and methods along with a detailed description of the numerical approach used to predict liner performance and optimize liner configurations. Chapter 2 also gives a detailed description of the definition and application of the Low-frequency Performance (LFP) factor and its implementation, which is used as a metric to compare different liner configurations within the Folded Cavity Packing Optimization Code. An in-depth description of liner designs developed as a consequence of this study, along with predicted performance for those designs, can also be found in Chapter 2. Lastly, Chapter 2 details a parametric study to examine the effect of face sheet porosity on liner performance.

The experimental testing standards and method used for the normal incidence tube and the grazing flow tube is presented in Chapter 3. Test article fabrication and material selection for the various designs along with discussion of experimental results are also presented in Chapter 3.

Chapter 4 summarizes the major conclusions from this study and offers recommendations for future work to be done in the field of low-frequency acoustic liner research.

CHAPTER 2

ANALYTICAL AND NUMERICAL DESIGN STUDIES

There are several different classifications of liners that are important to note. The first major distinction that needs to be made is whether the liner is locally, or non-locally reacting. Locally reacting liners are predominantly resonance driven, while non-locally reacting liners rely on dissipation from convoluted sound passageways. Non-locally reacting liners are typically bulk absorbers such as foams, but can also be comprised of distinct cavities that are able to communicate with each other such as the coupled resonator designs from Pratt & Whitney [19]. Non-locally reacting liners are typically used as non-structurally integral claddings used for example in interior cabin paneling in aircraft, and exhibit good broadband absorption for high-frequency noise. Locally reacting liners on the other hand, are commonly used as structurally integral parts capable of supporting a load. Typical examples include traditional honeycomb liners [17] and Hexcel Acousti-Cap® liners [25]. Locally reacting liners can be further categorized as either broadband, or single-tone. Locally reacting broadband liners target a large range of frequencies, while locally reacting single-tone liners target a much smaller range of frequencies. Another classification that can further distinguish liner types can be applied to both locally reacting and non-locally reacting liners, passive or active. Passive liners are not dependent on the noise environment they are in. They are typically tuned for a specific frequency range, but once implemented they do not change. Active liners on the other hand, can adapt to changing acoustic conditions. Active liners do not remain statically unchanged.

For this study, a passive, lightweight, compact, and structurally-integrated liner capable of absorbing a broadband frequency range below 500 Hz was desired. The importance of developing a liner that is lightweight narrowed down the possible solutions by eliminating any design aimed at reaching lower frequencies by adding mass to already existing liner designs, such as embedded mass inside bulk absorbers. The passive classification eliminated any active liner design ideas from being developed in the course of this study. Based on the desired structurally-integral and compactness characteristics, the exploration of bulk absorber type non-locally reacting liner designs was not considered as a potential solution to this problem either. The desired broadband absorption at low-frequencies further narrowed the potential liner designs. Based on these desired characteristics, locally reacting folded cavity liner designs seemed the most promising, and became the main focus of this research.

2.1 Mechanism of Liner Absorption

Most locally-reacting passive acoustic liner designs utilize either the quarter wave cancellation mechanism or the Helmholtz resonance mechanism to attenuate noise at specific frequencies. Both of these mechanisms can be tuned to target a certain frequency by changing certain dimensional parameters. A Helmholtz resonator can be represented as a simple single degree-of-freedom (SDOF) spring-mass system. The air trapped in the neck (shaded area in Figure 23) acts the mass, while the air trapped in the cavity acts as the spring. The frequency at which the system begins to resonate is given by the following equation.

$$f = \frac{c}{2\pi}\sqrt{\frac{S}{VL'}} \tag{1}$$

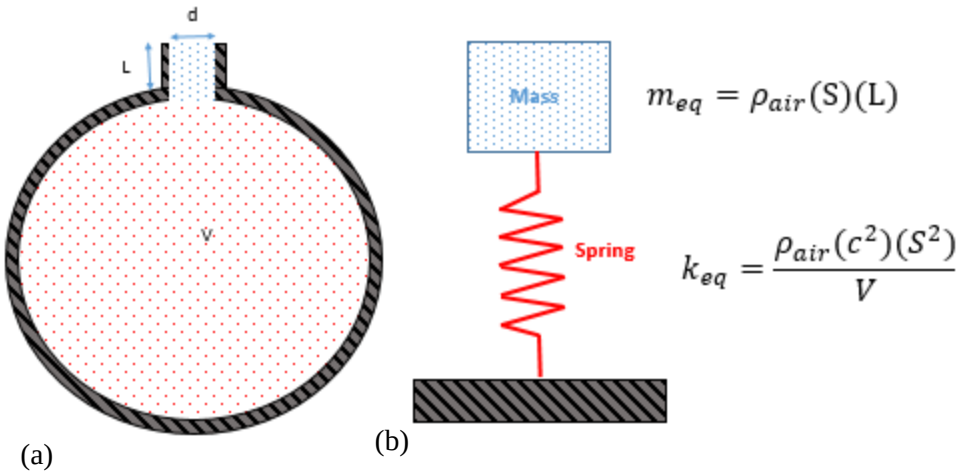

Figure 23: (a) Sketch of a simple Helmholtz resonator and (b)An equivalent mass-spring system.

Where c is the speed of sound in air, S is the cross-sectional area of the neck, V is the internal cavity volume, and L' is the effective length of the neck. L' includes an end correction factor that accounts for the additional mass of air at the lip of the cavity opening that moves in conjunction with the mass of trapped air inside the neck [32].

$$L' = L + 0.48(S^2)\left(1 - 1.25\frac{d}{d_c}\right) \tag{2}$$

This end correction factor is valid for $\frac{d}{d_c} < 0.4$. If this criteria is not satisfied, a different equation provided in [32] must be used. The mass of air trapped in the neck oscillates due to the effective spring (volume of air inside the cavity). At the designed resonant frequency, the effective mass-spring system oscillates out of phase with the incoming sound wave. The incoming sound wave then becomes effective absorbed by the Helmholtz resonator. By changing the neck size or the volume of the cavity, a Helmholtz resonator can be tuned to resonate at a certain frequency. In order to reach lower frequencies with this method of absorption, either the cross-sectional area of

the neck must be reduced, the volume of the cavity must be increased, or the length of the neck must be increased. Traditional honeycomb liners utilize this mechanism of absorption. Reaching lower frequencies with traditional honeycomb liners is problematic for several reasons. One reason being that increasing the length of the neck would also increase the thickness of the face sheet, which adds weight to the liner. Another reason conventional honeycomb liners are not ideal for reaching low frequencies is that increasing the volume of the cavity would either cause an increase in the overall thickness of the liner (which would add weight and potentially violate volume restrictions), or a decrease in the number of cavities contained in a given area of the liner, leading to a degradation of mechanical properties.

The mechanism of absorption for a quarter wave resonator is fundamentally different than that for the Helmholtz resonator. A quarter wave cavity reaches resonance when the cavity length l_c is 1/4th of the wavelength λ of the incoming sound wave. At resonance, maximum vibration amplitude occurs at the open surface, causing significant scrubbing against the cavity walls. This scrubbing converts the acoustic pressure to heat via the wall friction, thus absorbing the acoustic energy at that frequency.

$$f = n\frac{c}{\lambda} = n\frac{c}{4l_c} \qquad n = 1,3,5,,, \tag{3}$$

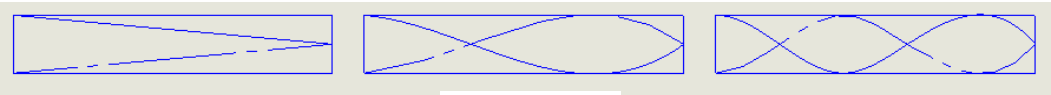

$$f_1 = \frac{c}{4l_c} \qquad f_3 = 3\frac{c}{4l_c} \qquad f_5 = 5\frac{c}{4l_c}$$

Figure 24: Sketch of destructive interference of a harmonic wave in a quarter wave resonator cavity. The solid line represents the incoming wave, and the dotted line represents the reflected wave.

By utilizing quarter wave cancellation in an acoustic liner, the higher harmonics of the fundamental frequency to which the cavity length is designed are also destructively interfered with. One way to reach lower frequencies with this method is to increase the cavity length. If the cavities stay straight, then the overall liner thickness must be increased, which would add weight to the liner. So in order to increase cavity length without changing the overall liner thickness, the cavities within the liner would need to be folded and efficiently packed within the liner to maximize low-frequency performance for prescribed mass and volume constraints.

2.2 ZKTL-Based Numerical Simulation Model

The study conducted by Parrott and Jones in 1995 [24], resulted in the development of a numerical model capable of predicting acoustic performance for a variety of locally reacting liner configurations. The model is the Zwikker-Kosten Transmission Line (ZKTL) Code, because it is based on the Zwikker and Kosten's theory of sound propagation in channels [14] to predict the surface impedance of a liner. Updates to the code were later added and published in a user's guide in 1997 [33]. In this model, individual impedances of an arbitrary set of channels are calculated, then the area-weighted acoustic admittances of all the channels are summed up in order to find the total admittance of a particular liner design. Once the total admittance is known, the total impedance is easily found as its reciprocal, and the absorption coefficient spectrum can be directly calculated.

The model firstly requires imputing relevant parameters specific to a particular liner design. It can be used to evaluate open channels, resistive layers, and porous materials. The following thereby is valid for the evaluation of acoustic liner performance when the liner is composed of open channels with no resistive layers or porous materials. Most designs in this study can be analyzed

as such. One other important assumption to note is that the Zwikker and Kosten solution assumes a low-reduced frequency case. Where the reduced frequency $K_{bar}<<1$ and $K_{bar}/s<<1$. All designs in this study satisfy this criterion. Here s denotes the shear wave number using notation obtained from Tijdeman [15]. The shear wave number is given by,

$$s = \frac{\mathrm{d}_c}{2}\sqrt{\frac{\rho\omega}{\mu}} \tag{4}$$

and the reduced frequency is,

$$K_{bar} = \frac{\omega d_c}{2c}. \tag{5}$$

The propagation constant Γ can then be found by,

$$\Gamma = \sqrt{\frac{J_0(i^{1.5}s)}{J_2(i^{1.5}s)}\gamma\left(1+\frac{\gamma-1}{\gamma}*\frac{J_2(i^{1.5}s\sigma)}{J_0(i^{1.5}s\sigma)}\right)} \tag{6}$$

where $J_{0,2}$ finds the Bessel functions of the first kind. Next the characteristic impedance z_c is calculated from,

$$z_c = \frac{-i}{\Gamma}\left(\frac{J_0(i^{1.5}s)}{J_2(i^{1.5}s)}\right). \tag{7}$$

Once the characteristic impedance and propagation constant are found, the entries for the forward transmission matrix are calculated.

$$t_{11} = t_{22} = \mathrm{Cosh}[k\Gamma l_c] \tag{8}$$

$$t_{12} = z_c\mathrm{Sinh}[k\Gamma l_c] \tag{9}$$

$$t_{21} = (z_c{}^{-1})\mathrm{Sinh}[k\Gamma l_c] \tag{10}$$

$$\begin{bmatrix} \mathrm{p}_{n+1} \\ \mathrm{u}_{n+1} \end{bmatrix} = \begin{bmatrix} t_{11} & t_{12} \\ t_{21} & t_{22} \end{bmatrix} \begin{bmatrix} \mathrm{p}_n \\ \mathrm{u}_n \end{bmatrix}. \tag{11}$$

The forward transmission matrix describes the wave transmission through a dissipative channel. After the forward transmission matrix, the channel admittance β_c for an individual channel is calculated as

$$\beta_c = {}^{\mathrm{u}_{n+1}}/_{\mathrm{p}_{n+1}}. \tag{12}$$

The porosity of the face of the liner normal to the direction of wave propagation (σ_c) is given by:

$$\sigma_c = \frac{\pi d_c{}^2}{4}/A_l\,. \tag{13}$$

σ_c is simply the open area of a channel divided by the entire surface area of the face normal to the wave propagation direction. The total admittance β_t is then found by multiplying the number of channels $\mathrm{n_c}$ with the porosity σ_c and the individual channel admittance β_c for each of the unique cavities in the liner, then adding those together.

$$\beta_t = \sum \mathrm{n}_c \sigma_c \beta_c \tag{14}$$

The total impedance z_{tot} is the inverse of the total admittance β_t, given by:

$$\mathrm{z}_{tot} = {}^{1}/_{\beta_t}. \tag{15}$$

Finally, the absorption coefficient α can be calculated.

$$\alpha = \frac{4 * \mathrm{Re}[z_{tot}]}{(\mathrm{Re}[z_{tot}] + 1)^2 + \mathrm{Im}[z_{tot}]^2} \quad (16)$$

"Re" denotes the real part of the impedance, also known as the acoustic resistance R. "Im" denotes the imaginary part of the impedance, also known as the acoustic reactance X. This ZKTL theory was used to model the absorption coefficient spectrum for each of the liner design configurations investigated in this thesis that meet the required locally reacting and low-reduced frequency assumptions.

2.3 Low-Frequency Performance (LFP) Factor Definition

Each of the new designs developed in the study has a unique absorption coefficient spectrum with multiple desirable absorption characteristics such as bandwidth, and peak magnitude. In order to directly compare designs using a single composite metric, a non-dimensionalized metric was developed termed the Low-frequency Performance (LFP) factor. A liner's LFP is directly calculated from the absorption coefficient spectrum characteristics either predicted by the ZKTL code or measured experimentally, and is defined as follows:

$$LFP = \frac{\beta M}{\zeta} 100. \quad (17)$$

β is the lowest continuous frequency bandwidth where the absorption coefficient α is greater than the minimum absorption threshold (set at 0.6 for all designs considered). M is the maximum peak value of the absorption coefficient within the bandwidth, β. ζ is the lower bound of the bandwidth β. The multiplication factor of 100 is included to avoid rounding errors. The higher the LFP, the better absorption performance a liner is considered to have. The LFP factor could

further be tailored using weightage factors or functions for specific consistent sub-metrics. This could lead to a versatile single acoustic metric to compare alternative designs for various performance or source characteristics requirements. Moreover, but including mechanical properties such as liner volume and mass per unit-cell or compressive stiffness and strength, this approach could be augmented to arrive at a holistic liner performance factor or index. This tailored metric will help automate evaluation of design iterations using the software tool for problem specs that could have potentially vast design spaces.

2.4 3D Folded Cavity Packing Optimization Procedure

One of the most challenging aspects of designing an acoustic liner with folded internal cavities is determining the most efficient way to pack the folded cavities in a given 3D volume. When only 2D folded cavities are considered, the space is not efficiently used. As part of the study, a 3D Folded Cavity Packing Optimization (FCPO) code was developed to determine the most efficient way to pack 3D folded cavities into a given volume. The FCPO code is implemented using Wolfram's Mathematica Link to run the Mathematica ZKTL code developed by NASA [24] in an Excel spreadsheet. This provides a single interface software tool to optimize the packing of 3D folded cavities.

Avaliable Liner Volume (length >= width)		
Avaliable Liner Length [in]	Avaliable Liner Width [in]	Height [in] (without face sheet)
2	2	1.5

Absorption Performance Parameters		
Desired Bandwidth - β=	100	[Hz]
	0.6	Minimum acceptable α
Target Frequency	354	[Hz]

Minimum Wall Thickness [mm]	Number of Cells (Length direction)	Number of Cells (Width direction)
1.50	6	6

Atmospheric Pressure [psi]	Ambient Temperature [K]	Face sheet thickness [in]
14.7	296.6	0.0625

Maximum Mass Allowance [lb]
0.5

Figure 25: Inputs snapshot of spreadsheet for the FCPO.

The first step in using the liner optimization code is to provide the necessary inputs, as shown in Figure 25, to the Excel sheet. The minimum wall thickness should be determined by the minimum thickness needed to ensure acoustic rigidity, which is dependent on the material used for the internal walls. Once the inputs are set, the code determines the possible cavity configurations that would result in three peaks in the absorption coefficient spectrum. Through a trial and error process at the beginning of the code development process, it was found that three peaks resulting from three distinct sets of resonator total cavity lengths tended to result in better LFP values than two or four peaks did.

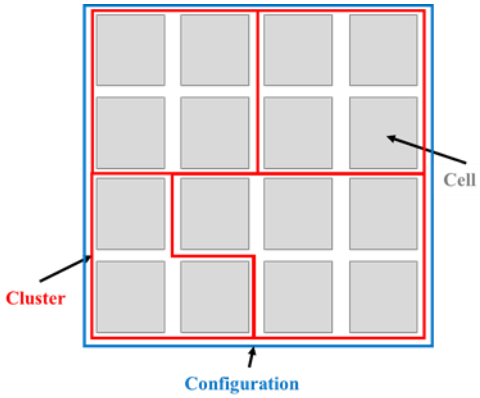

Figure 26: Visual representation of cell, cluster, and configuration notations, example liner top view shown.

Therefore, the total number of cells is divided into three distinct clusters (can be more than one of each cluster in the configuration) and assuming that each cluster is an integer number of cells. The size of each cell is determined by the minimum wall thickness and the number of cells in each direction. Figure 26 visually explains the 'cluster' and 'cell' notation. A cell is an individual open cavity if viewed from a top view (folding is not considered), while a cluster is a collection of connected cells that make a single folded cavity. In the preliminary selection, the three distinct clusters must have three consecutive integral number of cells. For instance, one could apportion a 6x6 configuration into 2 clusters of 5 cells, 2 clusters of 6 cells, and 2 clusters of 7 cells for a total of 36 cells with a configuration notation: [5(2), 6(2), 7(2)]. This is the preliminary configuration selected for the Optimized 3D Folded Cavity design from among other 3-cluster configurations based on simulations for further optimization. These configuration possibilities are narrowed down based on the input target frequency. Configurations for which the biggest cluster (longest cavity length) is not sufficient to reach the target frequency are immediately eliminated. Once the viable configuration option with clusters having integral number of cells is known, performance optimization for partial cell depths resulting from this configuration are done. For these partial

cell depth optimization runs, the total cavity length of the middle cluster is fixed, while the total cavity lengths for the shorter and longer of the three clusters are differentially varied over one cell depth to identify the configuration with the best performance. In the Optimized 3D Folded Cavity design case, the preliminary configuration, [5(2), 6(2), 7(2)] identified above was optimized to the final configuration, [5^{+}(2), 6(2), 7^{-}(2)]. Once each cavity length is known, an optimized face sheet is selected based on the same LFP selection criteria. After that, the design can move on to the manufacturing stage. Figure 27 shows a flow chart depicting the overall optimization process followed by the optimization code.

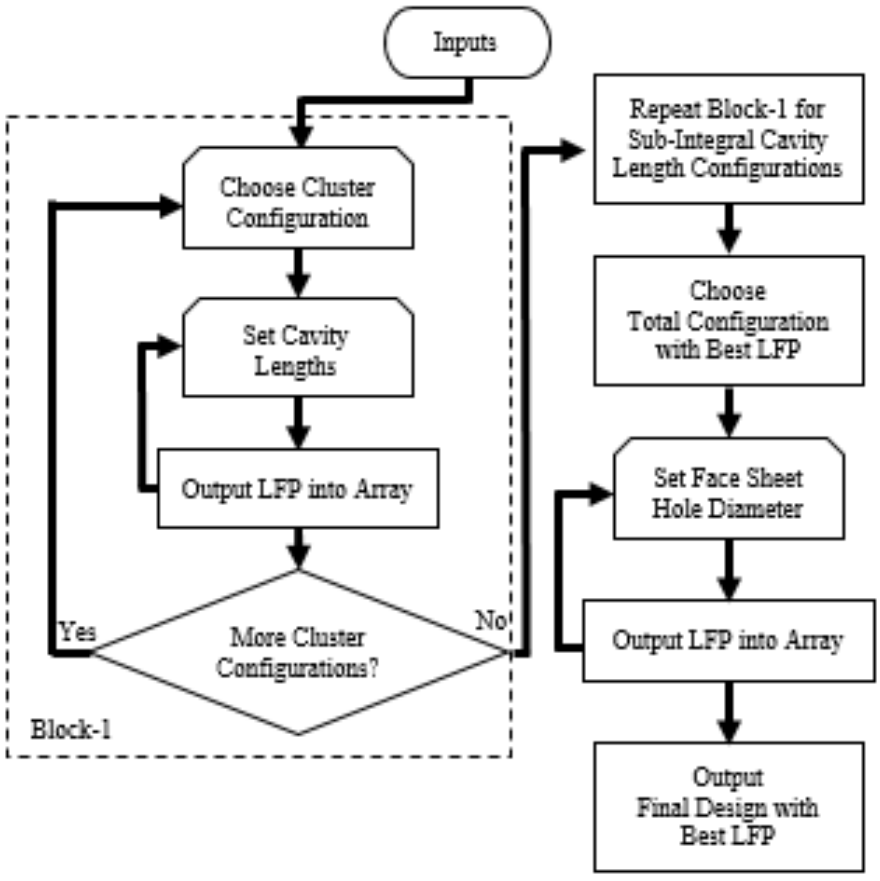

Figure 27: Folded cavity optimization code flow chart.

2.5 Liner Designs and Simulation Results

Several different folded liner design configurations were developed and tested as part of this study. In this section, the designs are introduced and explained, and the simulation results for the each of the designs is presented. Choice of liner dimensions were made based on the testing equipment, as well as dimensions of modern liners currently in use. Materials used in making the test articles were selected based on ease of manufacturing, as the liners tested are relatively small prototypes of full scale liners. The dimensions and materials used allowed for the exploration of complex folded cavity configurations as potential low-frequency liner solutions that are also lightweight, compact, and structurally-integrated. Dimensions shown are in inches unless otherwise labeled.

2.5.1 Quarter Wave Baseline Design

In order to provide a basis for comparison with a conventional core design, the Quarter Wave Baseline liner was made first. The first being a verification that the peak absorption as calculated by the ZKTL code would occur at the frequency expected according to the quarter wave resonance equation. The design has 25 straight cavities with no folds. The exact liner dimensions can be seen in Figure 28.

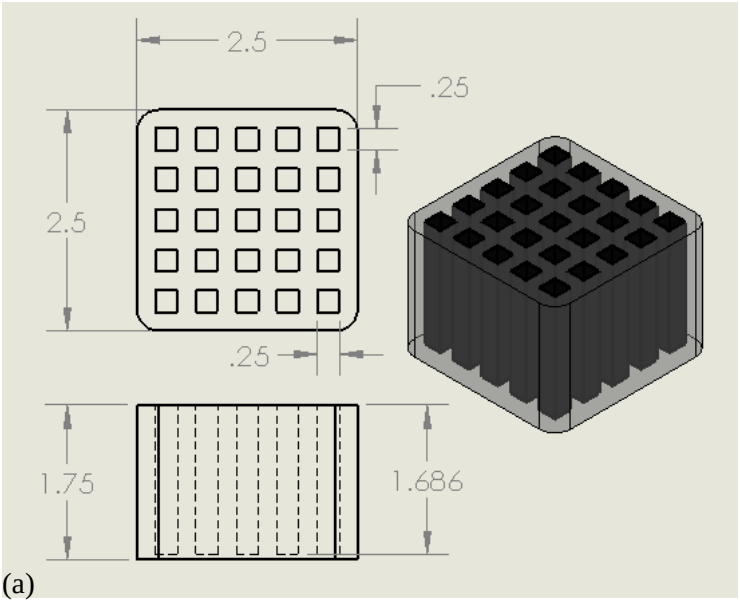

(a)

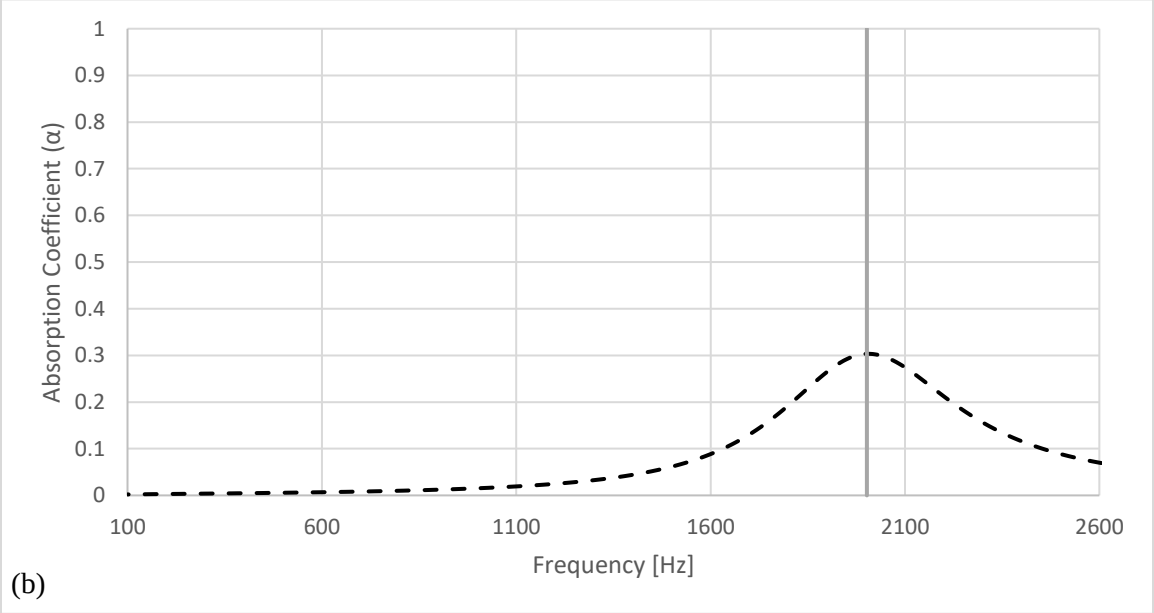

(b)

Figure 28: (a) Quarter Wave Baseline design and (b) ZKTL simulation results. (Δf =15 Hz)

Figure 28, shows the ZKTL simulation results along with a solid vertical line at the quarter wave design frequency (2002 Hz) corresponding to the depth of the cavity of 1.686 in..

$$f_1 = \frac{13504\ in/s}{4(1.686\ in)} = 2002\ Hz \tag{18}$$

2.5.2 Helmholtz Baseline Design

.In addition to the baseline design utilizing the quarter wave mechanism to absorb sound, a baseline design utilizing the Helmholtz resonance mechanism was also manufactured. This baseline serves as the comparison core for typical honeycomb liners in use currently. Unlike the 3D printed Quarter Wave Baseline, the Helmholtz Baseline was manufactured using an aluminum honeycomb core, much like a conventional SDOF liner. The honeycomb core used was 2 inches thick with an average cell diameter of approximately 0.56 inches. Ten total cells were able to fit within the allowed 2.5 in x 2.5 in cross sectional area. Each of the face sheet holes were drilled into the 1/16 inch thick plate with a 1/16 inch diameter drill bit. A picture of the Helmholtz Baseline test article can be seen in Figure 29.

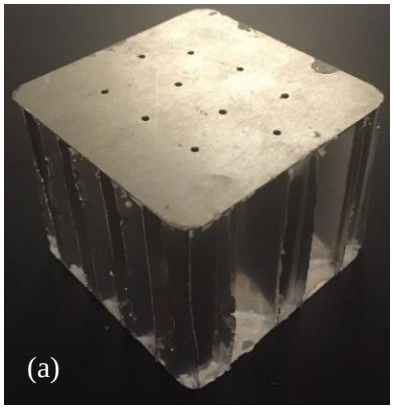

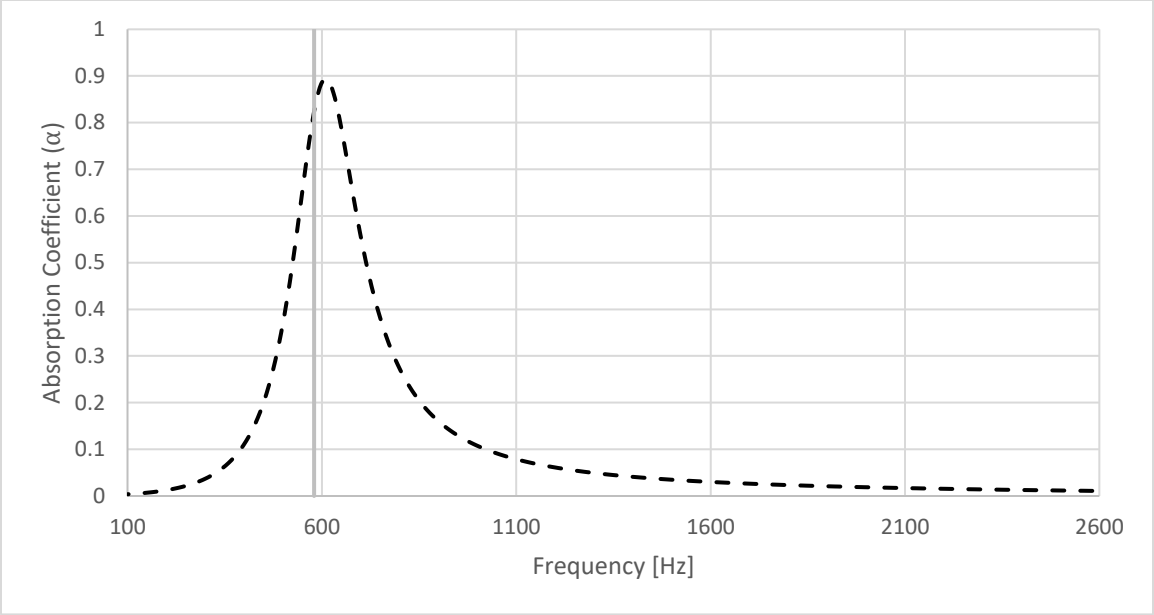

Figure 29: (a) Helmholtz Baseline design and (b) ZKTL simulation results. (Δf =15 Hz)

Figure 29 shows the ZKTL simulation results along with a solid vertical line at the resonant frequency (580 Hz) calculated by the following equation. Good agreement is observed between the two.

$$L' = 0.0625\ in + 0.48\left(\frac{\pi}{4}(0.0625\ in)^2\right)^{\frac{1}{2}}\left(1 - 1.25\frac{0.0625}{0.56}\right) = 0.0854\ in \tag{19}$$

$$f = \frac{13504\ in/s}{2\pi}\sqrt{\frac{\frac{\pi}{4}(0.0625\ in)^2}{(2\ in)\left(\frac{\pi}{4}(0.56\ in)^2\right)(0.0854\ in)}} = 580\ Hz \tag{20}$$

2.5.3 L-Liner Design

The L-Liner design is the first design developed in this study that incorporates folded cavities. The same total volume used for the Quarter Wave Baseline design is used for the L-Liner. In this design, there exists six rows with the same five different cavities in each row, for a total of thirty cavities. Four cavities in each row have the same square cross-sectional area, while the remaining cavity in each row has a much higher aspect ratio. The porosity (ratio of open cavity area to total active area) of this design is much higher than the two baseline designs. The motivation behind this design was to see how the absorption spectrum would behave when not every cavity length was equal. A straight cavity baseline with the same hole pattern as the L-Liner was additionally used for comparison. A wider frequency bandwidth of absorption was expected with the L-Liner design. Comparison of L-Liner and its baseline ZKTL simulation results are shown in Figure 30.

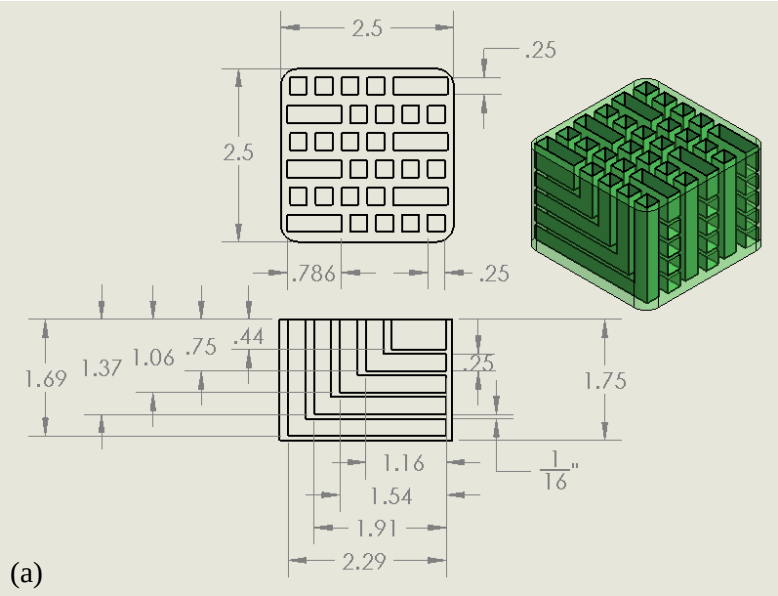

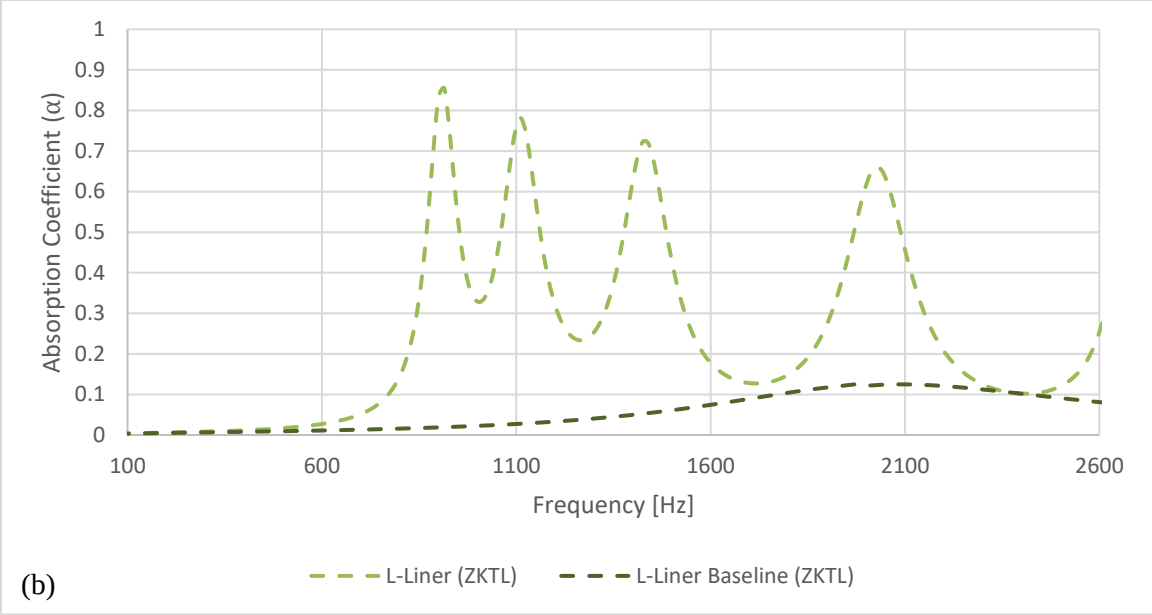

Figure 30: (a) L-Liner design and (b) ZKTL Simulation results for the L-Liner and its baseline. (Δf =15 Hz)

Simulation results show that my having multiple cavities of different lengths within the same liner, broadband absorption can be achieved. However, this 2D folded cavity design is limited to frequencies >500 Hz.

2.5.4 U-Liner Design

Stemming from the problem definition, the U-Liner design occupies the same volume as the Quarter Wave Baseline 1 and the L-Liner designs. This design incorporates an additional fold from the L-Liner to create 2D 'U' shape folded cavities. Thus, the cavity length is effectively doubled from the baseline design while maintaining the same liner volume. The total cavity length of each cavity for the U-Liner is 3.372 inches. In addition to testing the U-Liner as a quarter wave resonator, a face sheet was added to cause the liner to transition to a Helmholtz type liner. A new straight cavity baseline liner was also created that has the same number of holes (25)

with the same cavity diameter as the U-Liner for comparison. Another change with this liner is that one row is rotated 90° from all of the other rows. This was done to create a perfectly symmetrical hole pattern on the face of the liner. In order to do that, the cross sectional area of the secondary cell (post folded) for each of the cavities in the rotated row was decreased slightly. This led to the appearance of a slight double peak near the apex of the absorption coefficient spectrum for the quarter wave U-Liner simulation as shown in Figure 31.

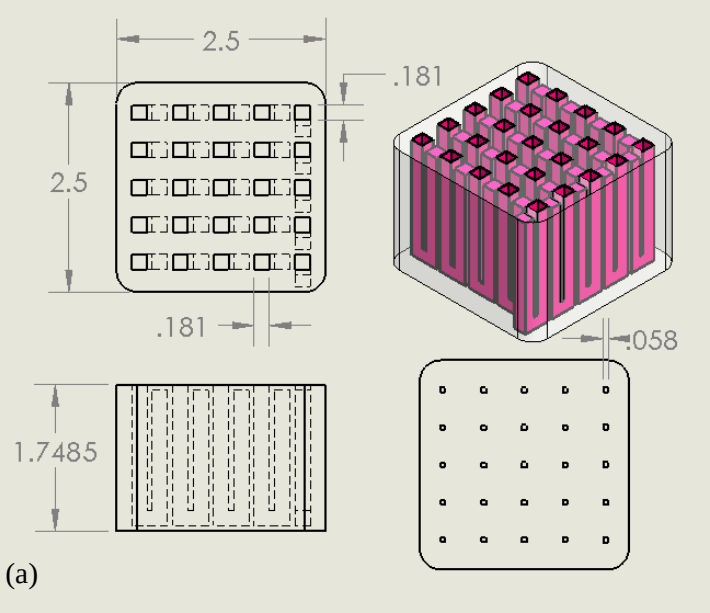

(a)

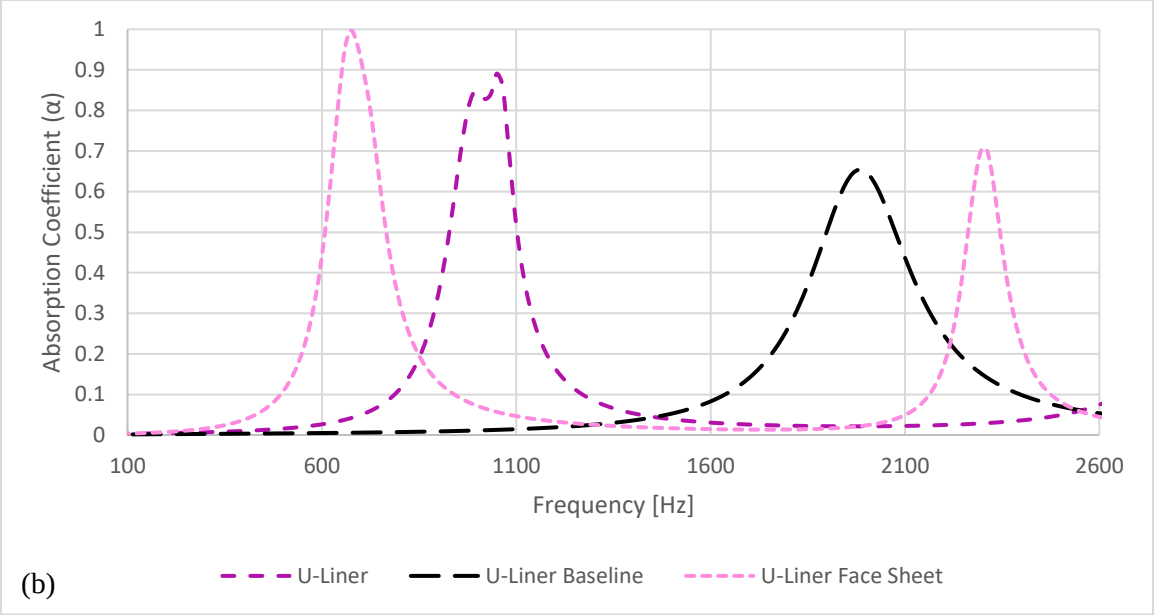

Figure 31: (a) U-Liner design and (b) ZKTL simulation results, different configurations shown. (Δf =15 Hz)

Simulation results in Figure 31 show that a significant shift to lower frequencies occurs for both the U-Liner, and the U-Liner with a face sheet from the U-Liner baseline design.

2.5.5 Phased Slanted U-Liner Design

The Phased Slanted U-Liner is the only non-locally reacting liner designed considered in research. The intention was to see what would happen if the U-Liner cavities were slightly slanted to increase the totally cavity depth, then allowed to communicate with adjacent cavities through connecting holes. A baseline Slanted U-Liner was printed along with the Phased Slanted U-Liner to directly compare the effect that the communicating holes had on the performance of the liner. The baseline made for comparison with this design is the exact same design except for the interior cavity connecting holes, so instead of having straight cavities, the slanted feature was included in the baseline. A 1/16 inch thick face sheet was also added to the Phased Slanted U-Liner with

0.058 inch diameter holes centered at the opening of each cavity. Because the ZKTL code can only simulate locally reacting liners, the Baseline Slanted U-Liner is the only simulation prediction for this design. The experimental results from the non-locally reacting configurations are compared with the locally reacting case in Chapter 3.

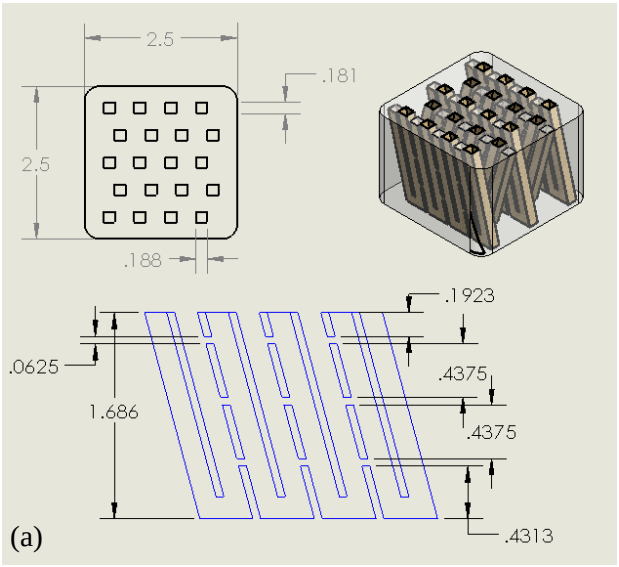

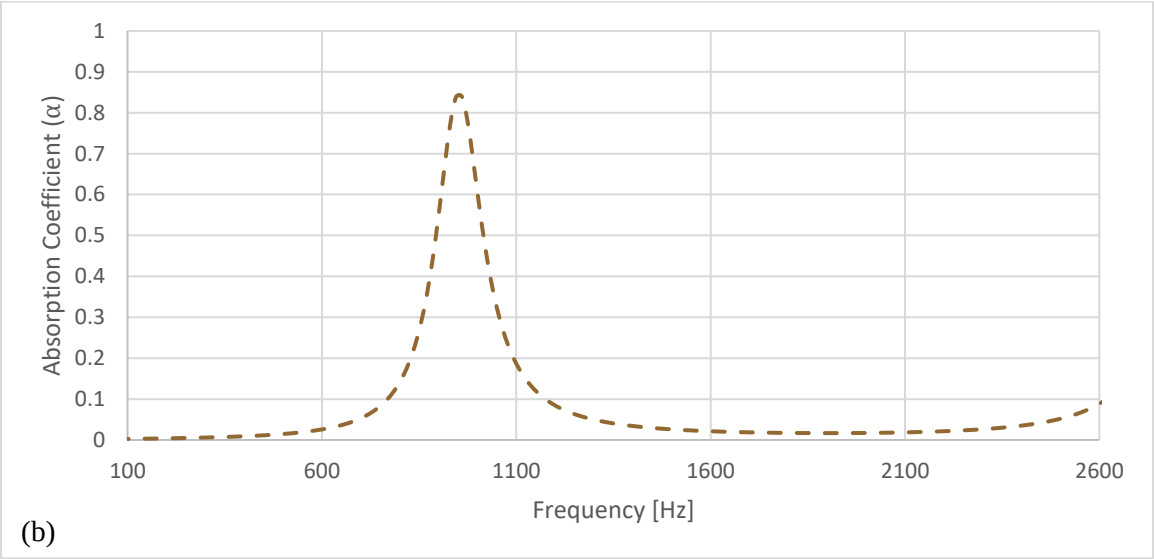

Figure 32: (a) Phased Slanted U-Liner design and (b) ZKTL simulation results. (Δf =15 Hz)

The simulation results in Figure 32 show an absorption peak for the locally reacting baseline case at approximately 960 Hz.

2.5.6 W-Liner Design

The W-Liner extends the same concept as the U-Liner, except that additional folds are introduced causing the cavity to make a ‘W’ shape instead of a ‘U’ shape, this allows more folds into a single cluster. The W-Liner occupies the same volume of the previous 3D printed designs discussed in this section. The W-Liner is essentially able to quadruple the length of the standard straight cavity liner in the baseline design. The total length of each cavity in the W-Liner is 6.54 inches. A new straight cavity baseline liner with the same cavity size as the W-Liner is used as a comparison to the W-Liner. Another feature to note in the ZKTL absorption spectra shown in Figure 33, is that peaks also occur at the higher harmonic frequencies corresponding to the particular cavity length. A 1/16 inch thick face sheet with 0.058 inch diameter holes was also added and simulated.

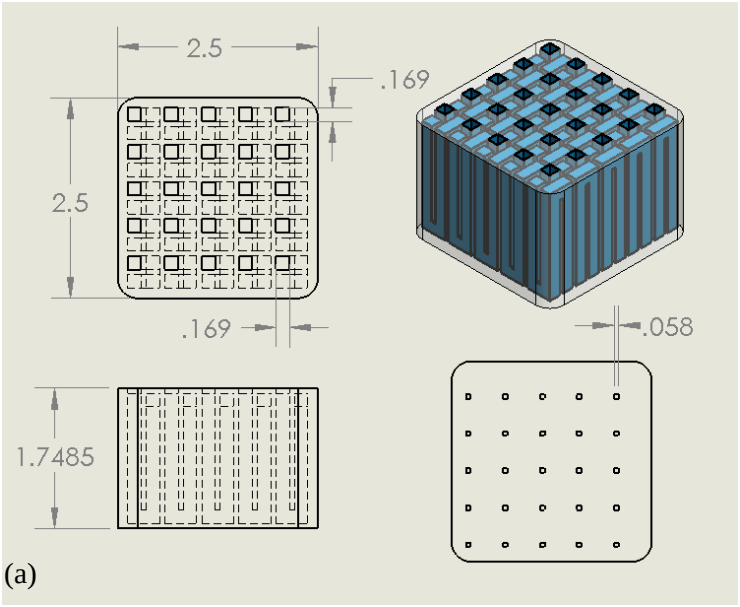

(a)

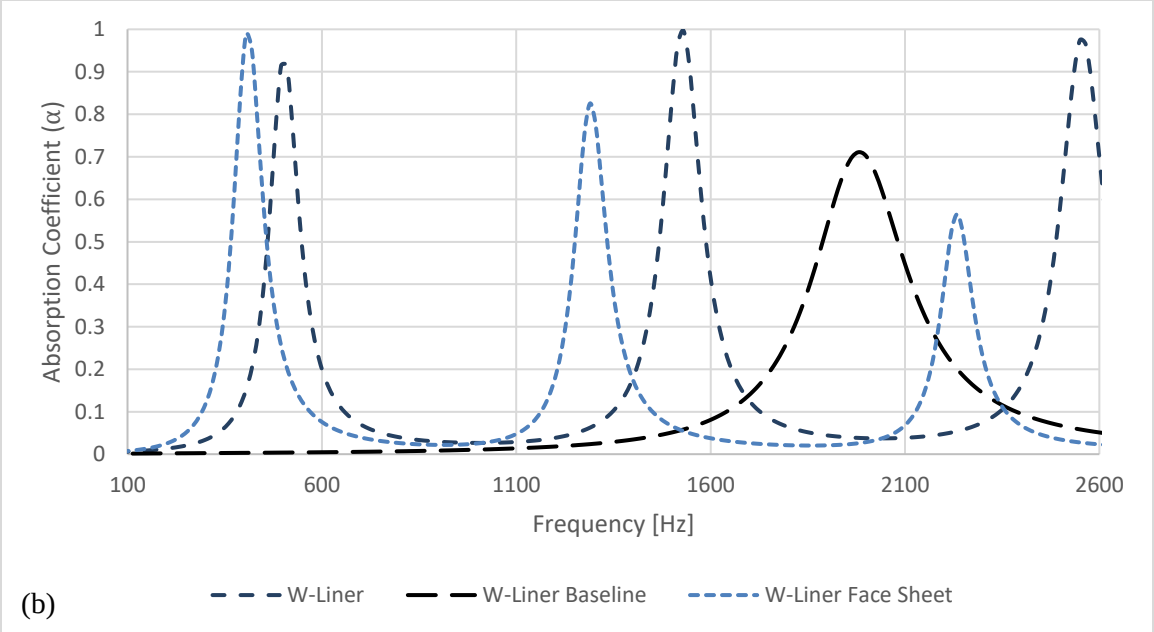

Figure 33: (a) W-Liner design and (b) ZKTL simulation results. (Δf =15 Hz)

The simulation results shown in Figure 33 show that excellent absorption is obtained below 500 Hz. A significant shift to lower frequencies is seen in the W-Liner and W-Liner with face sheet designs from the straight cavity W-Liner baseline design.

2.5.7 Circle Spiral Design

The Circle Spiral design refers to a design in which each cavity follows a spiral path along a cylindrical shaft. The goal was to create a liner with 25 equal cavities (like the Quarter Wave Baseline, U-Liner, and W-Liner) that occupied the same volume as the previous locally reacting 3D printed liners discussed, but with much longer cavities. By using the spiral geometry, the cavity length of each of the cavities in this design is 33.2% longer than the cavity length of each cavity in the W-Liner design. This allows for an even lower frequency to be reached, with the

lowest peak occurring at 375 Hz. Because of its spiral shape, manufacturing this design could be potentially challenging however.

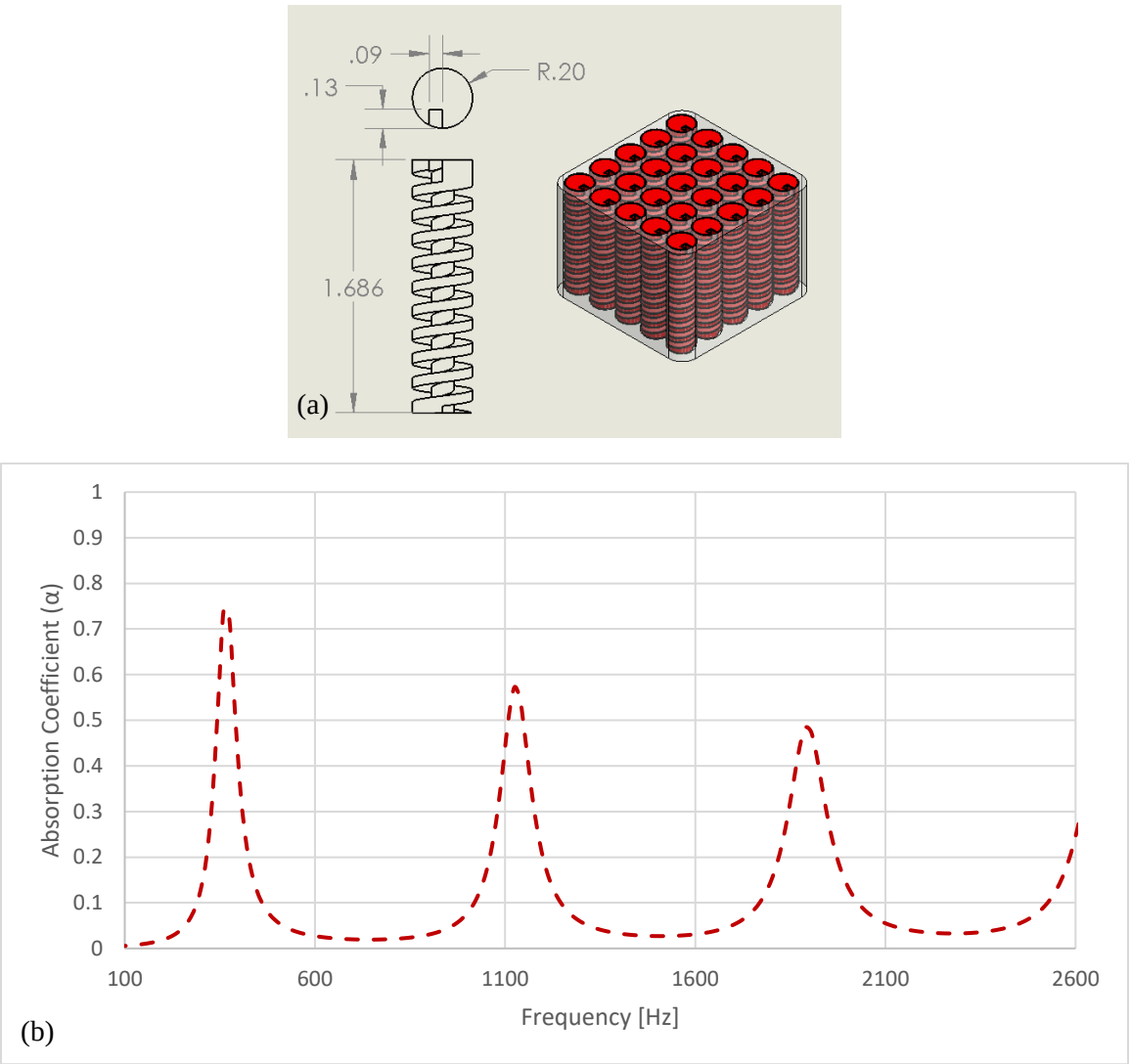

Figure 34: (a) Circle Spiral design and (b) ZKTL simulation results. (Δf =15 Hz)

Simulation results in Figure 34 show that a single absorption peak below 500 Hz should be observed with this particular liner design.

2.5.8 Square Spiral Design

The Square Spiral design is the same concept as the Circle Spiral design, with the exception of the spiral cavity following a path around a square shaft instead of a circular one. This could potentially be easier to manufacture than a circular spiral design. Unlike the Circle Spiral, the Square Spiral has right angle turns inside the cavity. The cavity size is kept the same as in the Circle Spiral design, but the overall cavity length is slightly greater than that for the Circle Spiral, causing the first peak in the absorption coefficient spectrum to occur at 285 Hz.

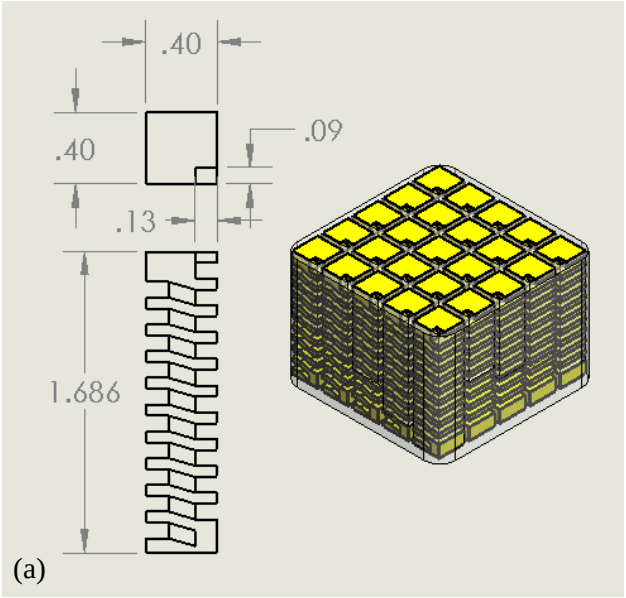

(a)

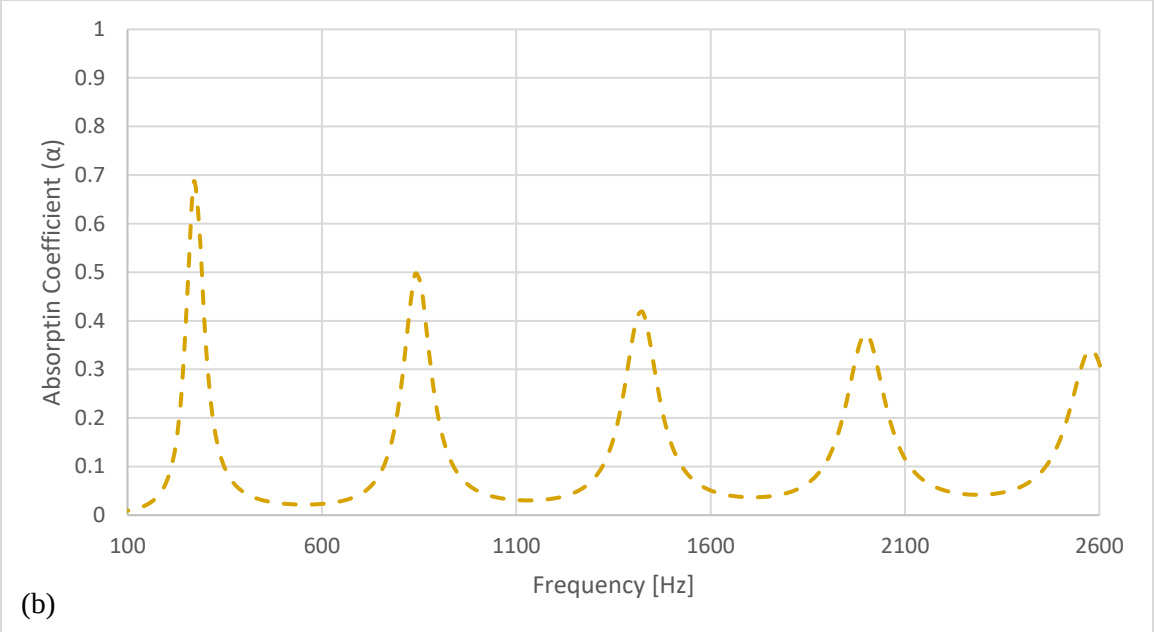

Figure 35: (a) Square Spiral design and (b) ZKTL simulation results. (Δf =15 Hz)

Simulation results from Figure 35 show that much like the Circle Spiral design, a single absorption peak below 500 Hz can be expected from this design.

2.5.9 Broadband Square Spiral Design

Since the Square Spiral was able to achieve a lower frequency than the Circle Spiral and could be relatively easier to manufacture, the square-type spiral was chosen for a broadband spiral design. Instead of having 25 cavities of equal length like in the Square Spiral and Circle Spiral designs, 25 cavities with 5 unique lengths were designed in an attempt to increase the bandwidth of absorption. Figure 36 shows each of the unique cavities with the frequency they were designed to target. The same volume restriction was enforced for this design as used for the other locally reacting liners discussed up to this point.

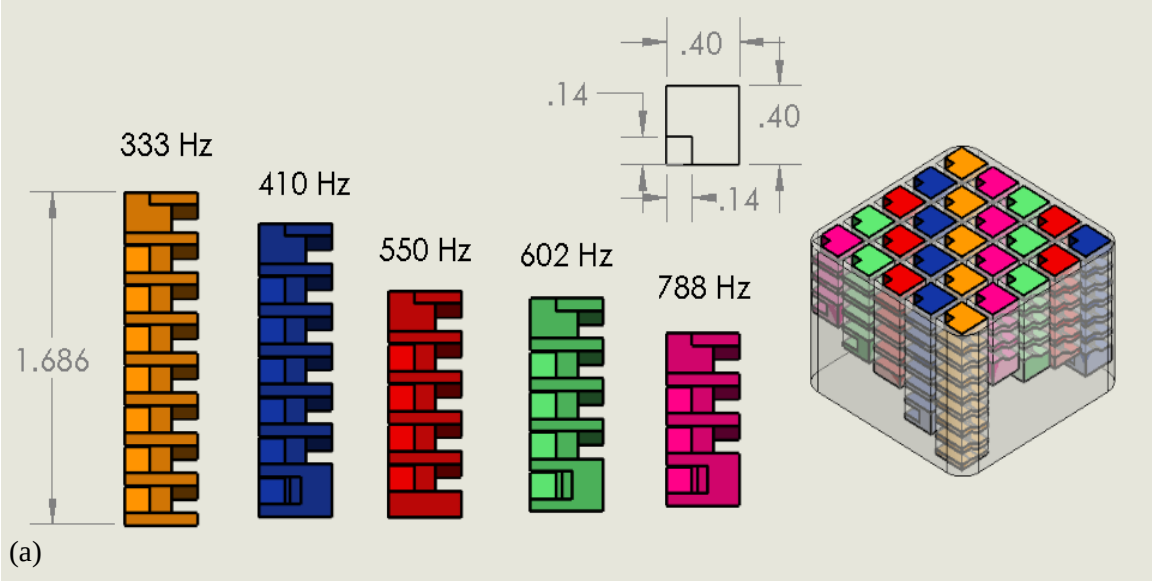

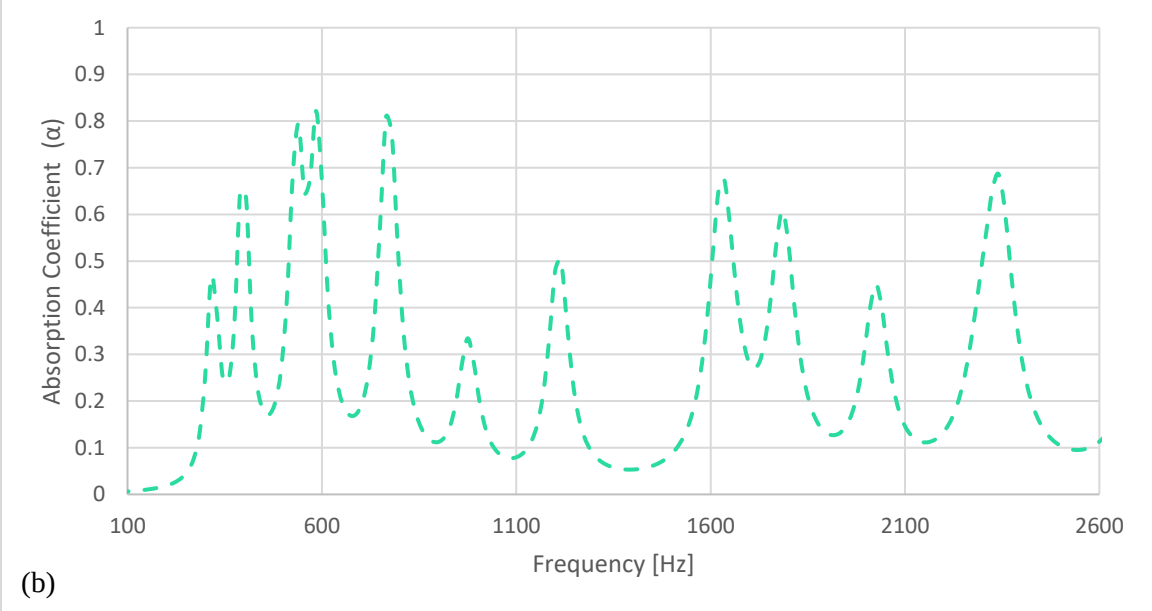

Figure 36: (a) Broadband Square Spiral design and (b) ZKTL simulation results. (Δf =15 Hz)

Simulation results in Figure 36 show that low magnitude absorption below 500 Hz can be achieved. This design demonstrated sub-optimal use of the available liner volume as well.

2.5.10 Broadband Spiral Insert Design

The Broadband Spiral Insert was also designed to utilize 5 different spiral cavity lengths to achieve a wide bandwidth of absorption. However, instead of a having a square geometry, this design uses a hexagonal geometry in order to act as an insert into a traditional honeycomb core. By using an aluminum honeycomb core as the primary structure, this design would weigh less than the 100% printed Broadband Square Spiral design, while maintaining adequate stiffness. Due to the hexagonal shape, the spiral path was changed to traverse in a circular pattern. The open cavity cross sectional area was kept the same as in the Broadband Square Spiral design, but due to the change in geometry (square to hexagonal) the overall cavity lengths had to be shortened. One further change is the overall liner thickness from approx. 1.75 inches to 2 inches. This change in thickness is so that the inserts could fit into the same 2 inch honeycomb used for the Helmholtz Baseline design. Figure 37 shows how the Broadband Spiral Insert design would be integrated with the aluminum honeycomb core.

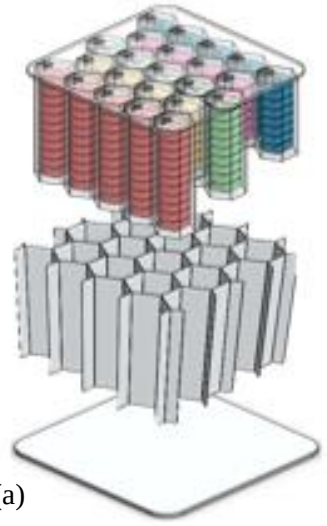

(a)

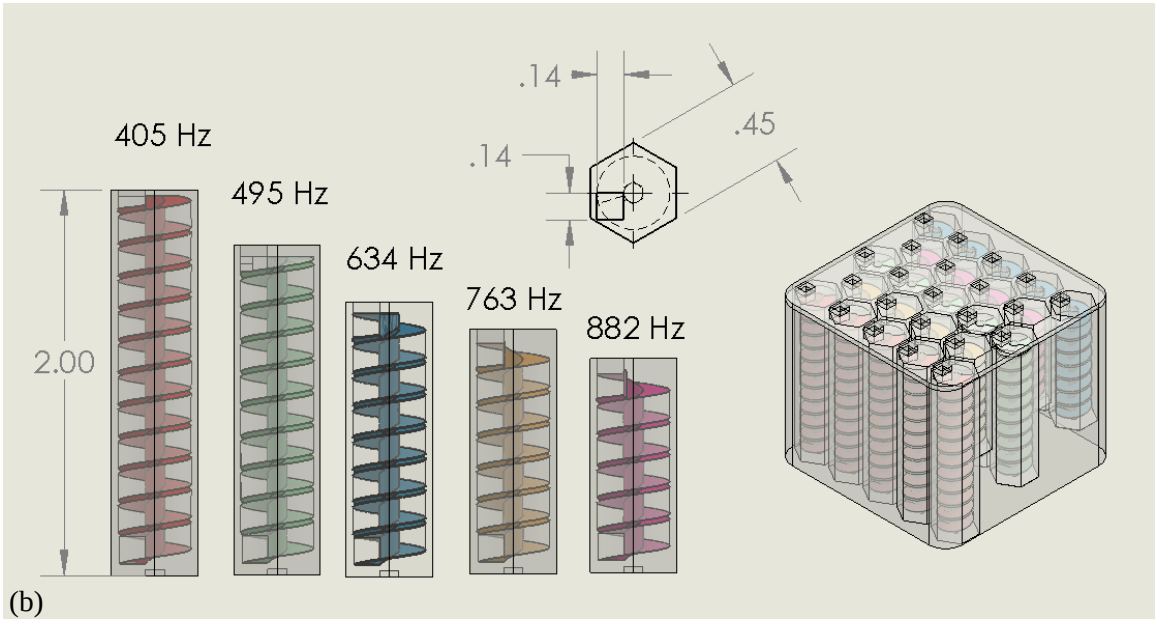

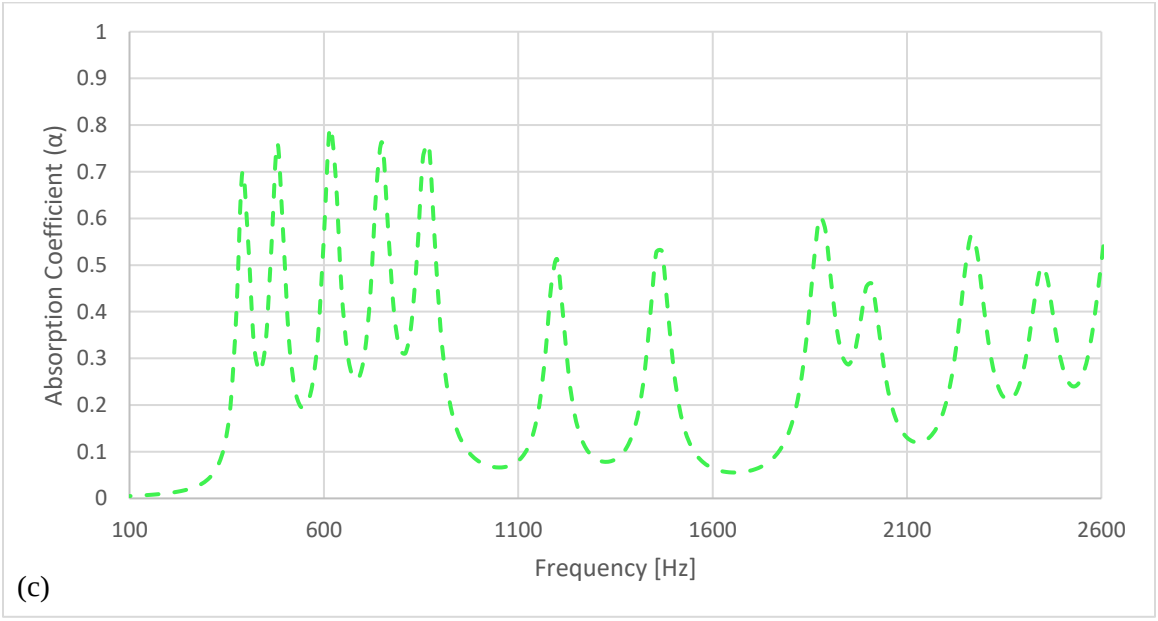

Figure 37: (a) Broadband Spiral Insert exploded assembly, (b) design, and (c) ZKTL simulation results. (Δf =15 Hz)

Results from the ZKTL simulation in Figure 37 show that by spacing the cavity lengths in a broadband design approximately the same amount, each of the distinct peaks corresponding to

those cavity lengths has approximately the same absorption magnitude. By incorporating the spiral cavities with a honeycomb core, the lightweight, compact, structurally-integrated aspects of the problem definition are satisfied.

2.5.11 Triangle 10-Fold Insert Design

The Triangle 10-Fold liner was also designed to be an insert into a 2 inch thick honeycomb core. The nomenclature ’10-Fold’ come from the fact that each cavity changes direction a total of 10 times. Three distinct cavities were designed to target three frequencies spaced approximately 100 Hz apart. This insert design has a triangle shaped cavity to most efficiently use the hexagonal geometry of the honeycomb. Instead of the cavity following a spiral path along the height of the cavity like the Broadband Spiral Insert design, the cavity follows a triangular patch such that the amount of 3D printed material needed is minimized. The interior wall thickness between cells is 0.2 mm thick, which is assumed acoustically rigid in the ZKTL simulations.

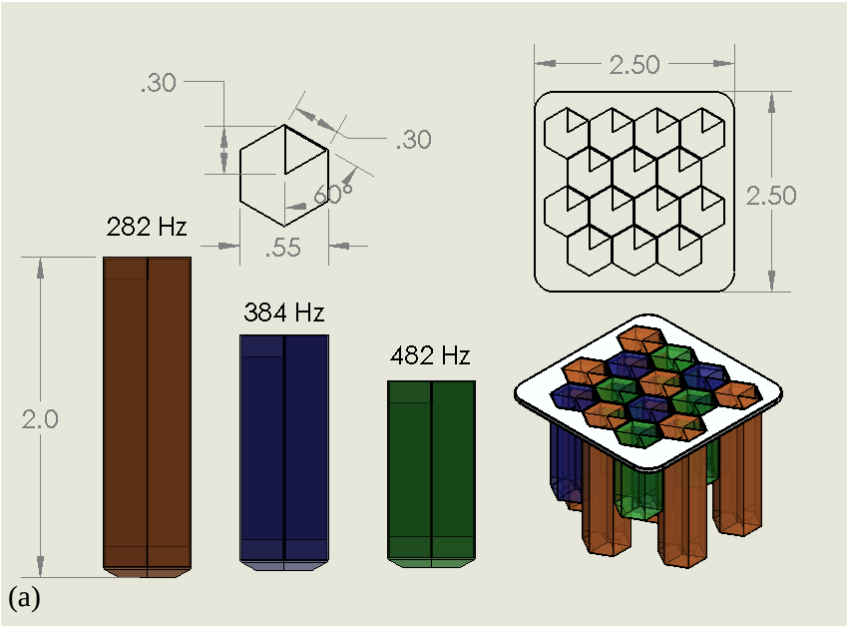

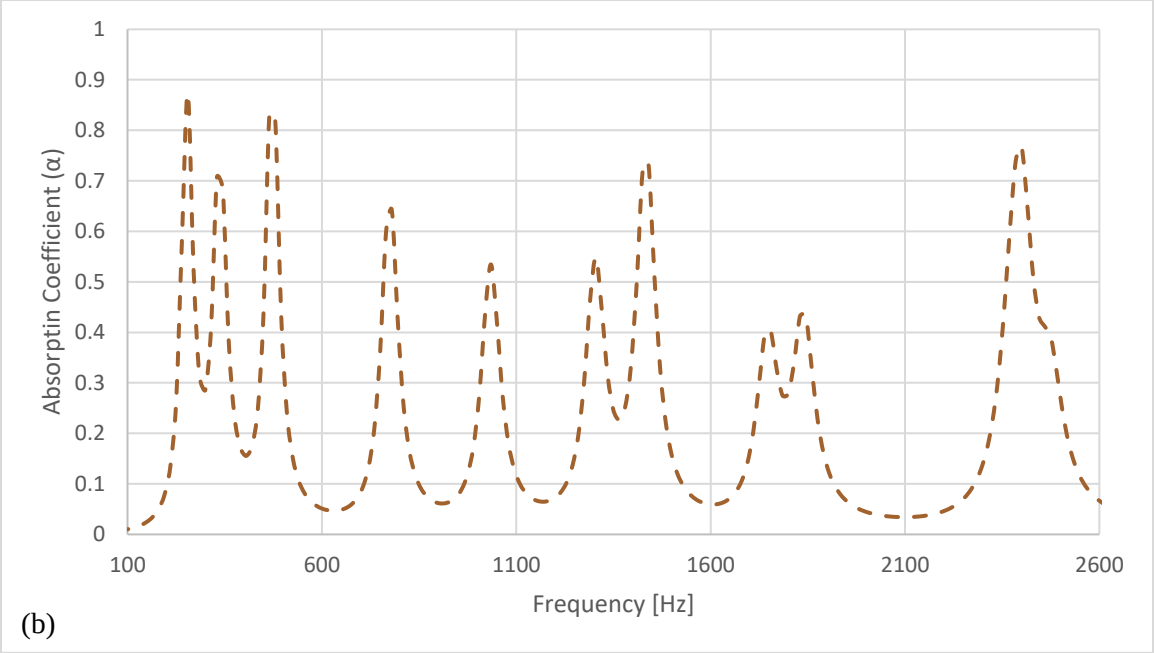

Figure 38: (a) Triangle 10-Fold Insert design and (b) ZKTL simulation results. (Δf =15 Hz)

ZKTL simulation results in Figure 38 show three distinct peaks at their analytically predicted locations, which are all < 500 Hz.

2.5.12 Hypothetical Teardrop Design

Hypothetical teardrop cell honeycomb-like designs were investigated as another potential design solution. These designs were motivated by recent Amorphous Metal Honeycomb (AMH) technology [34]. AMH technology was proposed to be used in the construction of new lightweight acoustic liners. Figure 39 shows important steps in the AMH manufacturing process. Essentially, a ribbon of very thin metal is woven around pegs to create a repeating teardrop shape that has a very high specific strength. This type of honeycomb could potentially be used instead of currently used high strength aluminum composites to provide better specific strength.

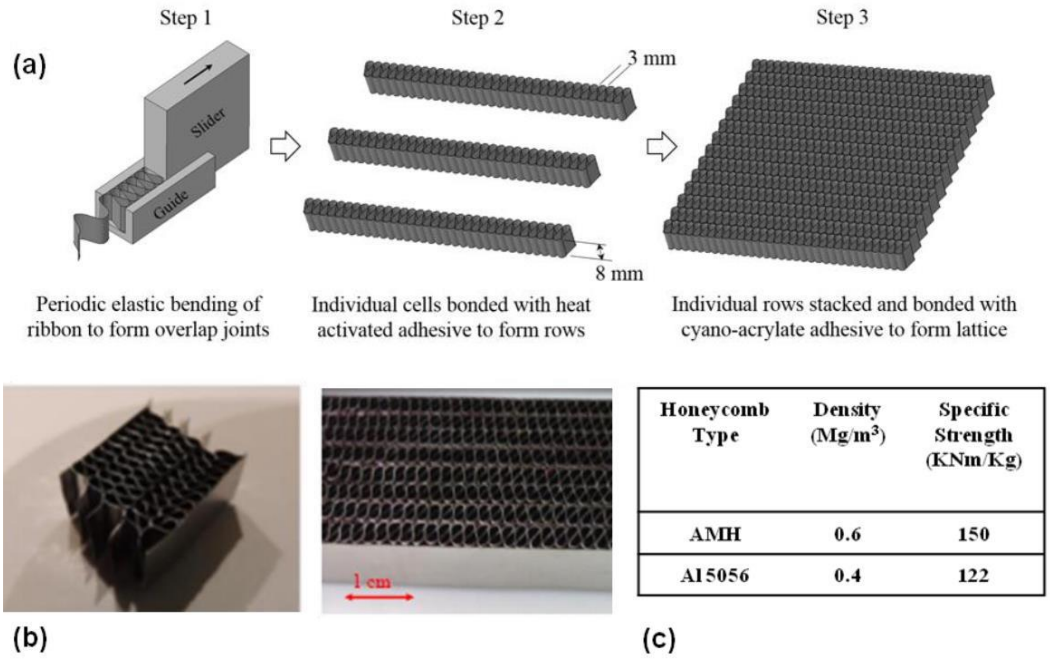

Honeycomb Type	Density (Mg/m^3)	Specific Strength (KNm/Kg)
AMH	0.6	150
Al5056	0.4	122

Figure 39: (a) Schematic of AMH manufacturing process, (b) lab scale prototypes of AMH, (c) comparison of AMH and highest strength conventional aluminum honeycomb commercially available. [34]

In order to effectively use this technology for a low-frequency acoustic liner, the folded cavity architecture should be integrated with this core. By precisely cutting the ribbon in specific locations either a) before the ribbon is woven, or b) after a sample is created, specific adjacent cavities can be made to communicate acoustically to create the desired folded cavity design. Based on this approach, 12 different cluster configurations for an 81 cell, 2.5 inch x 2.5 inch AMH core were designed and compared using the LFP factor resulting from the ZKTL simulation. Results from this comparison are shown in Table 2, with the configuration notation A(B) where A is the number of cells connected in a cluster and B is how many of those clusters are in the configuration. Note that all the simulation results used for the comparison were made assuming that the first cavity hole in each cluster has a completely open area. In other words, the

face sheet hole size is the same area as the cavity area. Comparison showed that Sim12 and Sim10 were the most promising designs as seen from Table 2.

LFP Rank – based on ZKTL simulation results				
Rank	Simulation	LFP Factor	Configuration	Peak α
1	12	83.58	10(2), 9(3), 8(5), 7(5), 6(3), 5(2)	0.971
2	10	65.91	9(5), 8(5), 7(5), 6(5)	0.973
3	11	63.52	10(5), 8(5), 7(5), 5(5)	0.992
4	3	51.32	6(15), 5(5), 4(5), 3(5)	0.96
5	7	50.57	10(5), 8(5), 6(10)	0.99
6	4	49.20	6(10), 5(10), 4(10)	0.98
7	9	16.69	8(10), 7(10)	0.985
8	8	13.58	10(10), 6(5), 4(5)	0.755
9	6	12.43	10(9)	0.774
10	5	10.50	6(5), 5(10), 4(10), 3(10)	0.985
11	2	0	6(20), 3(10)	0.33
12	1	0	6(25)	0.43

Table 2: Hypothetical Teardrop configuration comparison.

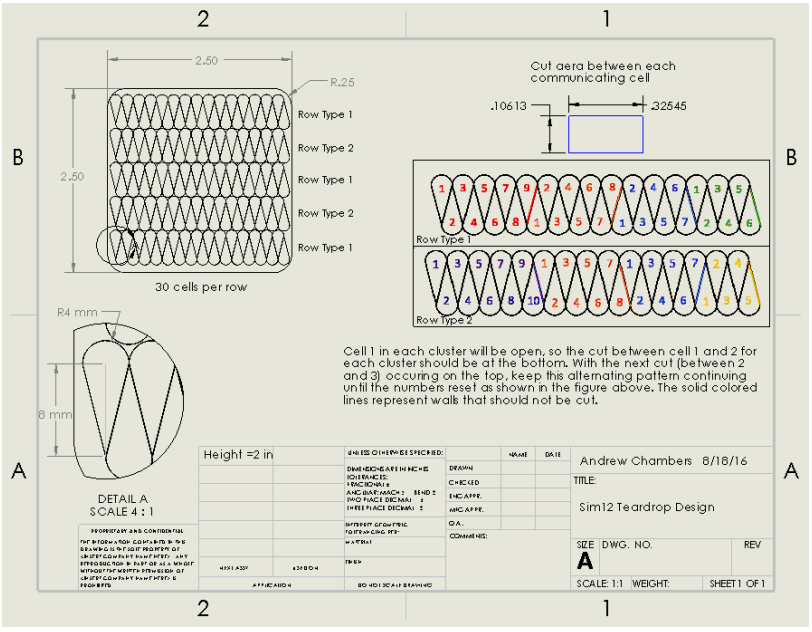

Figure 40: Sim12 teardrop core configuration design drawing, dimensions not otherwise labeled in [in].

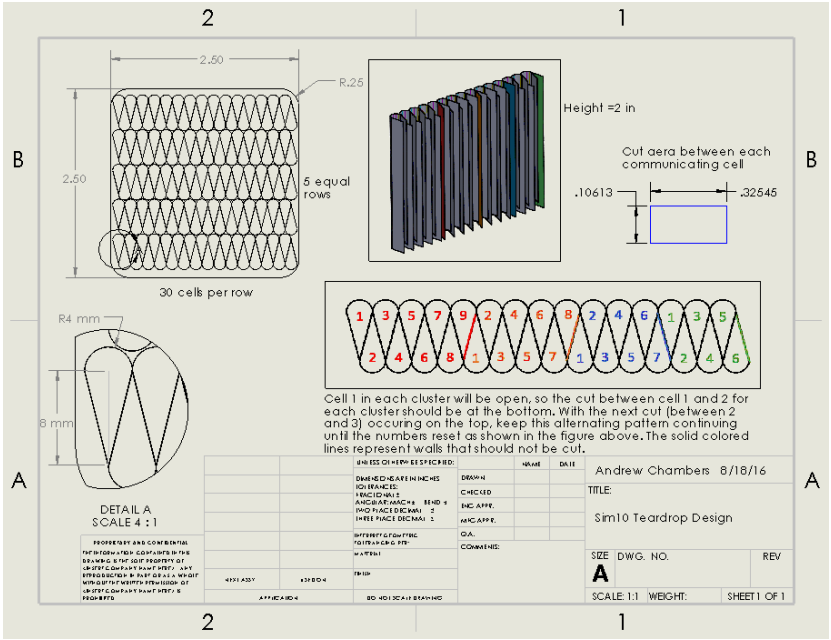

Figure 41: Sim10 teardrop core configuration design drawing, dimensions not otherwise labeled in [in].

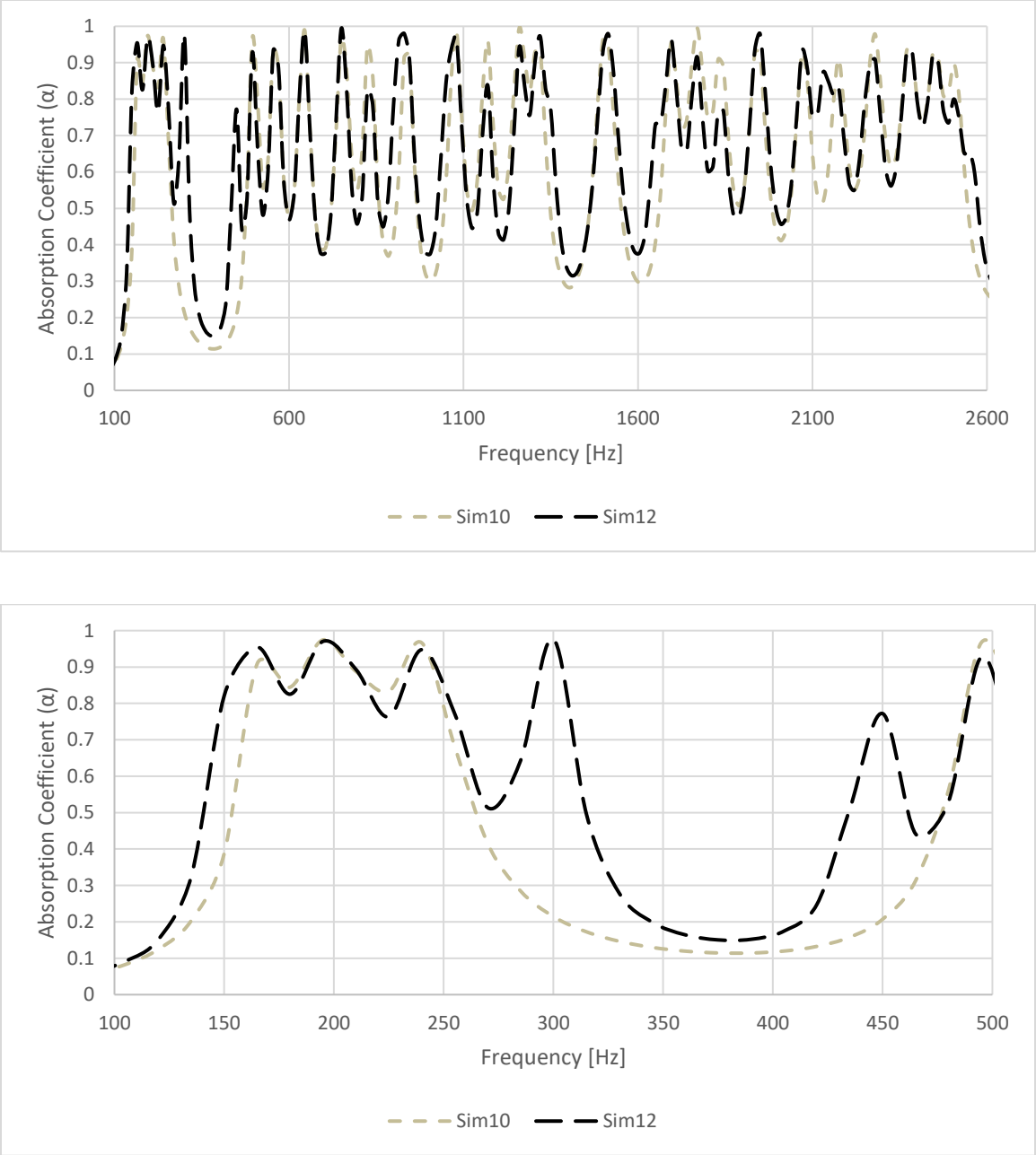

Figure 42: ZKTL simulation results for the selected Hypothetical Teardrop configurations. (Δf =15 Hz)

The simulation results shown in Figure 42 show exceptional low-frequency broadband performance below 500 Hz. The presence of good absorption from the higher frequency

harmonics in addition to the good low-frequency absorption could potentially be used for ultra-broadband applications. This seems to be in agreement with results found by Sugimoto et al. [8]. The high frequency performance is not compromised by folding the cavities. The cell and cluster configurations are what drives the simulated performance of these designs. The teardrop cell shape does not affect the simulation.

2.5.13 Sintered Folded Cavity Designs

Based on previous folded liner designs, proof of concept for optimized low-frequency configuration having square cavities that can be easily made using additive manufacturing were investigated. In an attempt to get better broadband absorption using 3D printed folded cavity liners, 7 new design configurations were created. These initial designs were made with the intention of using SLS (Selective Laser Sintering) instead of extrusion-type printing used for the previous samples. Thus the name “Sintered Folded Cavity” designs. Each of these utilize an active area of 2.5 inches x 2.5 inches with 81 total cells. Each cell has a 5.5 mm x 5.5 mm square cross sectional area with a consistent internal wall thickness of 1 mm. Additionally, the total thickness of each of the Sintered Folded Cavity designs is 1.5625 inches (1.5 inch thick core + 1/16 inch face sheet). The 7 different configurations were simulated using the ZKTL model and their respective LFP factors were compared to determine which liners should be manufactured and tested. Comparison of LFPs can be seen in Table 3 with the configuration notation following the same format as explained in the previous section.

LFP Rank – based on ZKTL simulation results					
Rank	**Simulation**	**Name**	**LFP Factor**	**Configuration**	**Peak α**
1	7	S7	25.22	10(3), 9(3), 8(3)	0.775
2	2	S2	16.98	9(4), 8(3), 7(3)	0.82
3	1	S1	16.35	10(2), 9(5), 8(2)	0.9
4	3	S3	15.74	9(3), 8(4), 7(2), 4(2)	0.78
5	6	S6	13.85	9(9)	0.96
6	5	S5	13.17	12(4), 11(3)	0.795
7	4	S4	4.02	9(3), 8(2), 7(2), 6(4)	0.72

Table 3: Sintered Folded Cavity design configuration comparison.

Each sample was simulated with a 1.5 mm, 2 mm, 2.5 mm, and 3 mm face sheet configuration. S7, S2, S6, and S5 were chosen to be manufactured and tested. Simulation results from these four configurations can be seen in Figures 43-46. S7 and S2 were selected because they were the best performing configurations. S6 was selected because all the cavities are of equal length in that configuration. S5 was selected because it was able to reach the lowest frequency out of all of configurations considered.

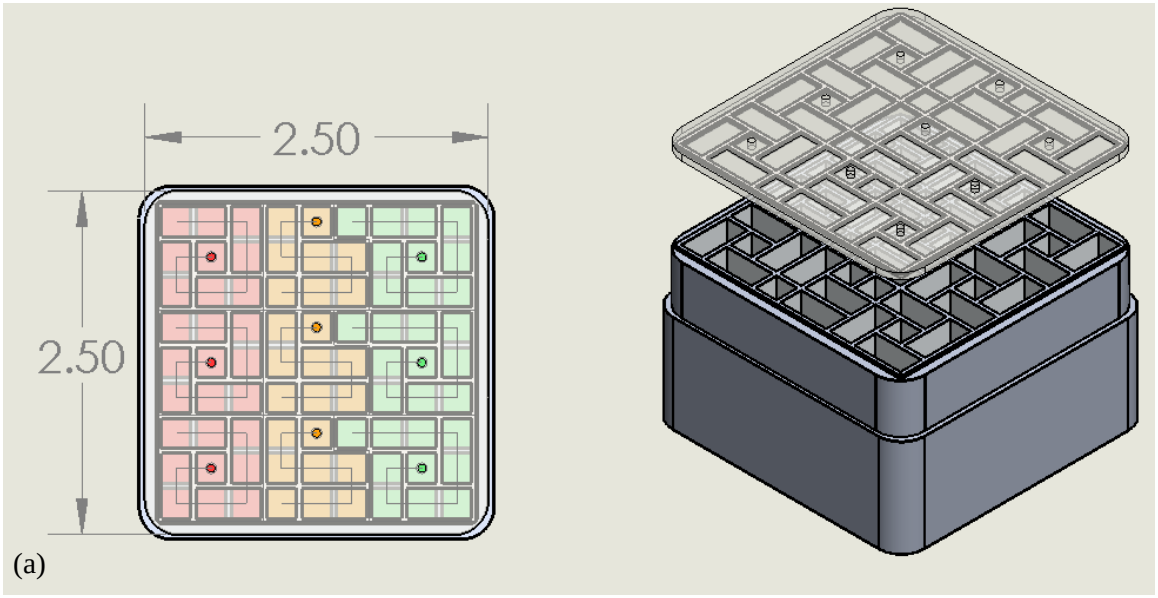

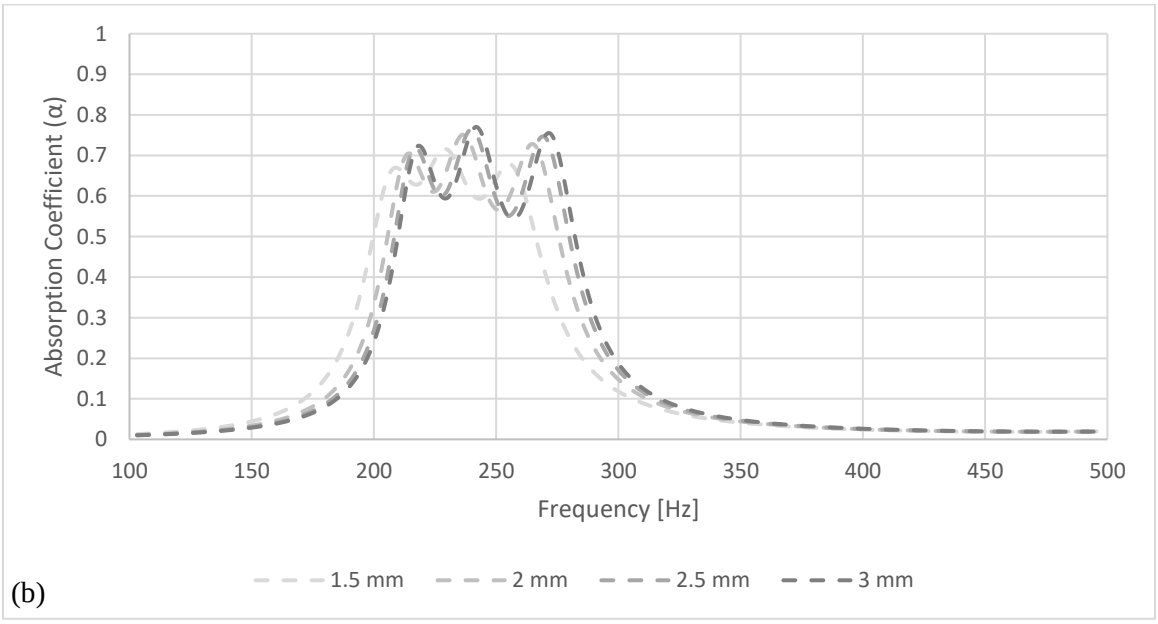

Figure 43: (a) S7 configuration and (b) ZKTL results for varying face sheet hole diameters. (Δf =2 Hz)

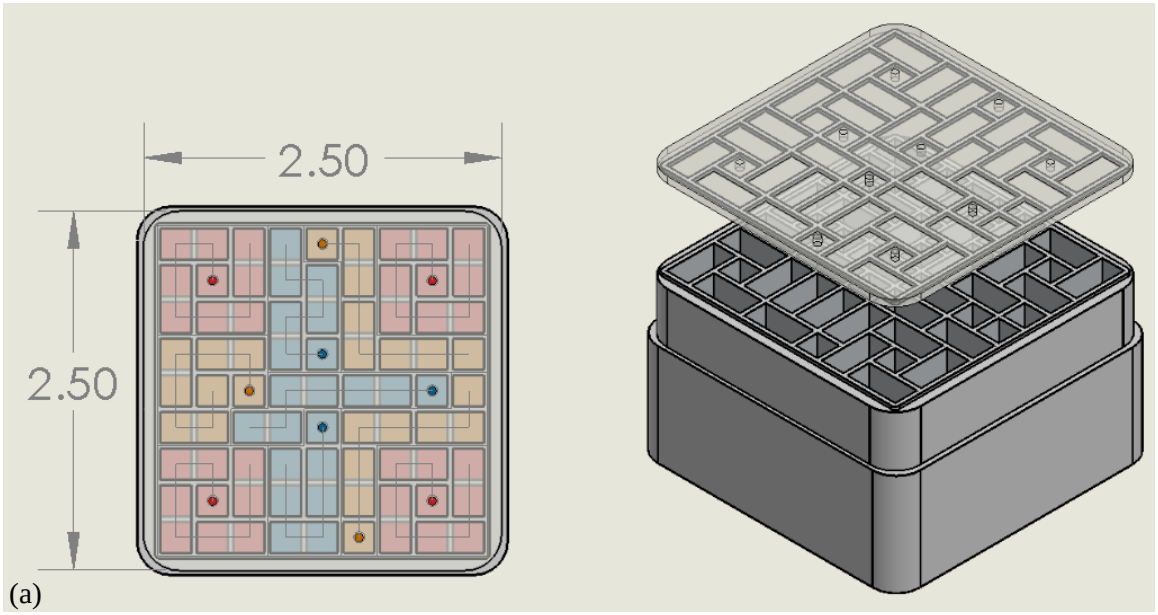

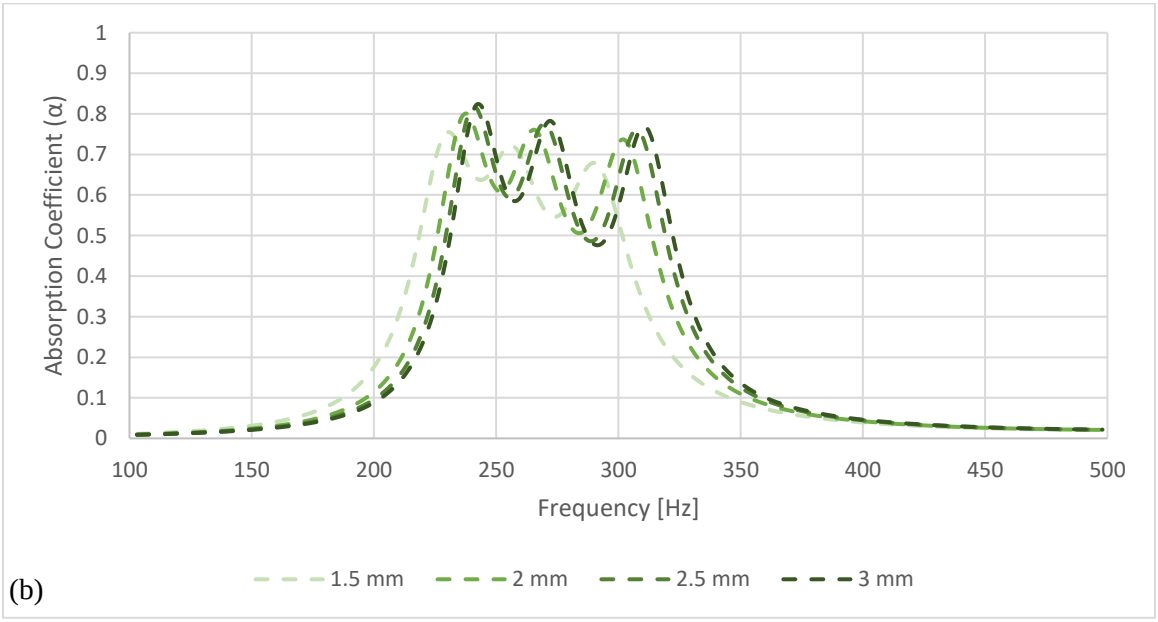

Figure 44: (a) S2 configuration and (b) ZKTL results for varying face sheet hole diameters. (Δf =2 Hz)

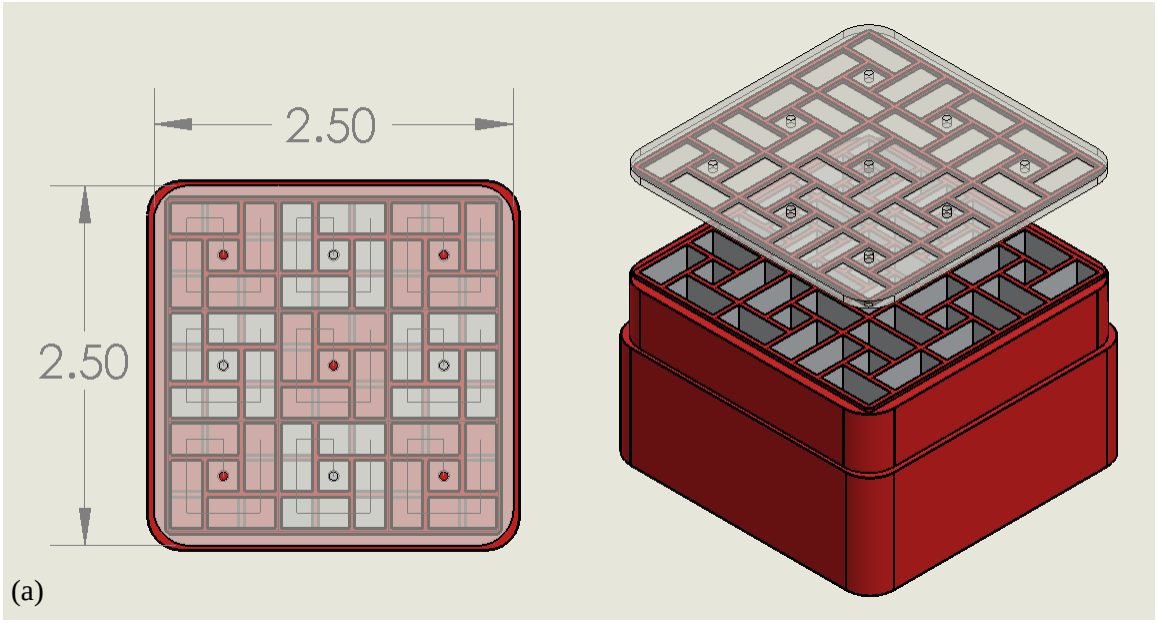

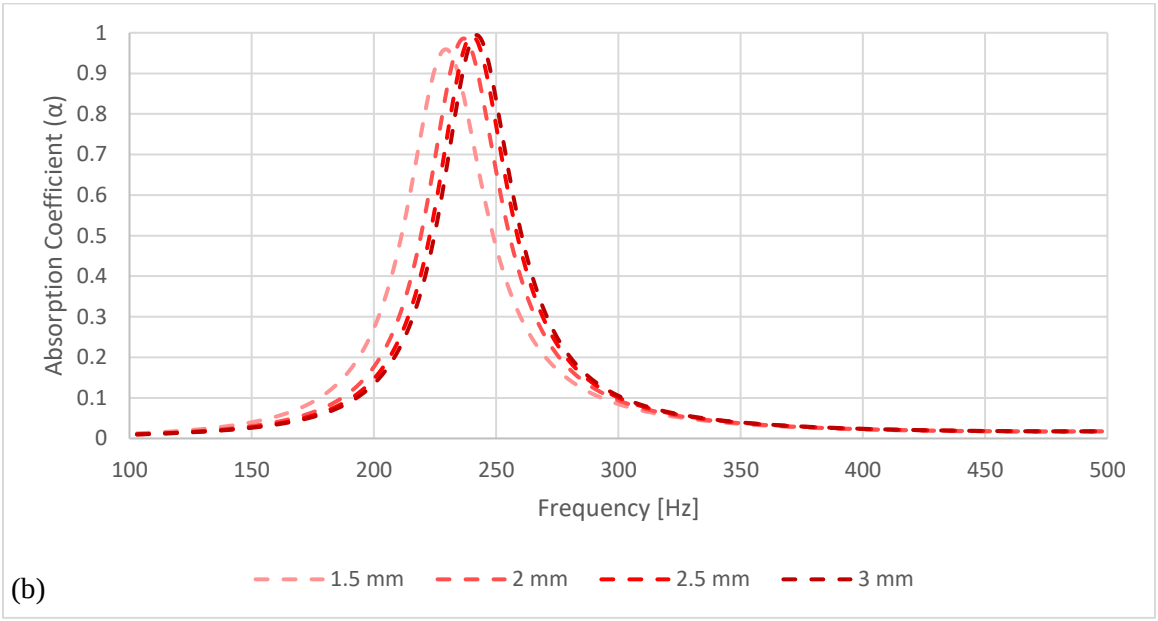

Figure 45: (a) S6 configuration and (b) ZKTL results for varying face sheet hole diameters. (Δf =2 Hz)

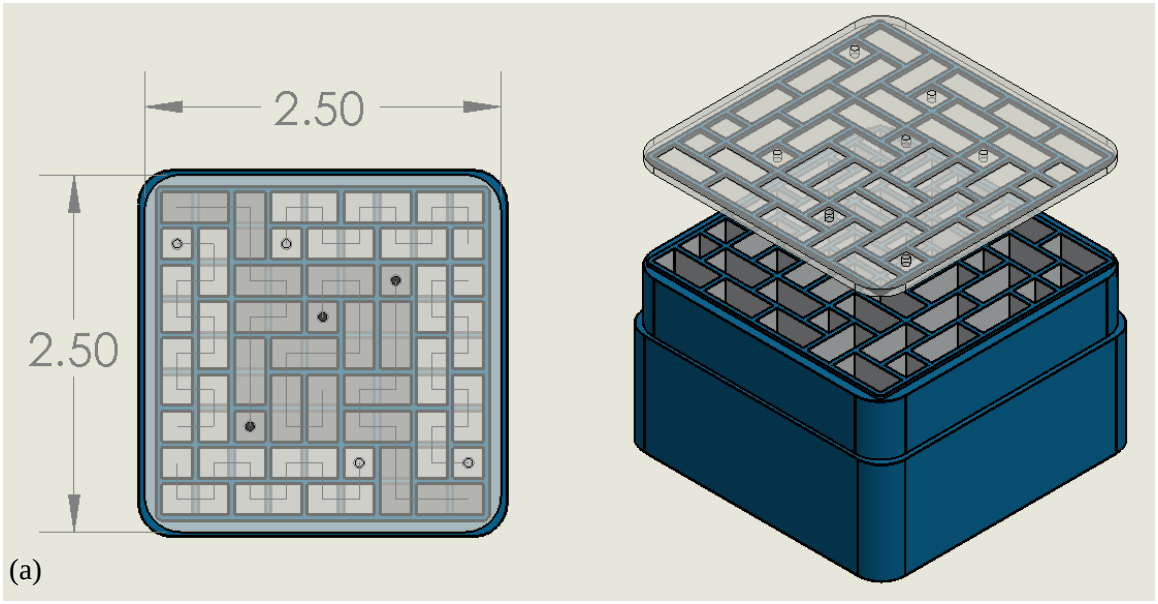

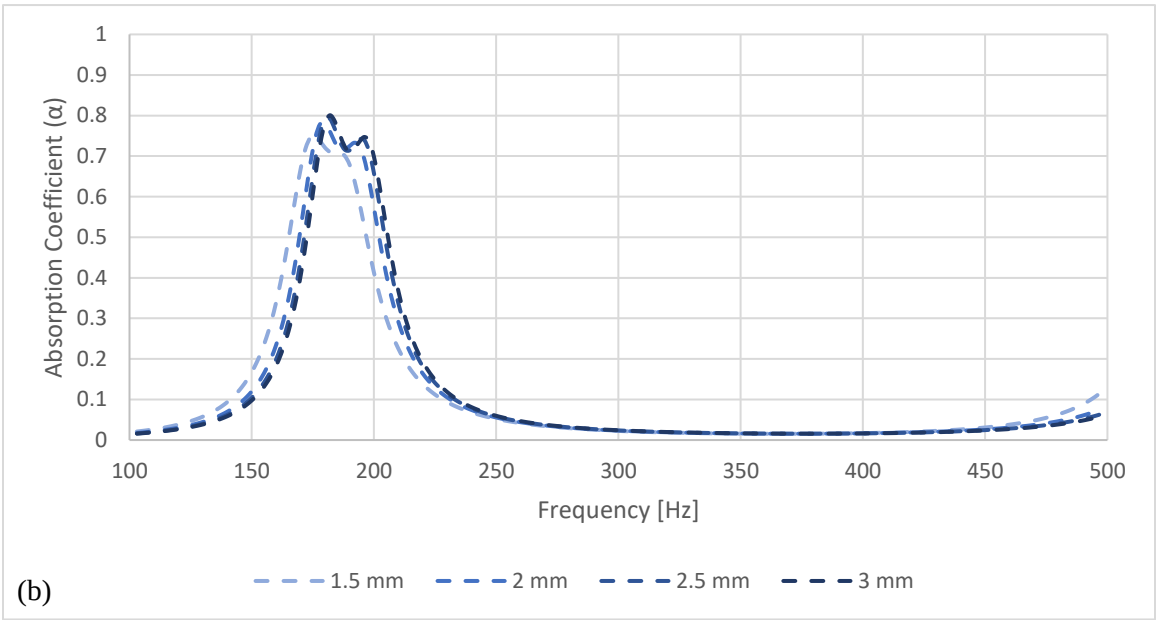

Figure 46: (a) S5 configuration and (b) ZKTL results for varying face sheet hole diameters. (Δf =2 Hz)

ZKTL simulation results show absorption below 500 Hz for each of the configurations. The single tone configuration (S6) has the highest absorption coefficient magnitude, while the other

three designs have a wider absorption bandwidth. Figures 43-46 also show that for each of the configurations, as the face sheet hole size increases, the absorption spectra shifts to higher frequencies. The frequency shift is slight between the different face sheets for each of the configurations, therefore the LFP doesn't change much based on the face sheet used.

2.5.14 Optimized 3D Folded Cavity Design

Questions regarding the acoustic rigidity of the internal walls in the sintered test articles led to the development of an Optimized 3D Folded Cavity design. The wall thickness was increased to 1.5 mm to ensure the acoustic rigidity of the walls. This liner was designed so that it could be tested in both the Oklahoma State University normal incidence impedance tube and the NASA normal incidence impedance tube. The details of both are provided in Chapter 3. The main difference between the two is that the active area of the liner (the surface area at the face of the liner that the sound wave will encounter) is a 2 inch x 2 inch square in the NASA tube as opposed to the 2.5 inch x 2.5 inch area in the OSU tube. Thus, the Optimized 3D Folded Cavity design was made with a 2 inch x 2 inch active area as shown in Figure 47. This decrease in active area from the previous folded cavity designs, along with an increased wall thickness, led to the final cavity size and number of cavities featured in this design. In order to test the exact same test article in the OSU tube, a simple adaptor sleeve was 3D printed and utilized. One of the things that make this design unique is that the cavity lengths are optimized so that the spacing between peaks in the absorption coefficient spectrum results in the best LFP. Instead of each cluster having an integer number of cells, some of cavity lengths are varied from a central length. In this design, the central length corresponding to the central peak in the absorption coefficient spectrum is the full length of 6 connected cells. In other words, instead of having [5(2) 6(2) 7(2)] configuration, this design

has a [5^{+}(2,) 6(2), 7^{-}(2)] configuration. The optimum cavity lengths were obtained using the 3D Folded Cavity Packing Optimization process shown in Figure 27. Retaining a consistent face sheet thickness of 1/16 inch, the optimum hole diameter was obtained using simulation to be 2 mm, and this face sheet was printed and tested along with this design. It was attached using double sided tape. Dimensions of the liner as well as the three distinct cavity lengths can be seen in Figure 47.

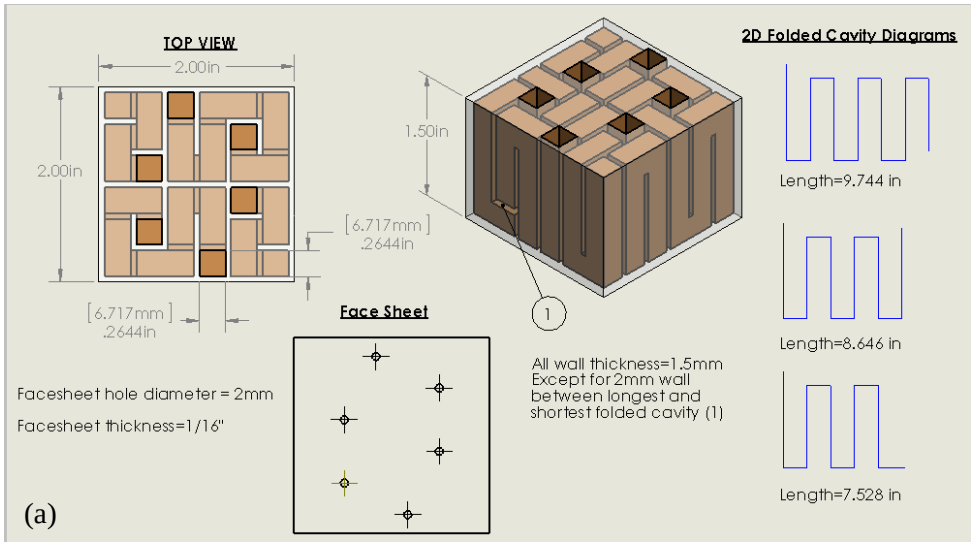

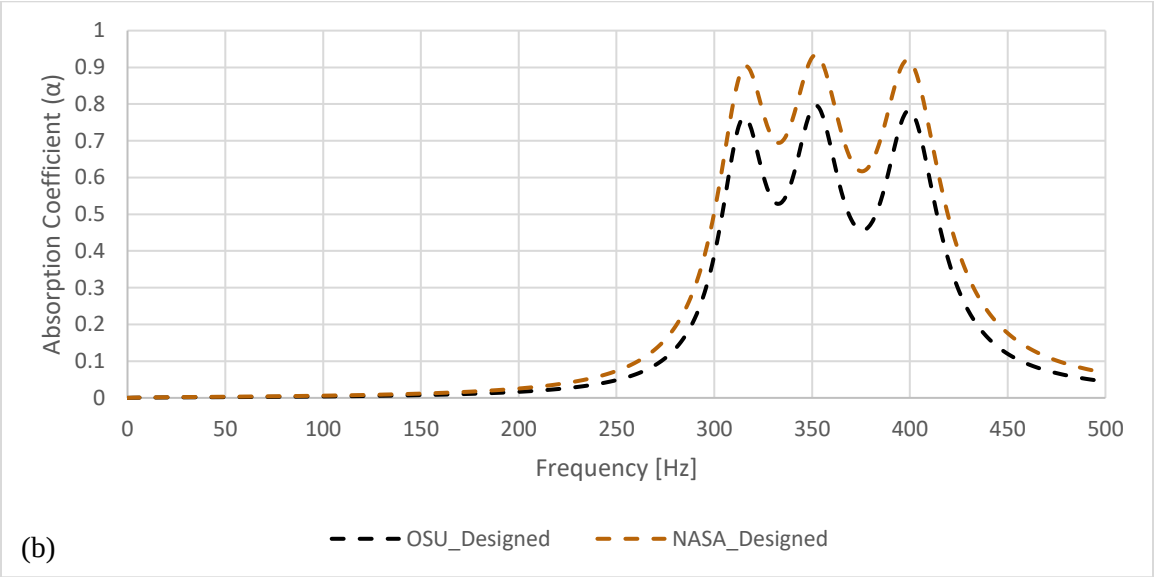

Figure 47: (a) Optimized 3D Folded Cavity design and (b) ZKTL simulation results. (Δf =2 Hz)

As shown in Figure 47, when the active area changes from 2 inch x 2 inch (NASA) to 2.5 inch x 2.5 inch (OSU), a drop in magnitude in the absorption coefficient spectrum is expected without any shift in frequency. This reduction in performance is not a limitation in itself, but is factored in to accommodate cross-compatibility between impedance tubes. Another important phenomenon observed during development of this design is that the spacing of resonant target frequencies for each cavity needed to achieve good broadband absorption is dependent on the frequency. For low frequencies, the cavity lengths need to be spaced closer together in order to keep the overall absorption spectrum above the threshold. If they become spaced too far apart, dips in the absorption spectrum disrupt the desired continuous bandwidth. On the other hand, for higher frequencies, the cavity lengths can be spaced further apart without disruption of continuous bandwidth.

2.6 Parametric Studies on Liner Porosity

During the design process, several phenomenon of interest were discovered that warranted further investigation. The first of which was the potential relationship observed between the peak absorption coefficient and the porosity for the different straight cavity baseline designs. Each of the three designs that were made with a corresponding straight cavity baseline design (L-Liner, U-Liner, and W-Liner) along with the Quarter Wave Baseline liner have different cavity sizes but the same number of cavities and the same overall area. Thus, they all have different porosities. Figure 48 shows the four quarter wave baseline design simulation results.

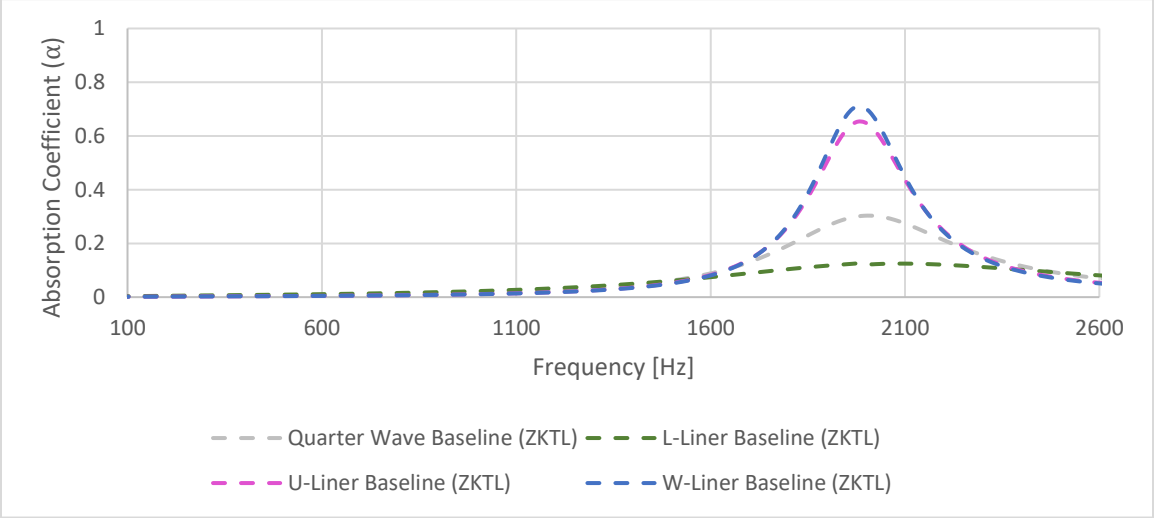

Figure 48: Straight cavity baseline simulation comparison. (Δf =2 Hz)

Figure 48 shows that each of the designs has a different peak absorption value. Figure 49 shows how the peak absorption coefficient changes for different porosities for these four liners. Note that the Quarter Wave Baseline, U-Liner, and W-Liner have the same number of square cavities (25) but varying cavity diameters. Thus, different amount of resistance is produced by scrubbing

losses within the cavities. The L-Liner has 30 cavities with 25 square cavities and 5 rectangular cavities.

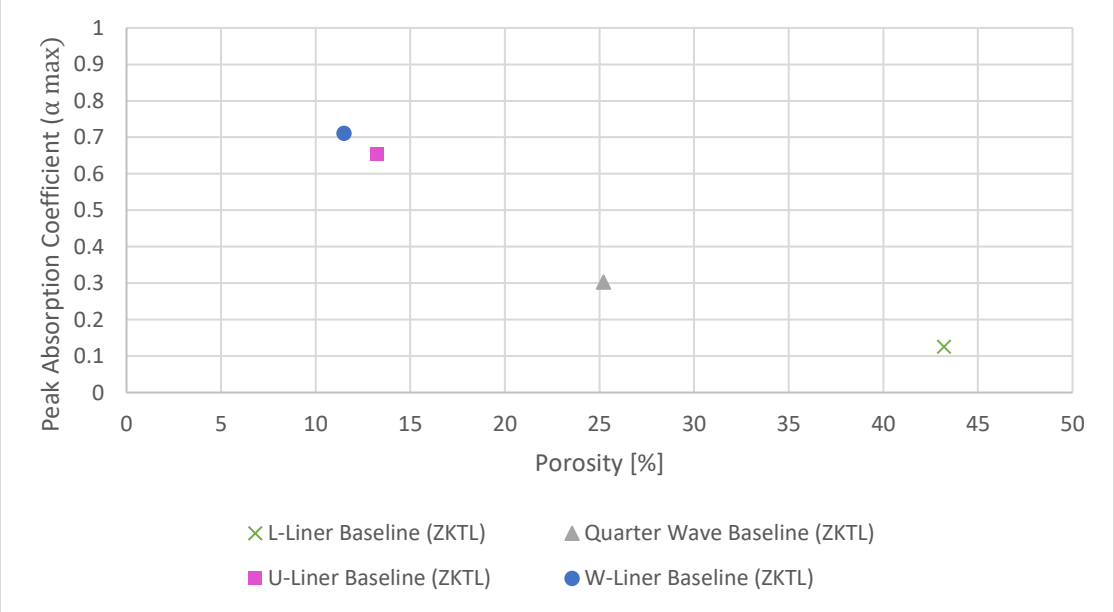

Figure 49: Peak absorption coefficient vs. porosity for the four quarter wave baseline designs.

In order to better understand this relationship, two parametric numerical studies were conducted. The first uses essentially a straight cavity baseline design for the Optimized 3D Folded Cavity design shown in Figure 47. The liner active area is 2 inches x 2 inches. There are 36 cavities, each with a total length of 1.44 inches (1.5 inch thickness – 1.5 mm back plate thickness). The number of cavities and the cavity length remains fixed, and the cavity diameter is varied from 6 mm to 1 mm in increments of 0.5 mm using the ZKTL simulation code. Figure 50 shows the absorption coefficient spectrum resulting from each of these iterations.

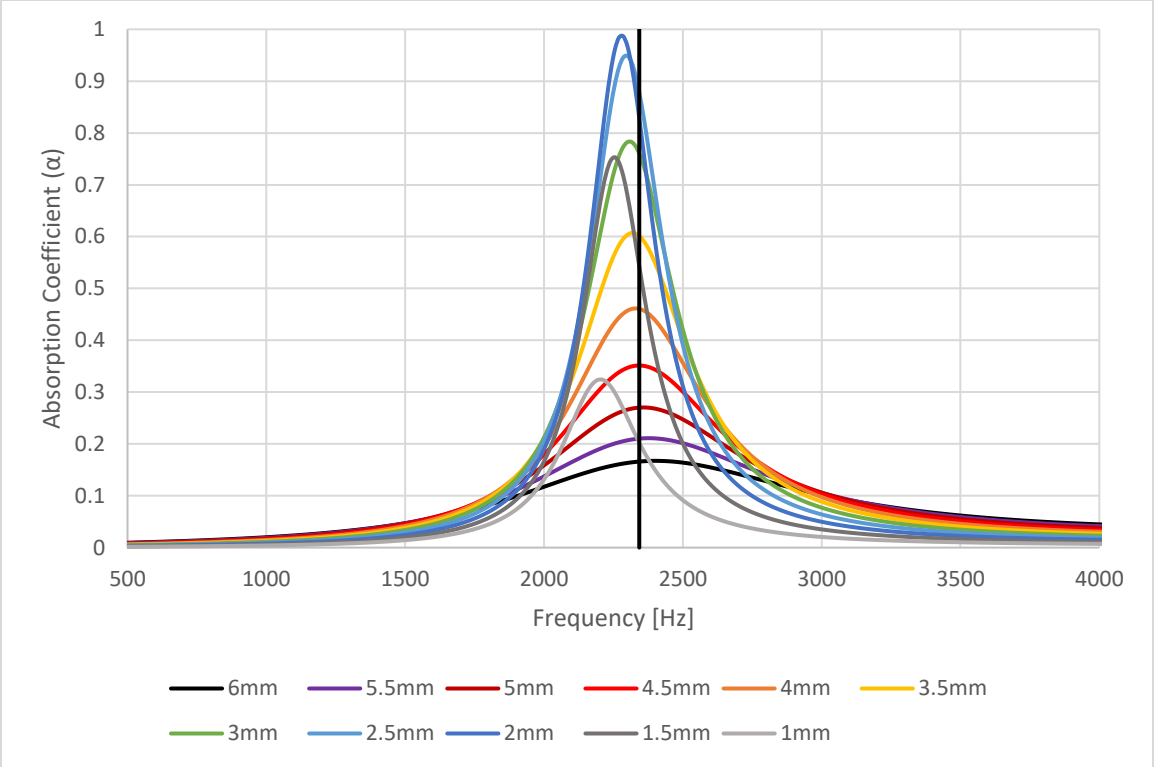

Figure 50: Simulation results for the parametric study where cavity diameter is varied. (Δf =2 Hz)

As seen from Figure 50, the peak absorption value changes as the cavity size changes, with a maximum peak being reached with a cavity diameter of 2 mm. Another important feature to note is that a shift in frequency for the peak location from the quarter wave frequency (2343 Hz, solid vertical line) begins to occur when the cavity diameter reaches approximately 3 mm. Figure 52 shows how the peak location is shifted for the different porosities examined. This shift increases as the cavity diameter or porosity decreases due to the increase in mass reactance. This could indicate that viscous effects become more and more present as the cavity size is decreased. As the cavity size becomes smaller, the viscous dissipation reduces the resonant response of the liner. This happens because acoustic dissipation in an air-filled channel is confined to the viscous

boundary layer induced by the no-slip boundary condition at the wall [24]. Figure 51 shows the peak absorption coefficient plotted against the porosity for each of the cases shown in Figure 50.

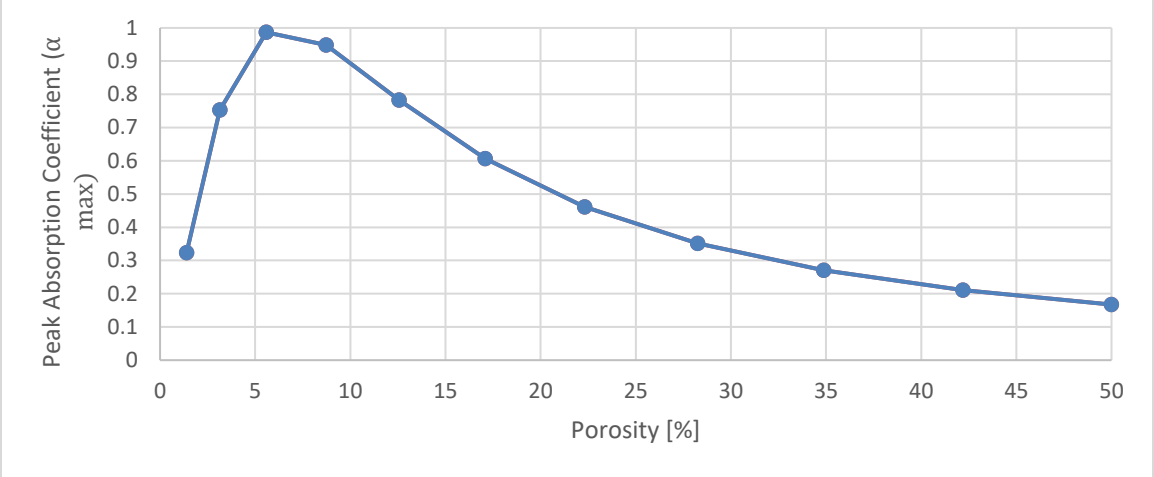

Figure 51: Peak absorption vs. porosity for the parametric study where cavity diameter is varied.

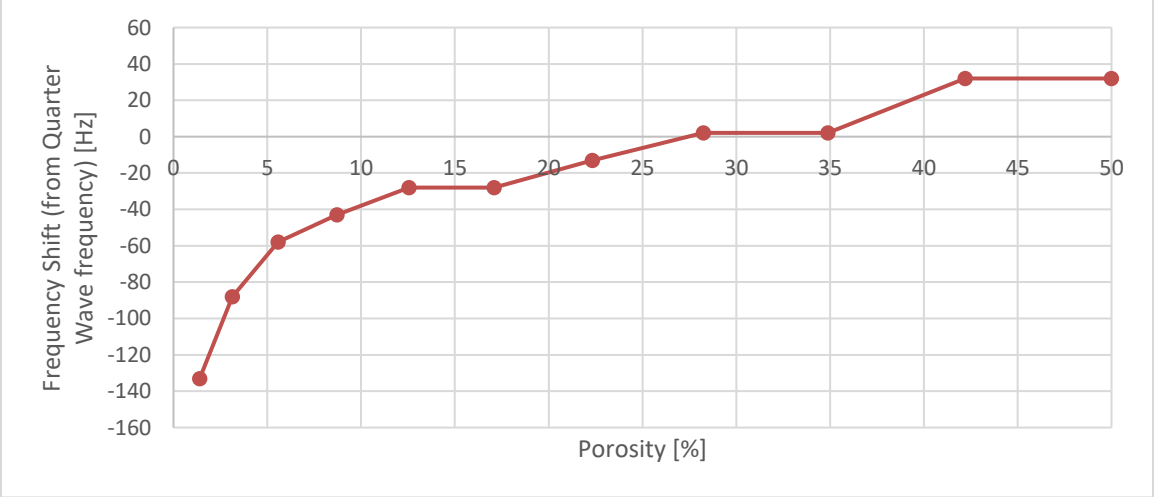

Figure 52: Shift in frequency from quarter wave designed frequency (2343 Hz) as the porosity changes for the parametric study where cavity diameter is varied.

Figure 51 shows that the ZKTL simulations indicate that an optimum peak absorption coefficient can be reached by choosing the porosity of the liner to be approximately 5%. This corresponds to

a 2 mm diameter cavity. But does that optimum porosity hold if the cavity size is fixed and the number of cavities is varied? In order to answer that question, another parametric experiment was developed that used the same liner (2 in x 2 in active area, 1.44 in cavity length) with a fixed cavity diameter. The number of cavities was then varied from 36 to 3 in 3 cavity increments. Three separate experiments were conducted using three different cavity diameters (2 mm, 3 mm, and 4 mm).

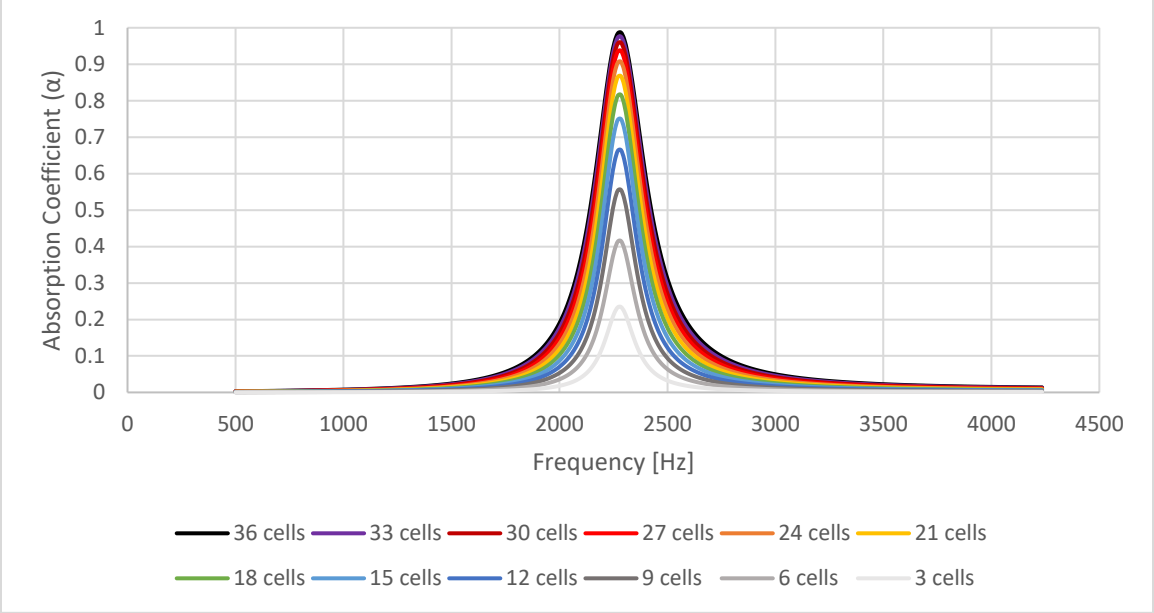

Figure 53: Simulation results for the parametric study where cavity length is varied, d_c = 2mm. (Δf =2 Hz)

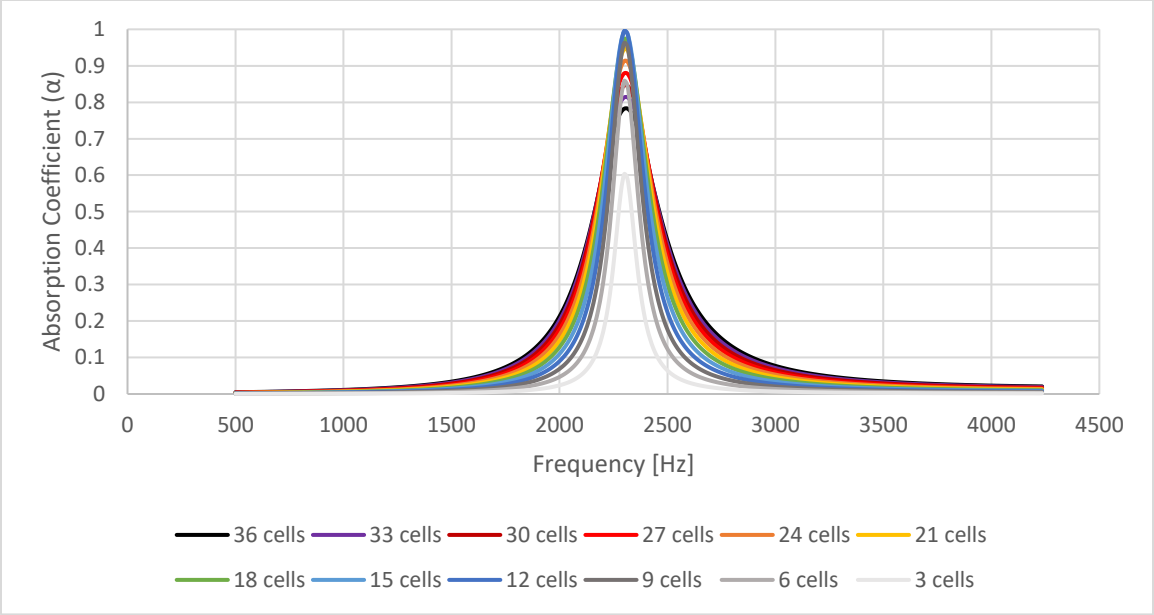

Figure 54: Simulation results for the parametric study where cavity length is varied, d_c = 3mm. (Δf =2 Hz)

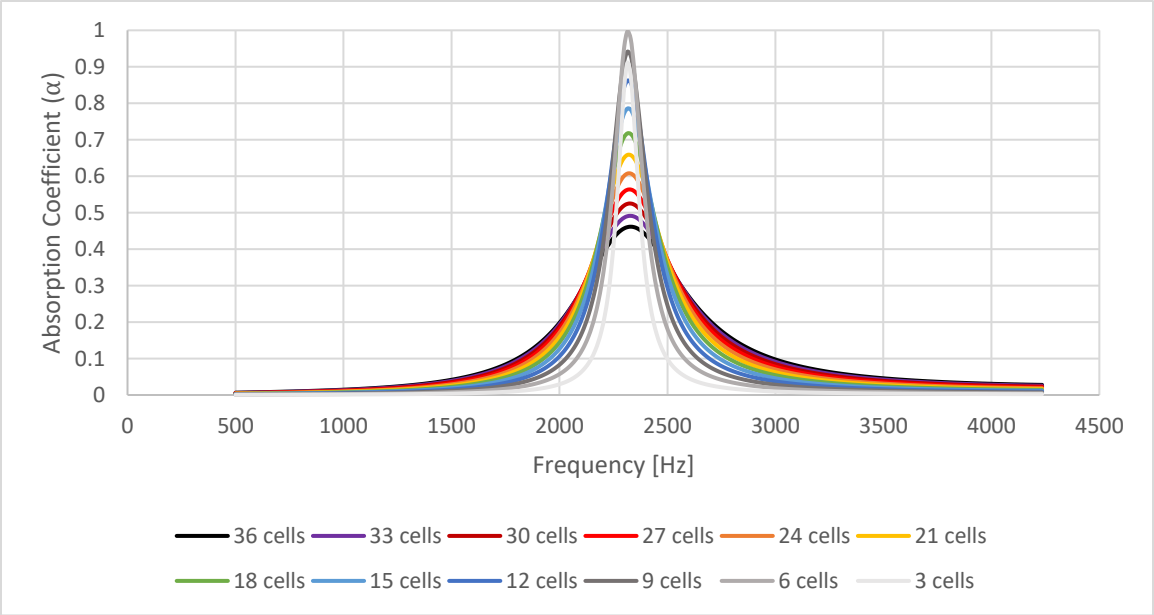

Figure 55: Simulation results for the parametric study where cavity length is varied, d_c = 4mm. (Δf =2 Hz)

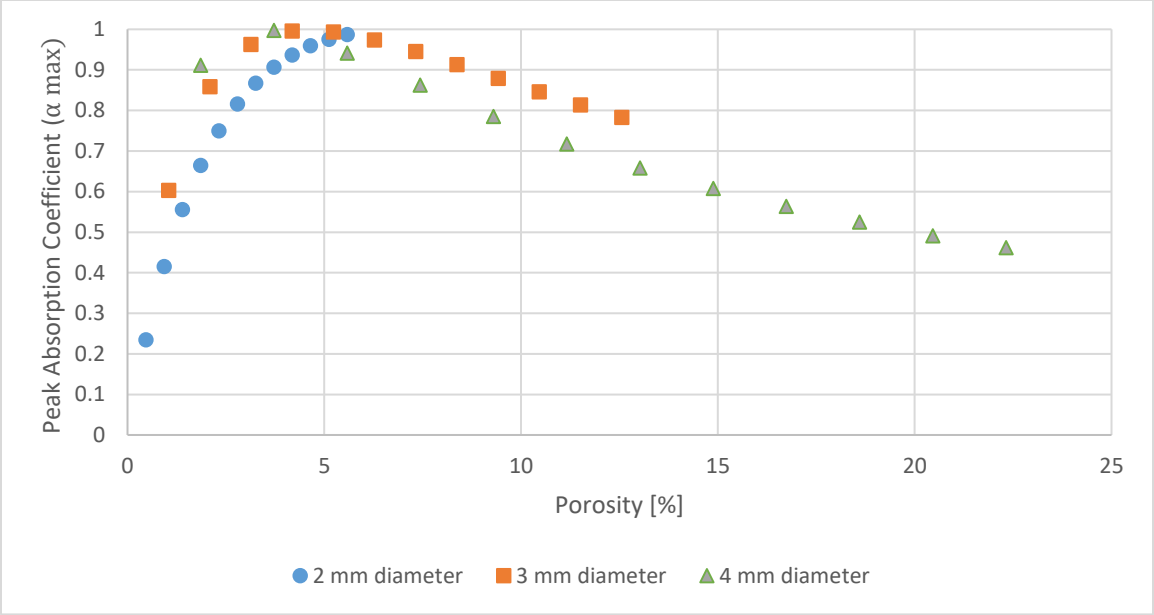

Figure 56: Peak absorption coefficient vs. porosity for each of the 3 parametric studies where cavity length is varied.

Figures 53-55 show that when the cavity size is unchanged, there is no frequency shift introduced with changing the number of cavities because the viscous dissipation of the cavities doesn't change. Figure 56 shows that for each of the fixed cavity diameter cases, the best porosity for achieving a high absorption coefficient peak is also at approximately 5%. As the porosity increases above 5%, the absorption peak begins to drop because in order for destructive interference to occur, reflections from the liner face must also be present. As the porosity increases, the available area for reflections from the liner face decreases. It is important to note that this 5% optimum porosity is for purely quarter wave resonating chambers in no-flow conditions. Ascertaining optimum porosity for Helmholtz resonating chambers with no flow, and any liner type with flow would require additional studies.

2.7 Chapter Summary

Chapter 2 provides a review of analytical terminology and methods associated with the Helmholtz and quarter wave absorption mechanisms, along with a detailed description of the ZKTL theory and numerical model used to predict liner performance and optimize liner configurations. A detailed description of the development and use of the Low-frequency Performance (LFP) factor in correlation with the Folded Cavity Packing Optimization Code is given. An in-depth description of each of the liner designs, along with ZKTL simulation results of those designs, was presented in Chapter 2. Lastly, a parametric study to examine the effect of porosity on liner performance is discussed.

CHAPTER 3

EXPERIMENTAL METHODS

3.1 Experimental Setup and Methodology

Three different experimental testing rigs and two testing methods were to evaluate the prototype liner test articles. The first and most predominantly used is the normal incidence impedance tube (NIT) located in the Oklahoma State University Acoustics Laboratory. The second is another normal incidence impedance tube located in the Liner Technology Facility at the NASA Langley Research Center. Both of these rigs were used to obtain the normal incidence absorption coefficient spectra. The last testing rig used is a grazing flow impedance tube, which is also located in the Liner Technology Facility at NASA Langley. Experimental NIT results from all designs tested are compared to their respective predicted ZKTL simulation results. All designs are tested in the OSU impedance tube (except for the GFIT test article), while the Optimized design is the only test article tested at the NASA facility.

3.1.1 Oklahoma State Normal Incidence Tube

The normal incidence impedance tube at Oklahoma State is located in the OSU Acoustics Laboratory [35]. The tube was designed to be used for both transmission loss and absorption testing. Figure 57 shows an exploded view of the entire setup, including the transmission loss side.

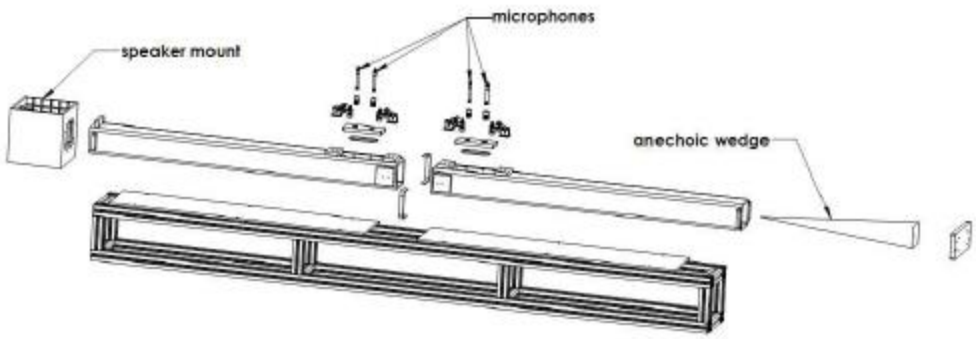

Figure 57: Exploded view of the OSU transmission loss tube. [35]

The transition from the transmission loss testing setup to the absorption testing setup is accomplished by placing the test article inside a separate sample holder that bolts into flanges located on the side of the incident tube. The holder has an adjustable steel back plate to accommodate different thickness test articles (Figure 58 (b)). The holder is acoustically sealed to the incident tube with petroleum jelly for each test. The transmission side tube is irrelevant for the absorption testing. The holder has a slightly larger area internal than the incident tube however. This area mismatch is compensated for with each of the test articles so that the each one is properly aligned with the tube.

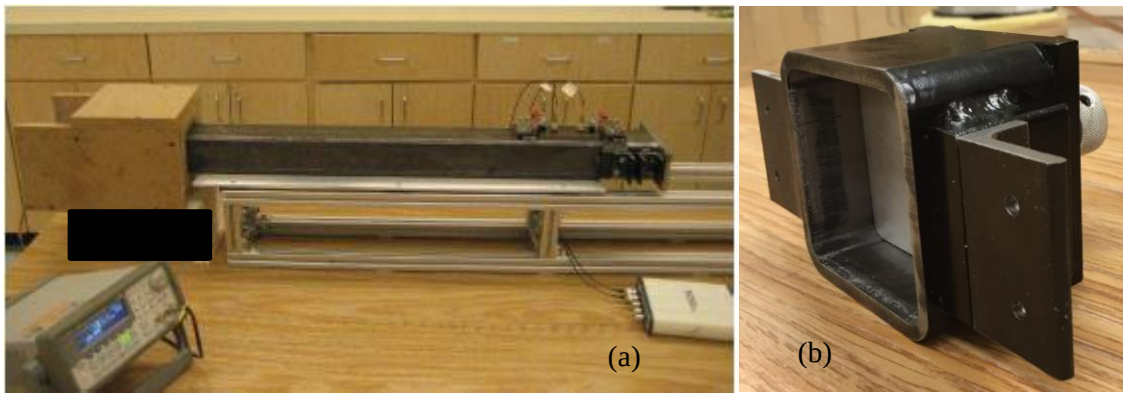

Figure 58: (a) Impedance tube setup for absorption testing. (b) Adjustable sample holder.

Calculations to compute acoustic performance follow the two-microphone method and agree with both ASTM E1050 [36] and ISO 10534-2:1998 [37]. The absorption coefficient spectrum is calculated from the following set of equations, beginning with the free-space wave number k.

$$k = \frac{2\pi f}{c} \tag{21}$$

Next, the real and imaginary components of the complex frequency response functions (FRF) measured from each microphone are put into their complex form.

$$H_{11} = H_{1r} + iH_{1i} \tag{22}$$

$$H_{22} = H_{2r} + iH_{2i}\,. \tag{23}$$

Then the reflection coefficient RC is calculated.

$$RC = \frac{H_{22} - e^{-i(2)(k)}}{e^{i(2)(k)} - H_{22}} e^{i(2)(k)(2+g)} \tag{24}$$

Where 2 is the distance between the two microphones in inches, and g is the distance from the liner face to the closest microphone. Finally, the absorption coefficient α can be calculated.

$$\alpha = 1 - |RC|^2 \tag{25}$$

Additionally, the impedance z can be found using the reflection coefficient.

$$z = \rho c \frac{1 + RC}{1 - RC} \tag{26}$$

In this experimental setup, the tube length is 36 inches, with a 2.5 inch x 2.5 inch (with 0.25 inch corner fillets) open cross sectional area. Two G.R.A.S ¼ -inch microphones are used to measure the sound pressure at 3.5 inches and 5.5 inches from the end of the tube respectively. Microphone calibration was performed at the beginning of the experimental process. The Overall Sound Pressure Level (OASPL) of the broadband white noise signal used in each experiment is

approximately 110 dB. The effective reliable frequency range is ~80 Hz to ~2500 Hz. The lower frequency limit depends on the spacing of the microphones and the accuracy of the analysis system, and the upper frequency limit depends on the diameter of the tube and the speed of sound. For each of the test articles tested in the OSU tube, three experimental runs are made and the data shown is an average of those three tests.

3.1.2 NASA Normal Incidence Tube

The OSU impedance tube is built similarly to The NASA Langley Normal Incidence Tube (NIT), with a few differences. The first major difference is that the interior cross sectional area of the NASA tube is a 2 inch x 2 inch square. When keeping the test articles active area the same, this difference in area has an effect on the magnitude of the absorption coefficient spectrum, as seen in the simulation results for the Optimized design shown in Figure 56. The second major difference is that the OSU tube's source is set at a 110 dB SPL level, while the NASA tube's can go up to 140 dB for standard tests. The NASA tube also uses a two-microphone method to measure the impedances [38][39].

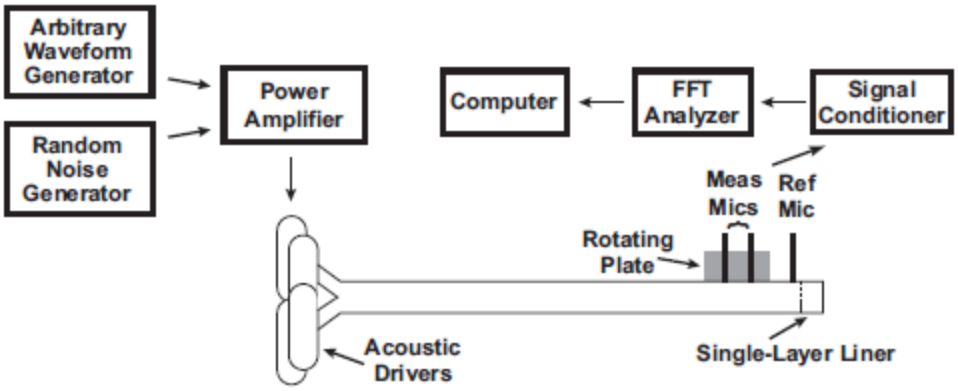

Figure 59: Sketch of the NASA Langley NIT shown with supporting instrumentation. [40]

3.1.3 NASA Grazing Flow Impedance Tube

The NASA Langley Grazing Flow Impedance Tube (GFIT) is a 6 m long, 2.5 inch x 2 inch waveguide that is used to measure acoustic liner performance within a controlled grazing flow environment [40]. Acoustic testing in the GFIT is conducted at near-ambient conditions with grazing flows up to Mach 0.5. For the tests conducted in this study, Mach 0.3 and Mach 0.5 flow was used. The standard SPL levels used in the GIFT are 120 dB and 140 dB, just like the NIT tube. Impedance of the samples is determined using the NASA Langley's impedance eduction technique [41], while the attenuation across the liner is directly calculated from the microphones.

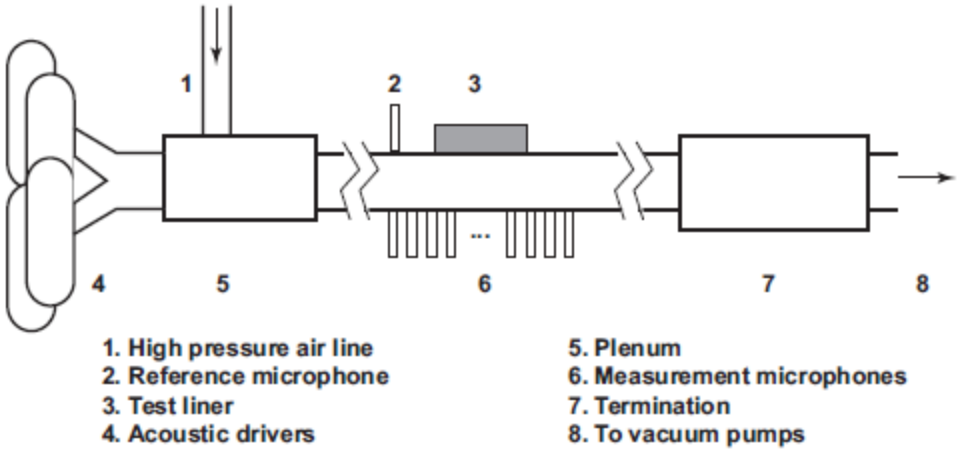

Figure 60: Sketch of the NASA Langley GFIT.

3.2 Test Article Fabrication

Two different fabrication techniques, conventional sandwich core composite layup and additive manufacturing, were used to manufacture the different test articles. The Helmholtz Baseline liner was the only article discussed in this thesis that was made using a 2 inch thick aluminum honeycomb core and 1/16th inch thick aluminum sheet metal. The aluminum sheet metal was used for the face sheet and back plate of the liner. Both the face sheet and back plate were cut to the OSU impedance tube dimensions, and then attached to the honeycomb core with Loctite Hysol epoxy. The face sheet was attached first, then the face sheet holes were drilled before the back plate was attached, so that no debris would be left inside the liner. The face sheet holes were drilled with a standard 1/16 inch diameter drill bit. Next, the back plate was attached, and the honeycomb core was trimmed so that the entire sample would fit properly inside the OSU impedance tube. Interfaces were sealed to prevent acoustic leakage.

The other fabrication method used is additive manufacturing. Several different types of 3D printers were used to manufacture the different test articles. The primary printer used for the majority of the test articles is an extrusion-type Makerbot Replicator 2X desktop 3D printer, which uses a fused filament fabrication process. The Quarter Wave Baseliner, L-Liner, U-Liner, Phased Slanted U-Liner, W-Liner, Circle Spiral, Square Spiral, Broadband Spiral Insert, and each of the secondary configurations (baselines and face sheets) for each of these test articles were manufactured with the Makerbot printer. ABS plastic was the extrusion material used for each of these test articles. For some, several layers of masking tape were added to the bottom inch of the test article to account for the area mismatch between the tube and the sample holder.

The Sintered designs were printed using a SLS (Selective Laser Sintering) 3D printing process by Shapeways©. The material needed to ensure a proper fit in both the sample holder and the tube was printed directly with the cores of these test articles, instead of using layers of tape. In the SLS printing process, the powder could easily get trapped inside any internal cavities. Because of this, and along with wanting to test different face sheets on each sample, the face sheets were printed separately from the core of each sample and designed to be detachable. Ridges that follow the internal wall structure were cut into the face sheets along with corresponding extrusions on the core so that the face sheets fit onto the core using an interlocking grid. By doing so, the face sheet holes were able to align perfectly, and no powder remained trapped inside the cavities. To keep the face sheets secured to the core, masking tape was used along the outer edge of the test article. The Optimized 3D Folded Cavity GFIT article was also printed using the Makerbot Replicator 2X. It was printed in eight different interlocking sections (four holder sections and four test article sections) to form the total 22 inch long test article.

The final two 3D printers were each used to print a single NIT Optimized 3D Folded Cavity test article. An extrusion-type Prusa i3 3D desktop printer was used with ABS plastic as the material to create the PR_Yellow test article. Lastly, an unspecified Shapeways© extrusion-type printer was used with PLA material to create the SW_Grey test article. Both of these printers follow the fused filament fabrication process.

3.3 Discussion of Results

Results for each of the test articles tested are shown and discussed in detail in this section. The absorption coefficient spectrum is shown for each of the experimental tests for each of the different configurations for each of the different designs, along with the appropriate ZKTL simulation results. Photographs of each of the completed test articles are also included in this section.

3.3.1 Quarter Wave Baseline Results

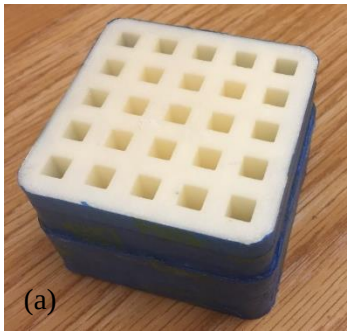
(a)

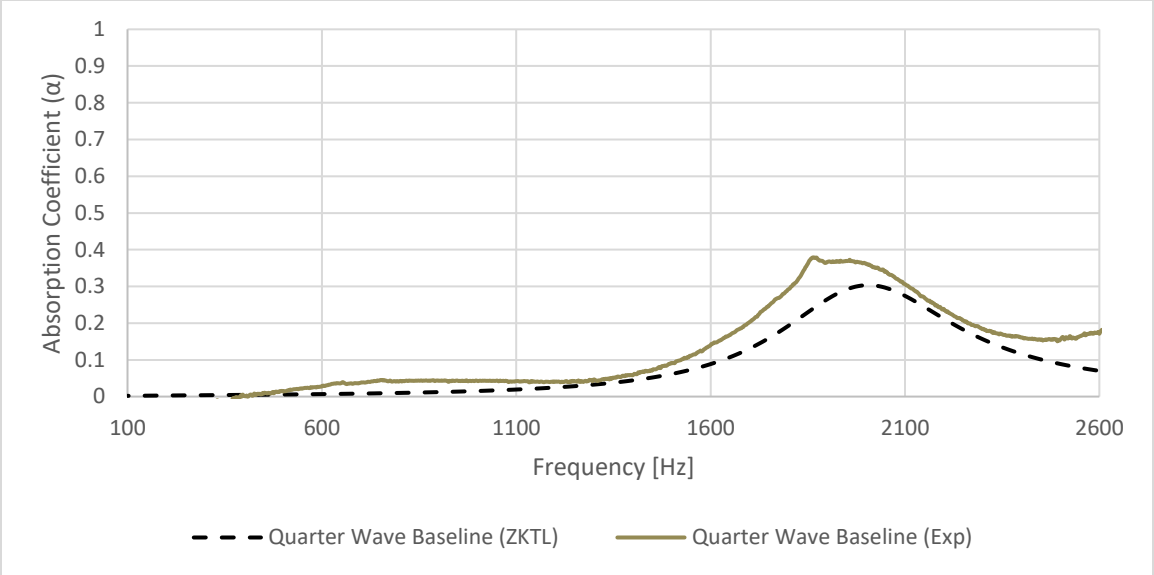

(b)

Figure 61: (a) Quarter Wave Baseline test article and (b) absorption coefficient spectrum. (Δf =2 Hz)

As shown in Figure 61, the experimental absorption coefficient spectrum matches well with the expected ZKTL simulation results. The peak absorption frequency range for the conventional liner with straight cavities is limited by the liner volume that is available. Targeting lower frequencies using straight cavities requires the use of thicker liners. The slight difference in the experimental spectrum from the simulated spectrum is perhaps due to imperfect source and acoustic sealing conditions, and possible imperfect setup conditions in the experiments.

3.3.2 Helmholtz Baseline 1 Results

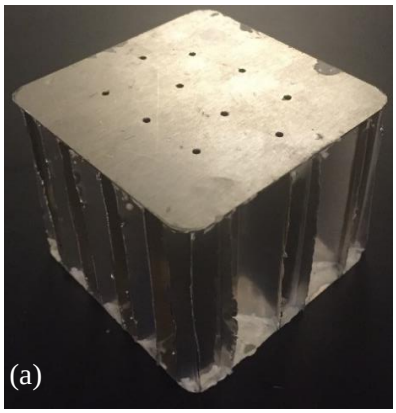

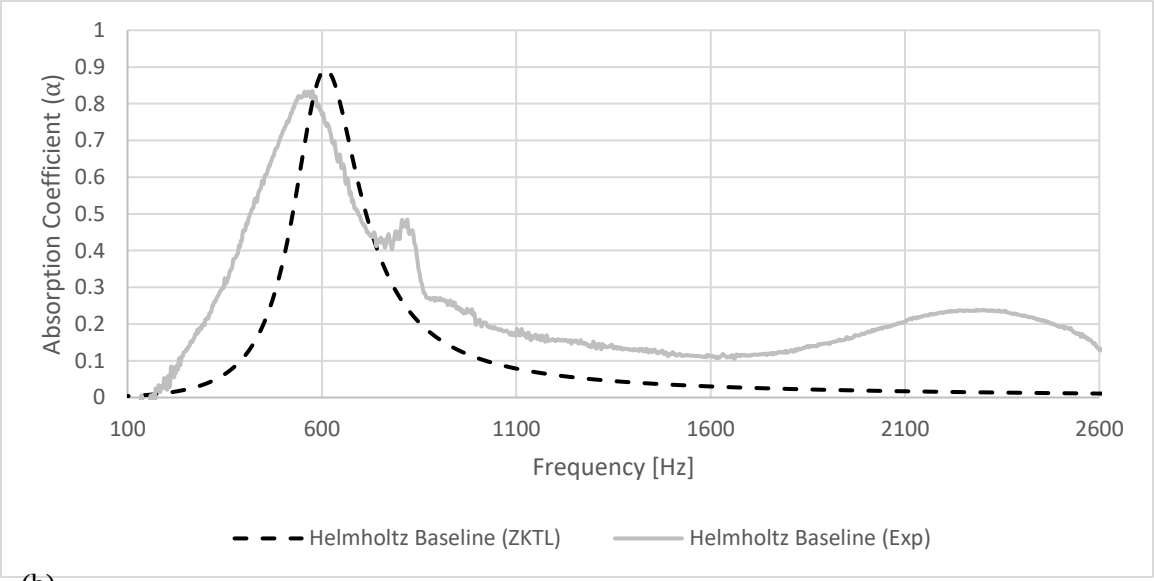

(b)

Figure 62: (a) Helmholtz Baseline test article and (b) absorption coefficient spectrum. (Δf =2 Hz)

Figure 62 shows that the ZKTL simulation predicted the absorption coefficient spectrum fairly well. The non-uniformity of the honeycomb cell could account for the slight discrepancy in the peak location and the width of the peak. The small secondary peak in the experimental results near 830 Hz is most likely due to a resonating chamber created by the outside of the honeycomb and the interior wall of the sample holder.

3.3.3 L-Liner Results

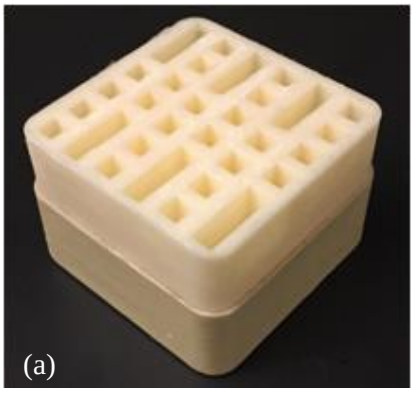

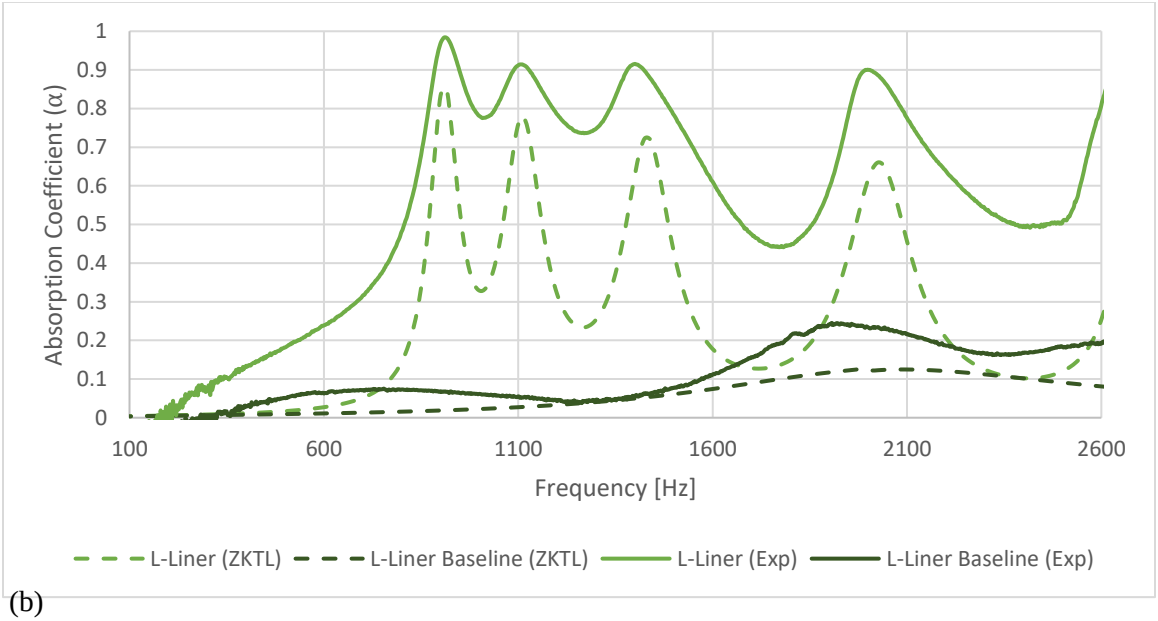

(b)

Figure 63: (a) L-Liner test article and (b) absorption coefficient spectrum. (Δf =2 Hz)

Figure 63 shows that by introducing folds to increase the cavity lengths, absorption at lower frequencies can be reached. By having multiple cavities at different lengths, the bandwidth of absorption is greatly increased from the straight cavity baseline design. Figure 63 also shown that the peak frequency location can be accurately predicted by the ZKTL code for broadband quarter wave resonator designs.

3.3.4 U-Liner Results

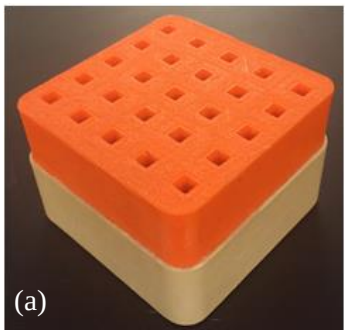

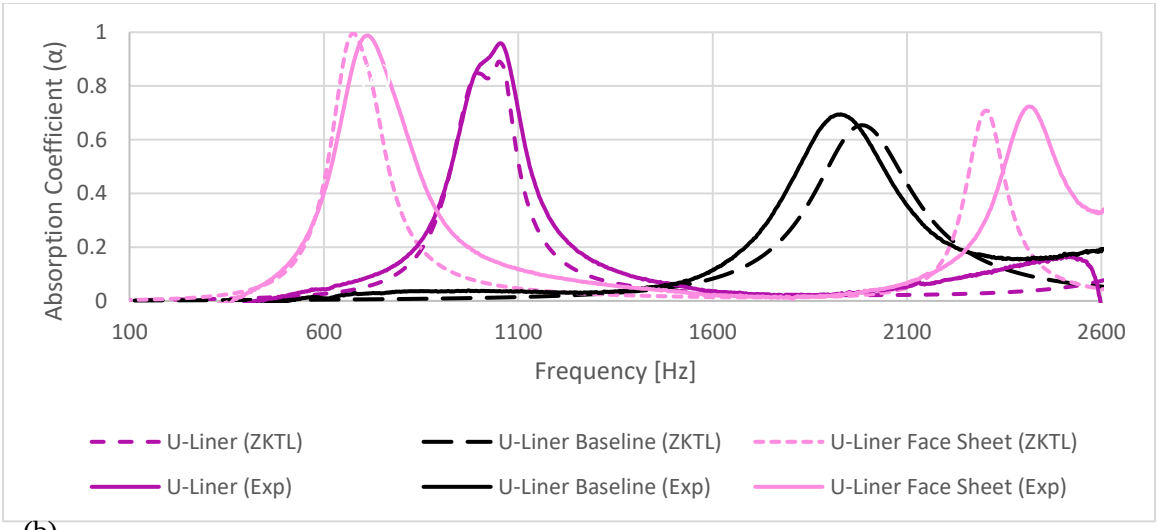

(b)

Figure 64: (a) U-Liner test article and (b) absorption coefficient spectrum. (Δf =2 Hz)

Figure 64 shows that good matching between experimental results and ZKTL simulation results occurs for all three different configurations of the U-Liner. The slight double peak predicted in the no-face sheet design can also be seen in the experimental absorption coefficient spectrum. Figure 64 also shows that increasing the cavity length by approximately twice the straight cavity length causes a shift to a much target lower frequency. Adding a face sheet to change the absorption mechanism of the liner from quarter wave resonance to Helmholtz resonance causes the peak to shift to an even lower frequency.

3.3.5 Phased Slanted U-Liner Results

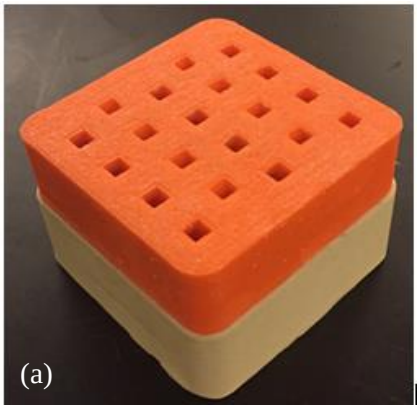

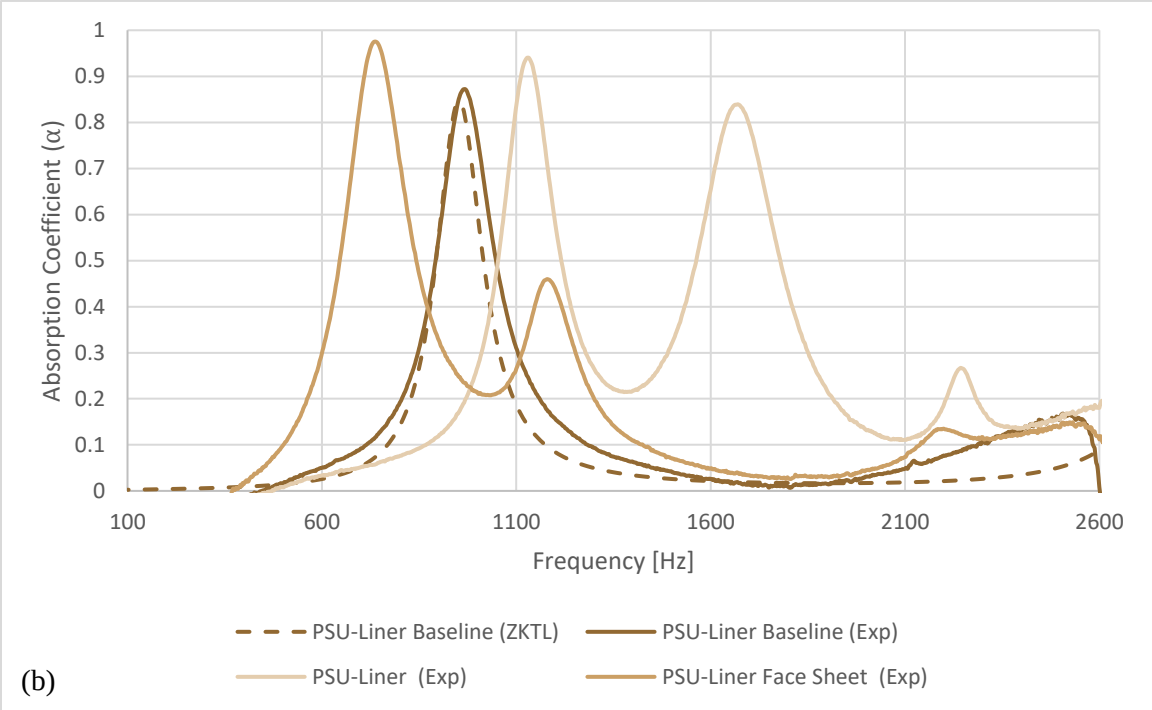

Figure 65: (a) Phased Slanted U-Liner (PSU) test article and (b) absorption coefficient spectrum. (Δf =2 Hz)

Figure 65 shows that for the locally reacting baseline case, the ZKTL simulation accurately predicts the absorption performance of the liner. Figure 65 also shows that when the cavities become connected and the liner becomes non-locally reacting, a dual peak phenomenon is

introduced in both the quarter wave (PSU-Liner) and the Helmholtz (PSU-Liner Baseline) absorption spectra. Interestingly, when no face sheet is added to the liner, the absorption shifts to a higher frequency from the baseline case. However, when a face sheet is added, the absorption shifts to a lower frequency from the baseline case. The mechanism behind non-local reacting liners needs to be further investigated to be able to accurately predict how it performs.

3.3.6 W-Liner Results

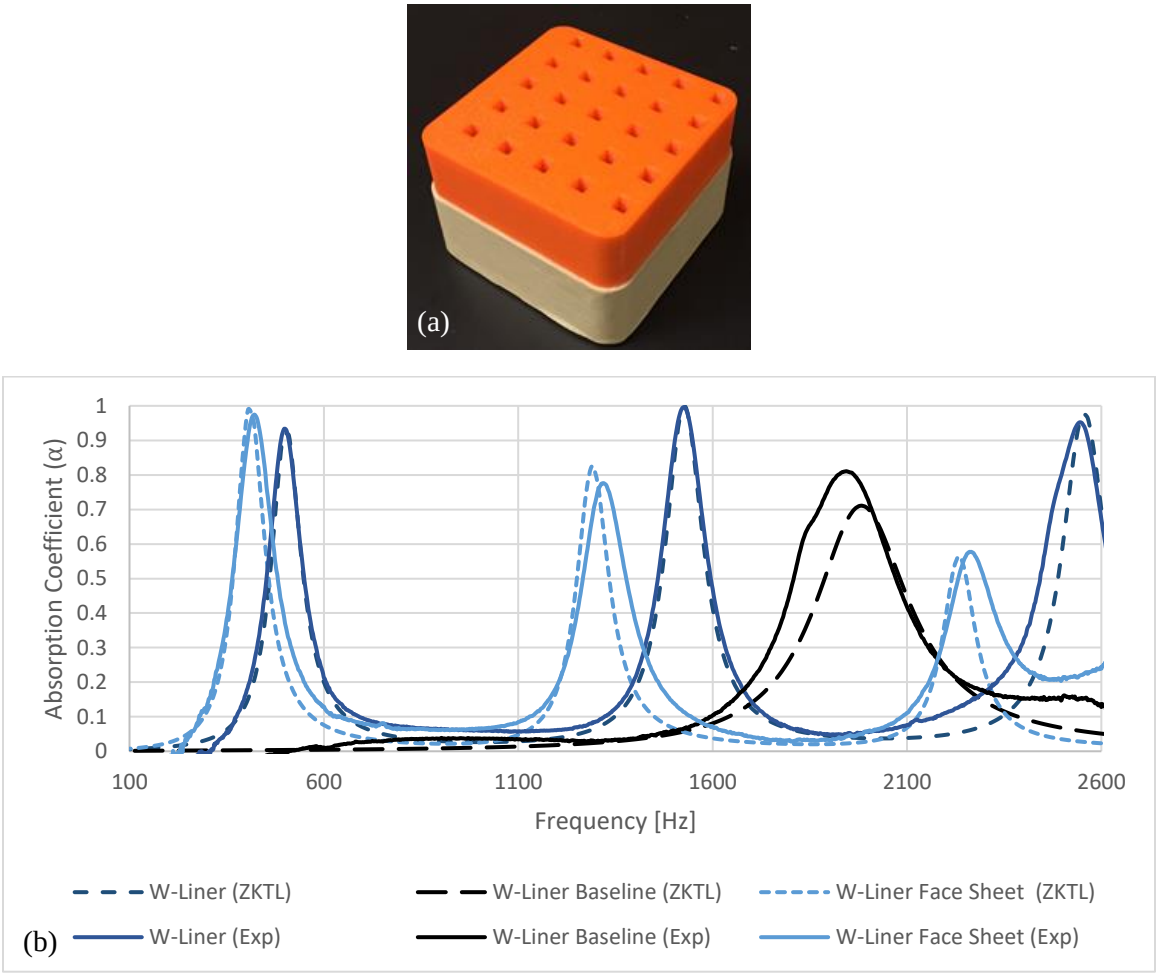

Figure 66: (a) W-Liner test article and (b) absorption coefficient spectrum. (Δf =2 Hz)

Figure 66 shows exceptional matching between the ZKTL prediction and the experimental results for each of the W-Liner configurations tested. Both the W-Liner and the W-Liner with face sheet configurations show significant movement toward lower frequencies from the straight cavity baseline configuration. This is the first design tested that shows substantial absorption at the higher harmonics corresponding to the odd multiples of the target frequency as explained in Section 2.1. The first peak for the Helmholtz configuration (with face sheet) is located at ~430 Hz, which is within the < 500 Hz target frequency range. The LFP for the W-Liner with face sheet as calculated using the experimental results per equation 17 is 24.35.

3.3.7 Circle Spiral Results

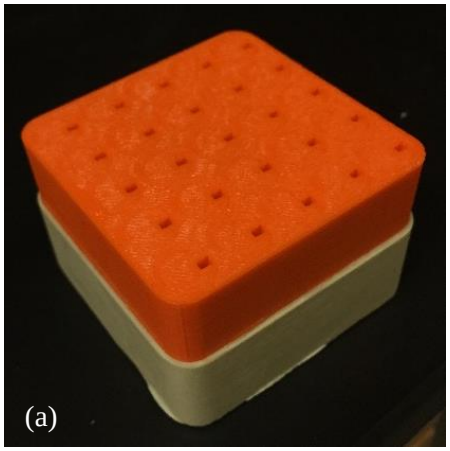

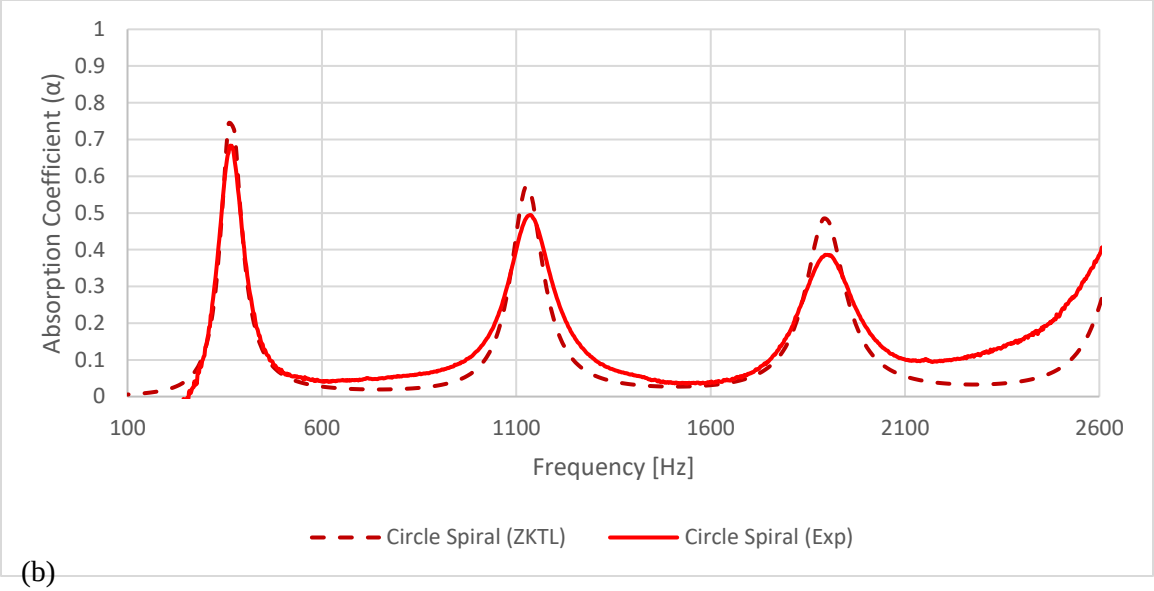

(b)

Figure 67: (a) Circle Spiral test article and (b) absorption coefficient spectrum. (Δf =2 Hz)

The peak locations from the experimental results match well with the ZKTL simulation results as shown in Figure 67, but the magnitude of the experimental absorption spectrum is slightly less for each of the peaks than predicted. This is likely due to inaccuracies involved with printing small holes using an extrusion-type printing method. Higher harmonic absorption can also be seen from Figure 67. The first peak location is < 500 Hz, therefore a LFP of 5.82 can be calculated from the experimental absorption coefficient spectrum.

3.3.8 Square Spiral Results

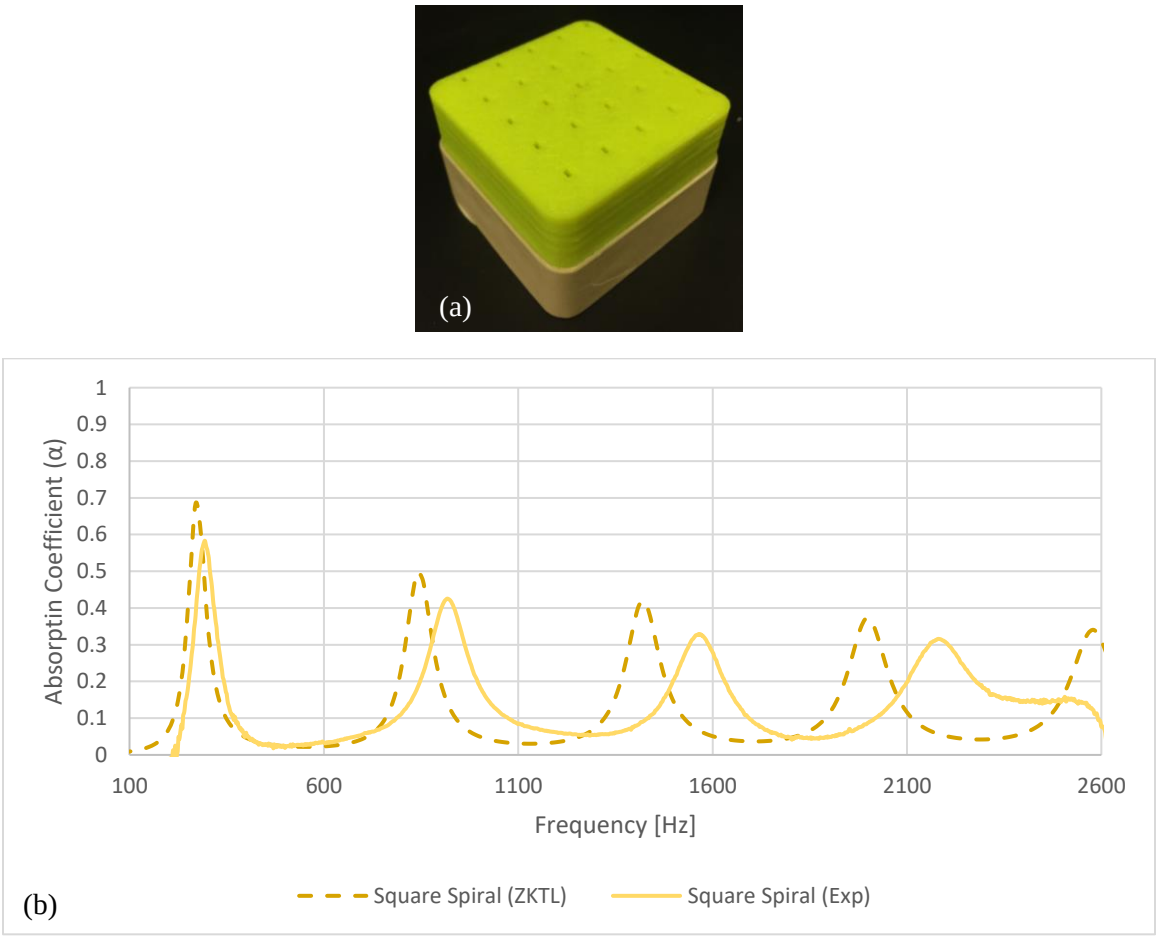

Figure 68: (a) Square Spiral test article and (b) absorption coefficient spectrum. (Δf =2 Hz)

Figure 68 shows that a slight frequency shift in the experimental spectrum from the predicted spectrum is introduced for the Square Spiral design. As the frequency increases, the experimental data seems to shift further away from the ZKTL data. The most probable explanation for this shift is that each of the cavities became partially blocked near the end of the cavity due to the printing process. Another possible explanation is that the shift is caused by non-uniform smoothness of the cavity walls due to printing the spiral cavity without internal supports using an extrusion

printing method. In the Circle Spiral design, the cavity was uniformly sloped the entire length of the cavity, while in the Square Spiral design this is not the case. This problem could have possibly been avoided by using a different 3D printing process, or by having more control of the extrusion process with the Makerbot printer. Although the first peak location is within the target frequency range, the magnitude never exceeds 0.6, therefore no LFP can be calculated.

3.3.9 Broadband Spiral Insert Results

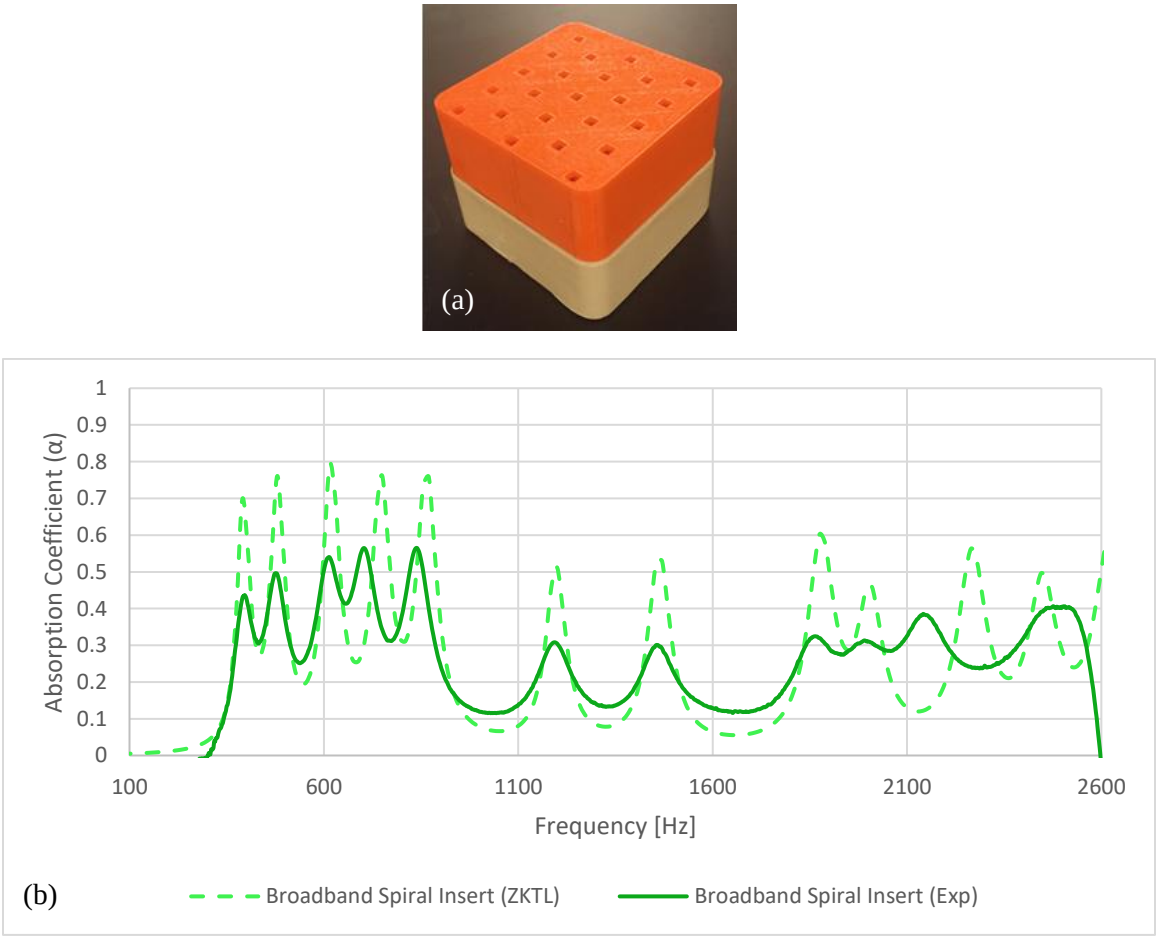

Figure 69: (a) Broadband Spiral Insert test article and (b) absorption coefficient spectrum. (Δf =2 Hz)

For testing and ease of manufacturing, this design was printed as a solid block of ABS instead of being printed as a honeycomb insert. Figure 69 shows that the peak locations from the experimental results match well with the peak locations predicted by the ZKTL simulation results. However, the magnitude of absorption is much less than predicted. This is likely due to the inaccuracy involved with printing small holes using an extrusion-type printing method. Due to the decreased magnitude, no LFP can be calculated from this test article.

3.3.11 Sintered Folded Cavity Results

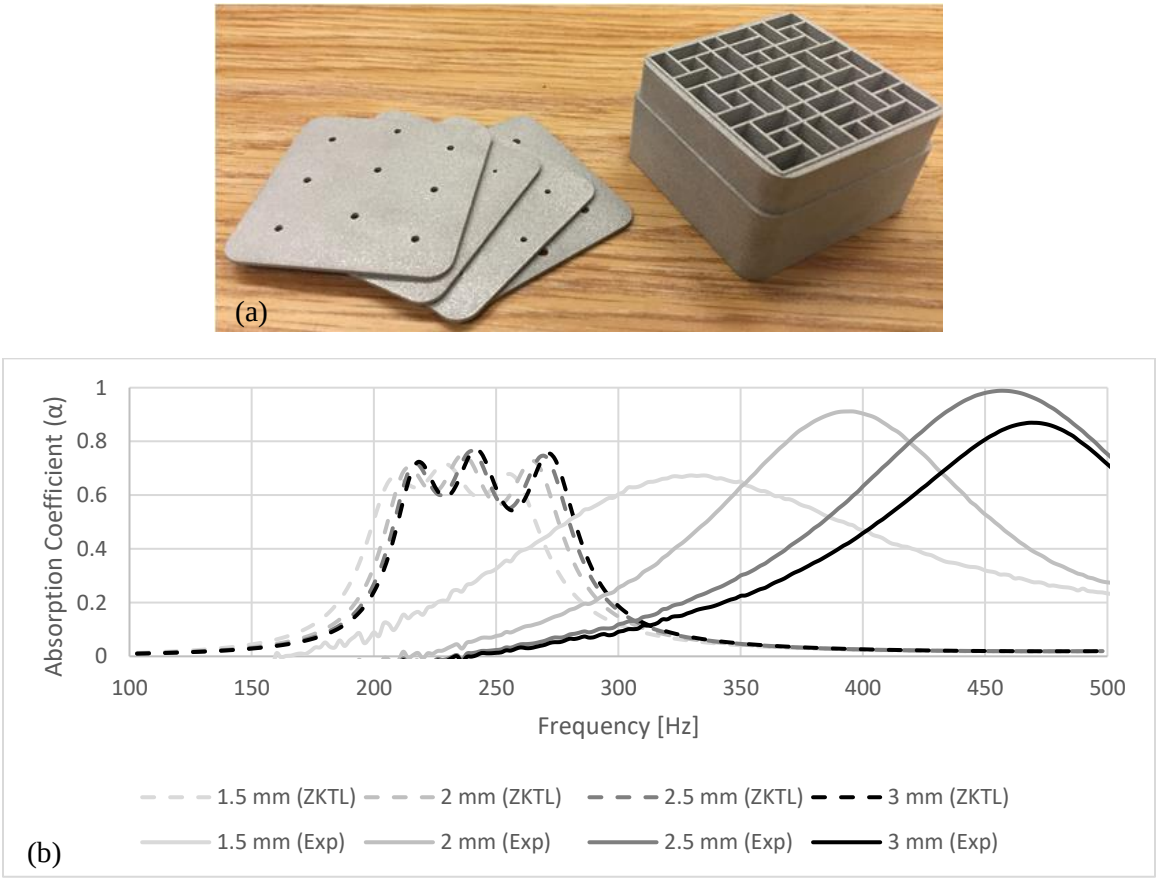

Figure 70: (a) S7 test article and (b) absorption coefficient spectrum. (Δf =2 Hz)

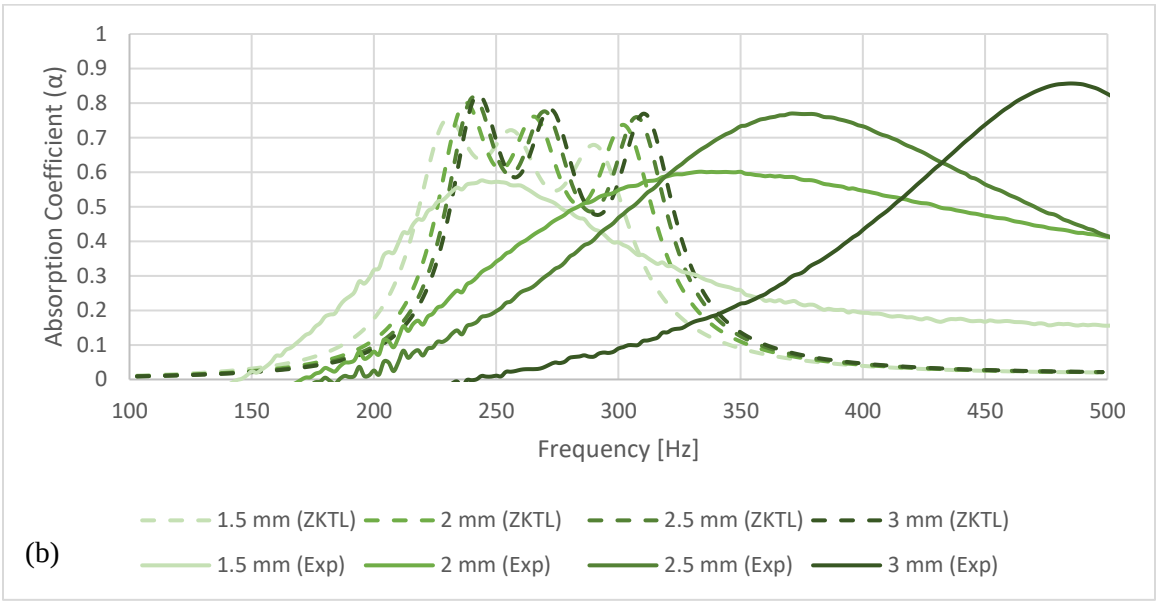

Figure 71: (a) S2 test article and (b) absorption coefficient spectrum. (Δf =2 Hz)

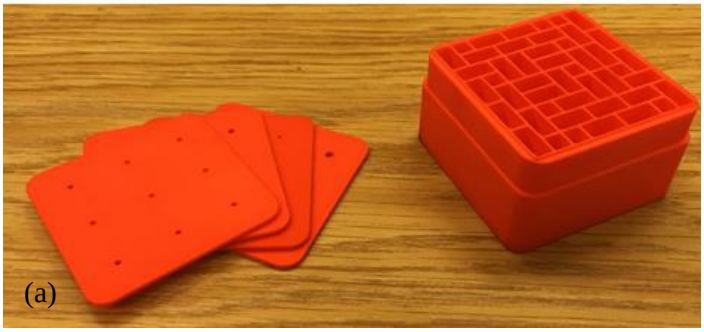

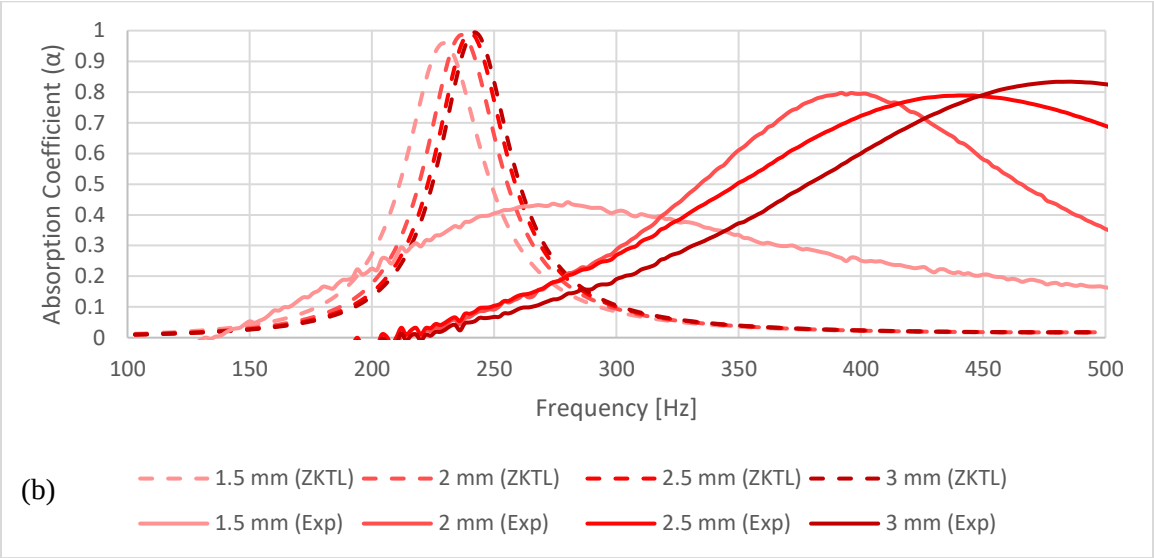

Figure 72: (a) S6 test article and (b) absorption coefficient spectrum. (Δf =2 Hz)

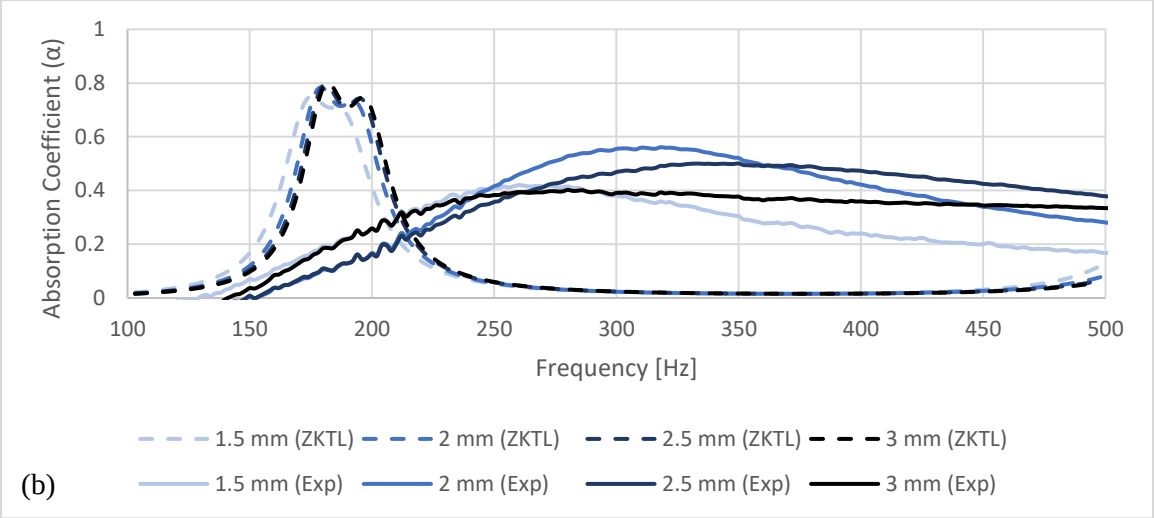

Figure 73: (a) S5 test article and (b) absorption coefficient spectrum. (Δf =2 Hz)

Figures 70, 71, 72, and 73 show that the experimental absorption coefficient spectrum for each of the sintered design configurations do not match with the absorption coefficient spectrum predicted by the ZKTL code. The discrepancy between the predicted and experimental results was originally thought to be a result of the way the face sheets were attached to the cores. To test this theory, one of the S7 configurations was tested again. For the second test, the face sheet was attached to the core using super glue instead of masking tape. Results showed that gluing the face sheet as opposed to taping it to the core did not affect the absorption spectrum enough to explain why the experimental spectrum didn't match the predicted spectrum. The next theory to explain the discrepancy was that the 1 mm thick internal walls were not acoustically rigid. This would explain why the absorption spectrum became smeared and shifted. To test this theory, the S7 design was re-printed using the Makerbot extrusion printer. Because of the previous designs that showed good agreement between ZKTL prediction and experimental results using test articles printed with this method, if the results still did not match it would seem to indicate non-locally

reacting behavior was occurring in the liner. Which would indicate that the internal walls were not acoustically rigid. Results from the Makerbot printed S7 experiment is shown in Figure 74.

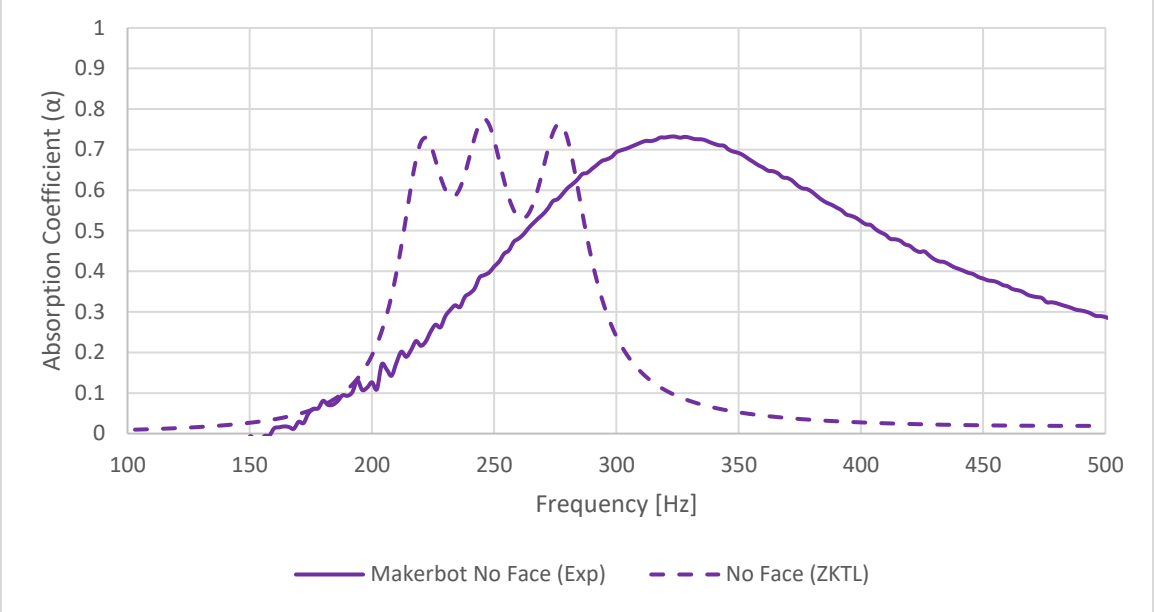

Figure 74: S7 absorption coefficient spectrum for the Makerbot printed test article. (Δf =2 Hz)

The resulting absorption coefficient spectrum for the Makerbot printed S7 test article (Figure 74) does not match with the ZKTL simulation. In order to be sure that the wall thickness is the problem, the S7 test article was re-designed so that the internal wall thickness was increased to 2 mm. This subsequently changed the cavity diameter of the design from 5.5 mm to 4.5 mm. Nothing else on the design was changed. The newly designed "S7_2" test article was again printed using the Makerbot extrusion process and tested.

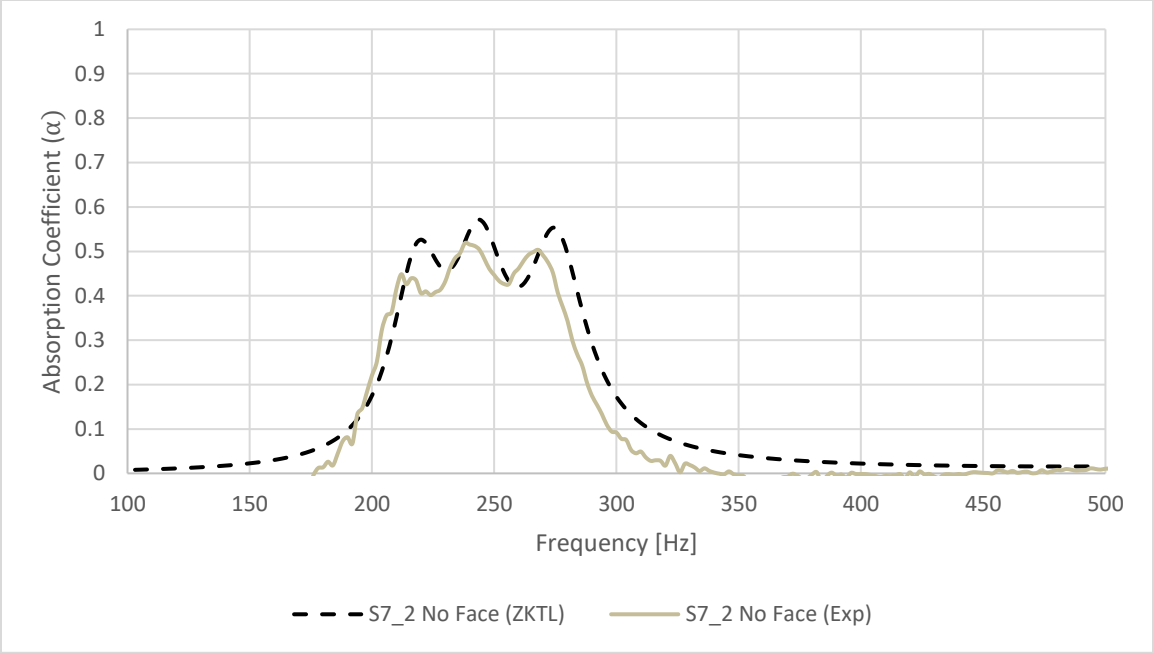

Figure 75: Absorption coefficient spectrum for the S7_2 test article (2 mm thick internal walls). (Δf =2 Hz)

After performing the experiment on S7_2, the conclusion that all liners with an internal wall thickness of 1 mm are not acoustically rigid was reached. However, that conclusion proved to be false upon testing of a Shapeways© sintered plastic Optimized design test article with a 1.5 mm internal wall thickness (shown in the next section). The minimum thickness required for acoustic rigidity is different for ABS than for the Shapeways© sintered plastic. From the tests conducted on the S7 design and variations of that design, it is known that a 1 mm internal wall thickness is not acoustically rigid for liners using ABS plastic in a filament extrusion 3D printing method.

3.3.12 Optimized 3D Folded Cavity Design NIT Results

For the Optimized 3D Folded Cavity NIT design, several different test articles were made using different types of material, and with different 3D printers. Figure 76 shows photographs of each

of them. The yellow one in Figure 76 a) was made out of extruded ABS filament on a Prusa i3 3D printer. The orange one in Figure 76 b) was made using the Makerbot Replicator 2X with ABS extruded filament. The grey one in Figure 76 c) was manufactured by Shapeways© using PLA extruded filament. Lastly, the purple one in Figure 76 d) was made by Shapeways© using the same laser sintering process used for the previous Sintered designs. For notation simplification, the test articles are named according to how they were printed, followed by their color. In the naming notation, the first two letters represent the type of printing (PR=Prusa, MB=Makerbot, and SW=Shapeways©). Figure 76 e) shows the Makerbot printed ABS face sheet used for each of the non-sintered test articles. The face sheet is attached to each of the cores by double sided tape, so that it can be moved between the different designs during testing. Figure 76 f) shows the adaptor sleeve used for the OSU impedance tube so that the exact same samples could be tested in both the OSU tube and the NASA tube.

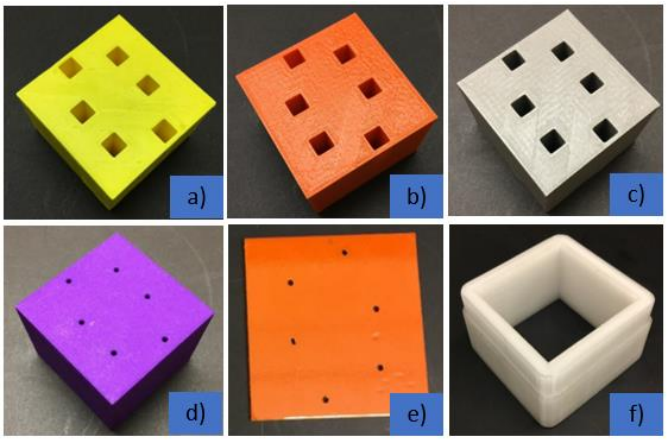

Figure 76: a) PR_Yellow test article; b) MB_Orange test article; c) SW_Grey test article; d) SW_Purple test article; e) ABS face sheet; & f) OSU tube adaptor sleeve.

After printing the face sheet, measurements of its dimensions revealed that it had become slightly altered from the original designed dimensions. Instead of the face sheet holes being 2 mm in

diameter, they were closer to 1.78 mm in diameter with some slight variation between each hole. The thickness was also greater than 1/16 inches and non-uniform across the face sheet. Adding the layer of double sided tape also added to the overall thickness of the face sheet, causing the thickness to be ~2 mm. These changes, although slight, cause a shift in both magnitude and frequency of the absorption coefficient spectrum as shown in Figure 77.

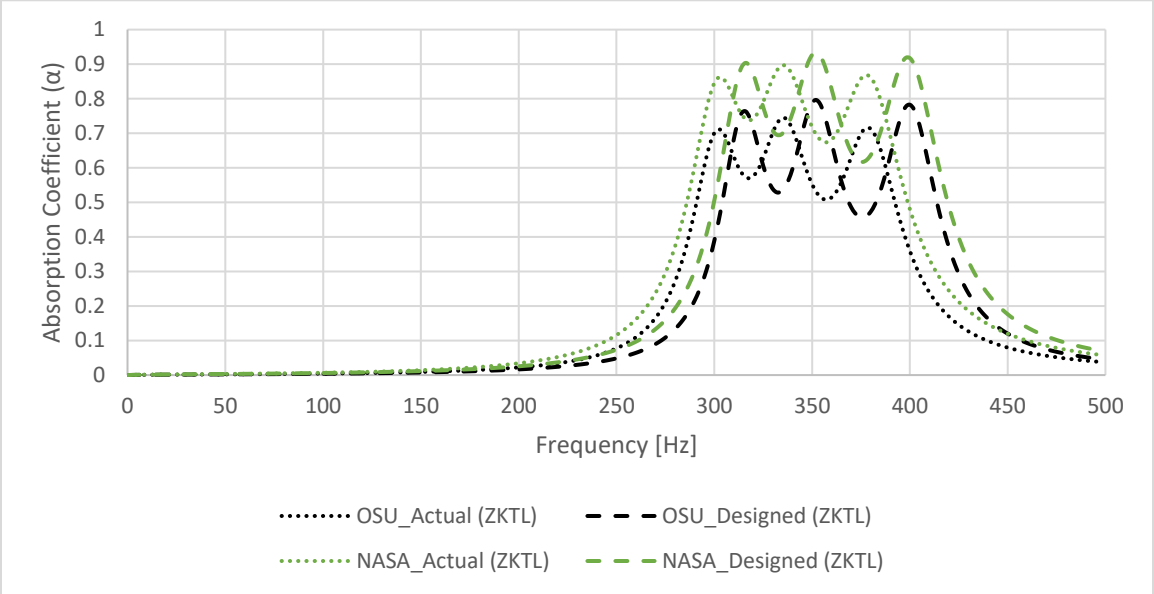

Figure 77: ZKTL simulation results for the Optimized 3D Folded Cavity Liner design with the designed face sheet dimensions and the adjusted actual face sheets dimensions shown.

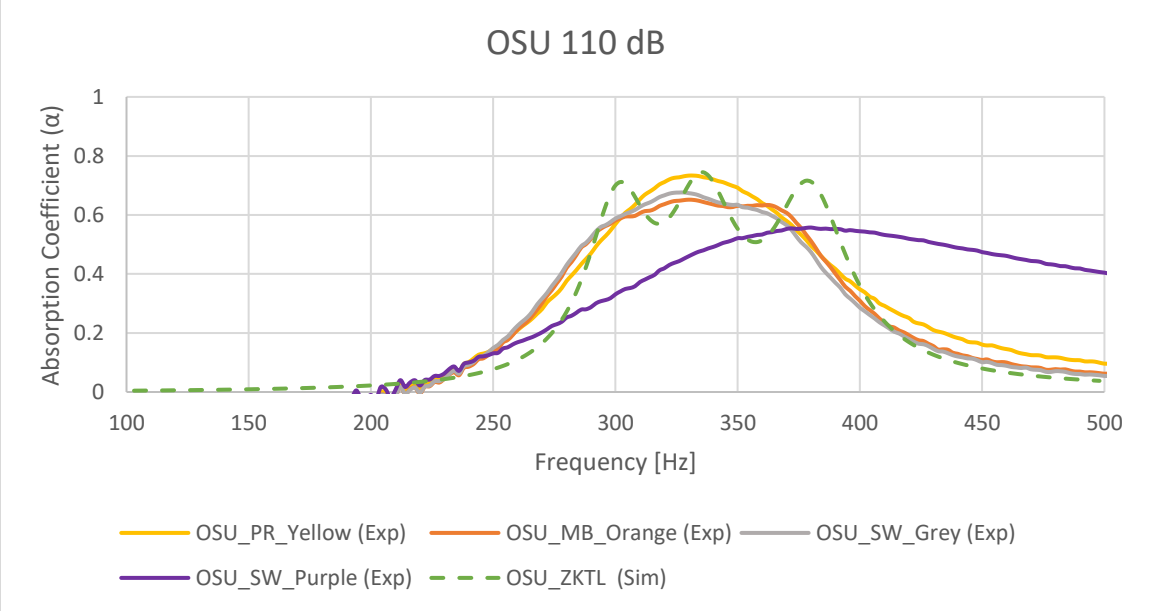

Figure 78: Optimized 3D Folded Cavity Liner design results from the OSU NIT (110 dB). (Δf =2 Hz)

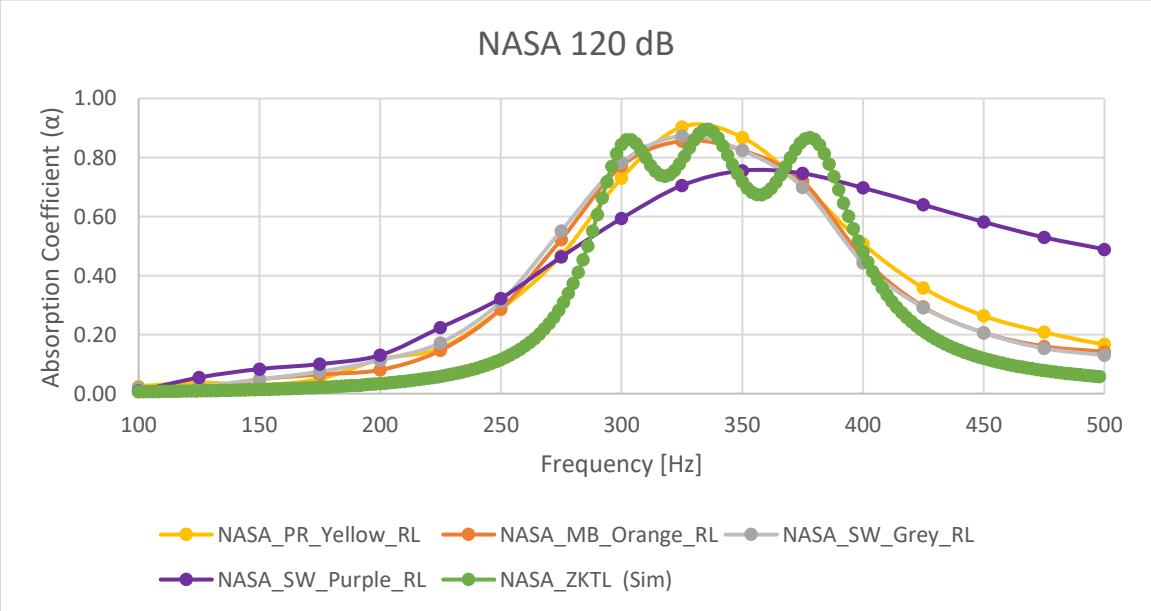

Figure 79: Optimized 3D Folded Cavity Liner design results from the NASA NIT (random low 'RL' broadband test at 120 dB). (NASA Δf =25 Hz; OSU Δf =2 Hz)

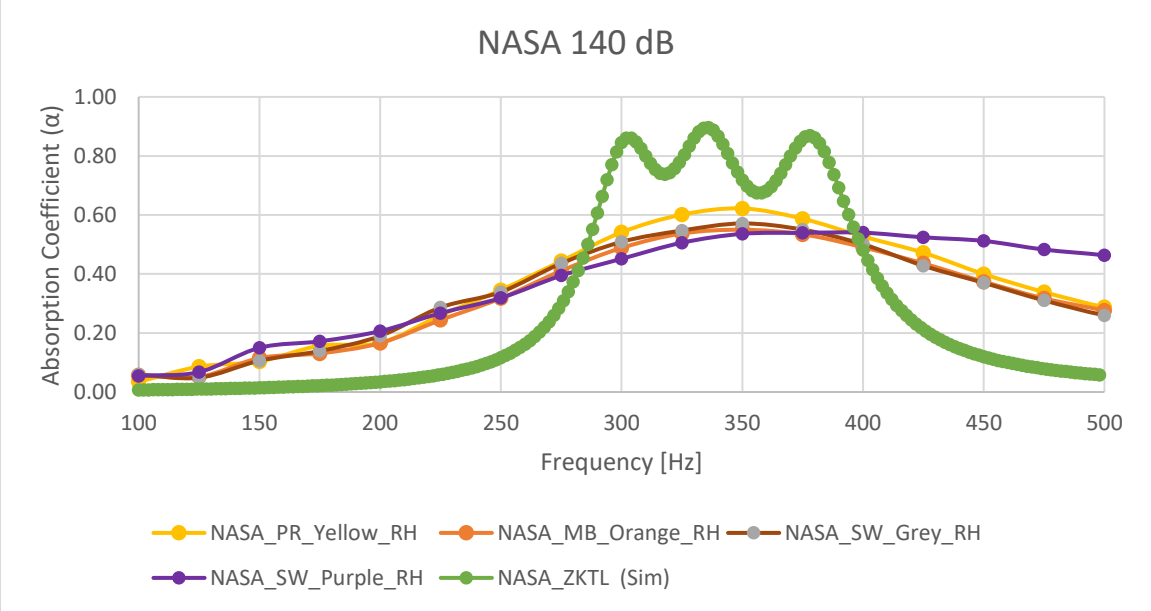

Figure 80: Optimized 3D Folded Cavity Liner design results from the NASA NIT (random high 'RH' broadband test at 140 dB). (NASA Δf =25 Hz; OSU Δf =2 Hz)

Figures 78-80 show the absorption coefficient spectrum from each of the four Optimized design articles, with the adjusted ZKTL simulations shown. The three extrusion-type test articles match closely with each other in all three absorption spectrums, but the Sintered one is shifted to a slightly higher frequency range and a lower magnitude in all three cases. The frequency shift for the sintered design is less pronounced in the NASA tube tests. As the SPL level used for the testing increases, the performance of the sintered design become more comparable to the other designs. Note that as the SPL level increases, the absorption peak becomes less pronounced. A decrease in absorption coefficient magnitude is seen when the NASA tube is transitioned from 120 dB to 140 dB. The shift to a lower magnitude absorption in the OSU tube occurs as expected because of the active area difference between the tubes. Figures 81-84 show the absorption coefficient spectrums for each of the distinct Optimized 3D Folded Cavity design test articles.

Appendix A.1 shows the entire absorption coefficient spectrum (100-3000 Hz) for all of the NASA tests along with the impedance plots for each of the Optimized designs.

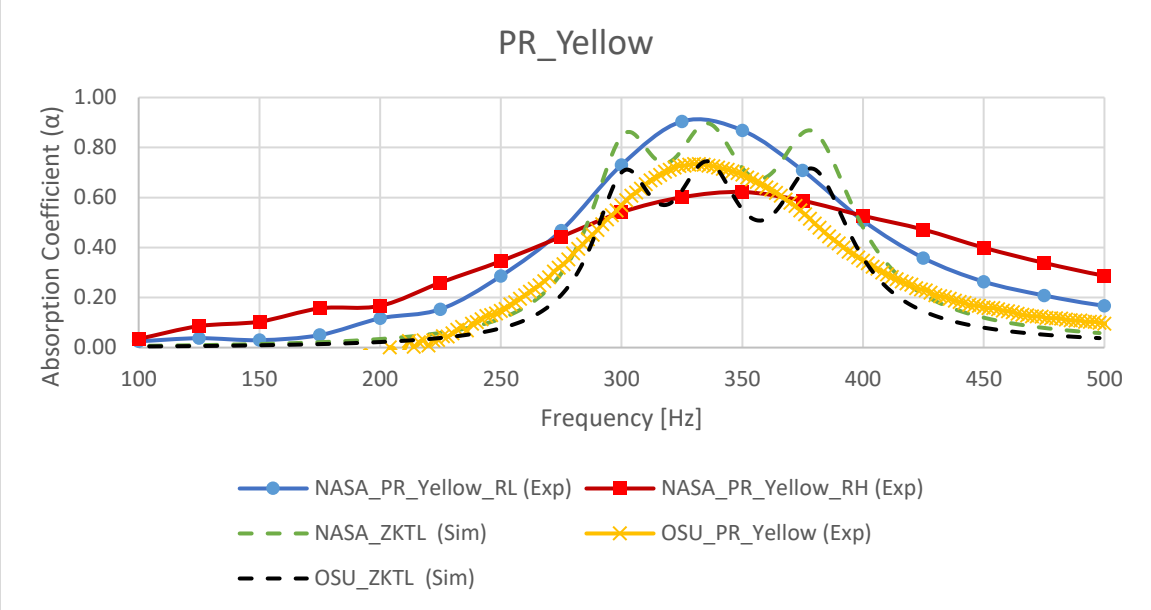

Figure 81: PR_Yellow test article absorption coefficient spectra. (NASA Δf =25 Hz; OSU Δf =2 Hz)

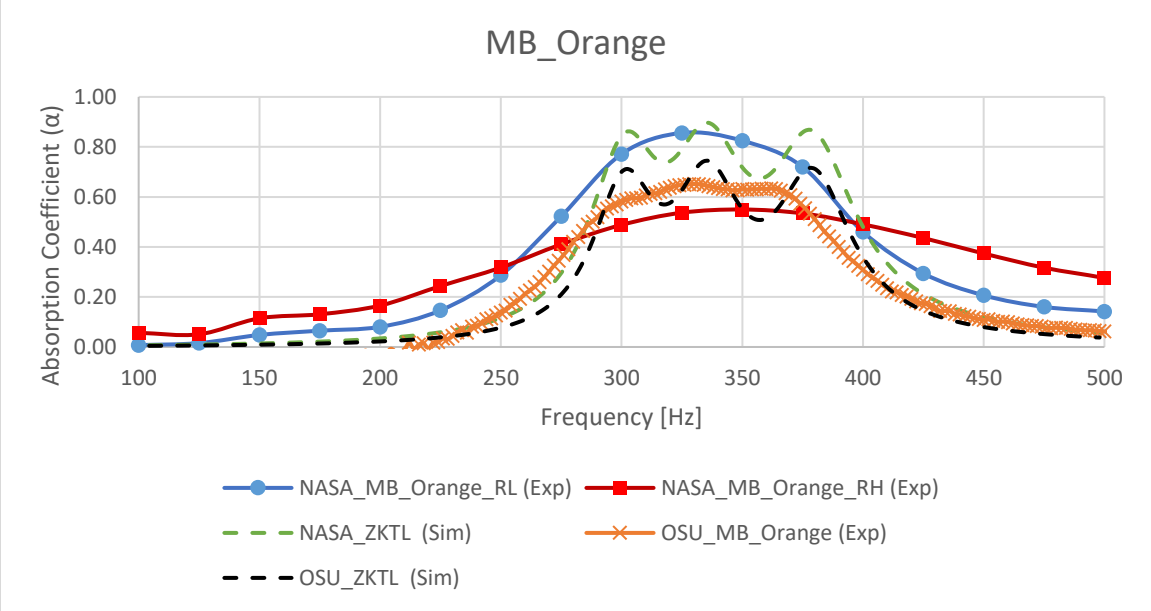

Figure 82: MB_Orange test article absorption coefficient spectra. (NASA Δf =25 Hz; OSU Δf =2 Hz)

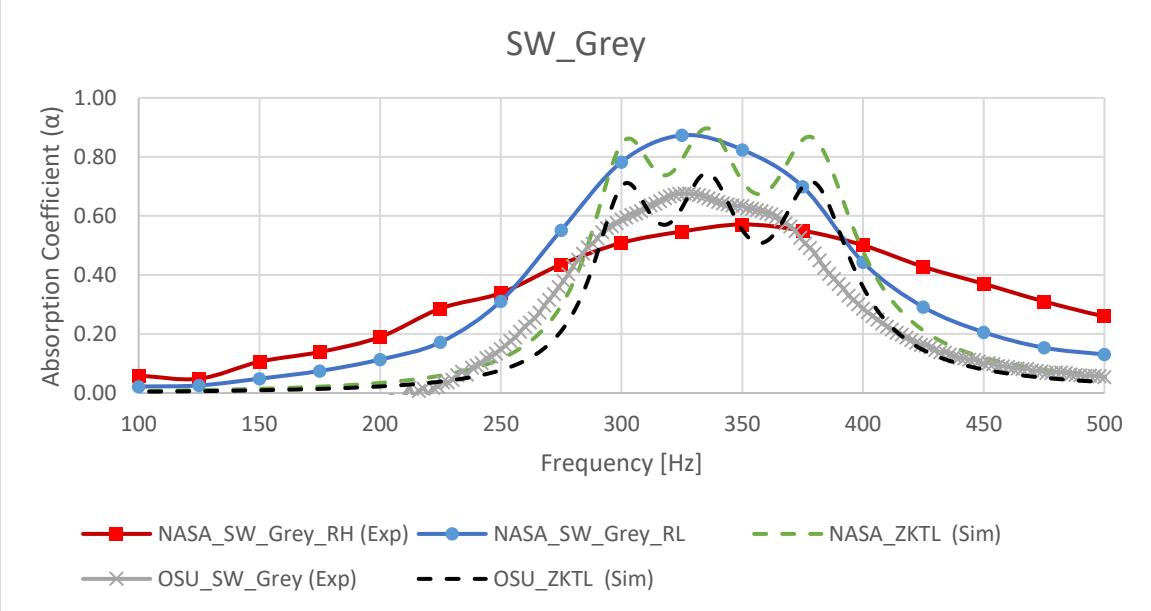

Figure 83: SW_Grey test article absorption coefficient spectra. (NASA Δf =25 Hz; OSU Δf =2 Hz)

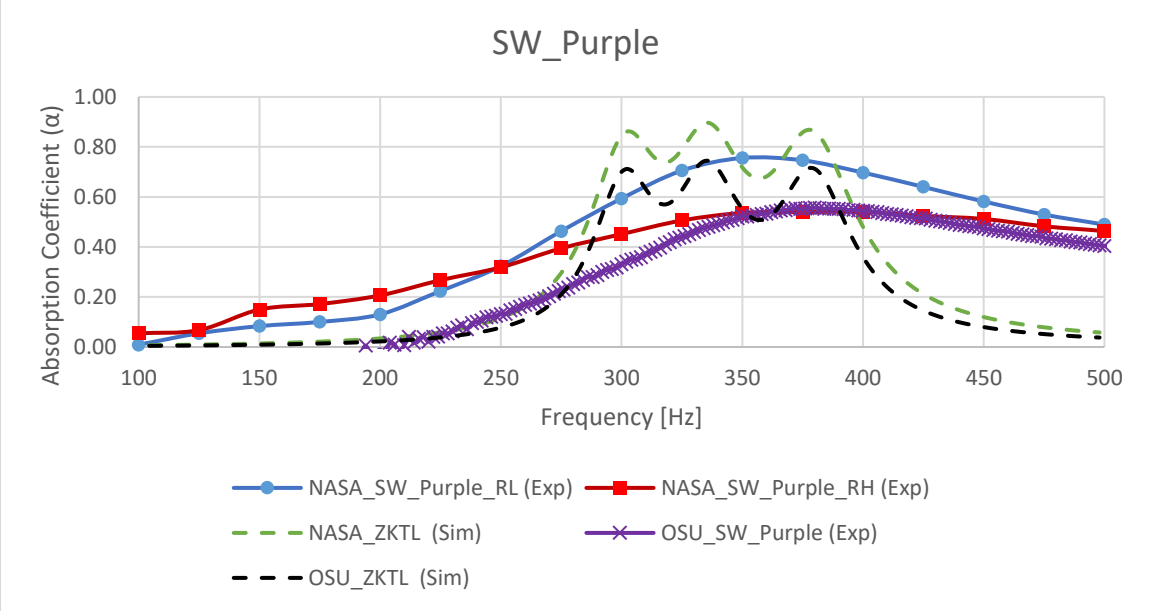

Figure 84: SW_Purple test article absorption coefficient spectra. (NASA Δf =25 Hz; OSU Δf =2 Hz)

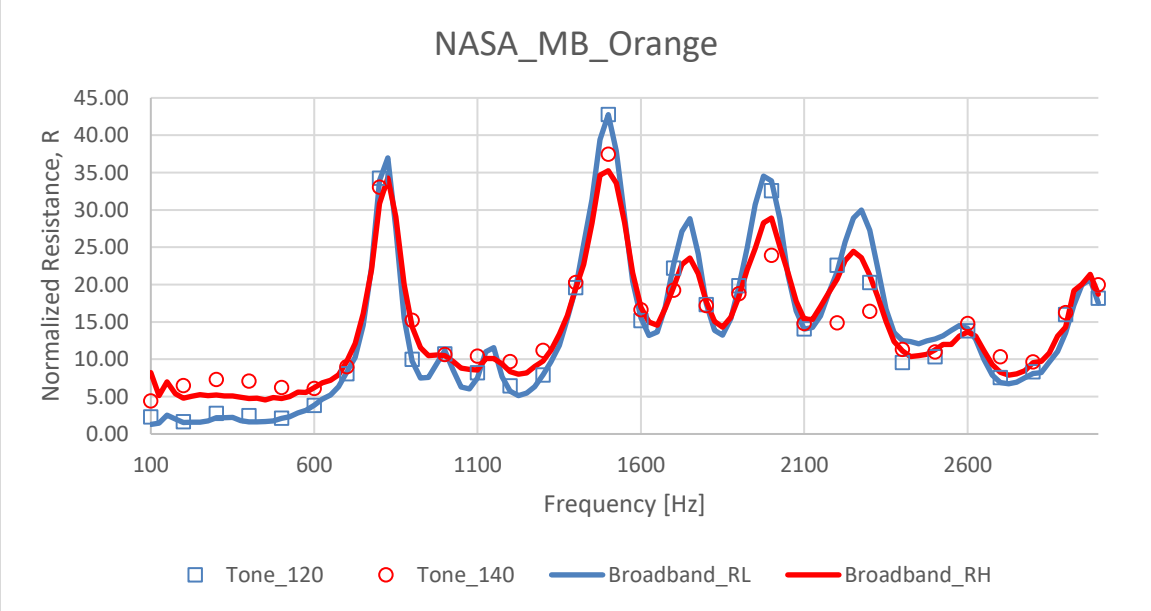

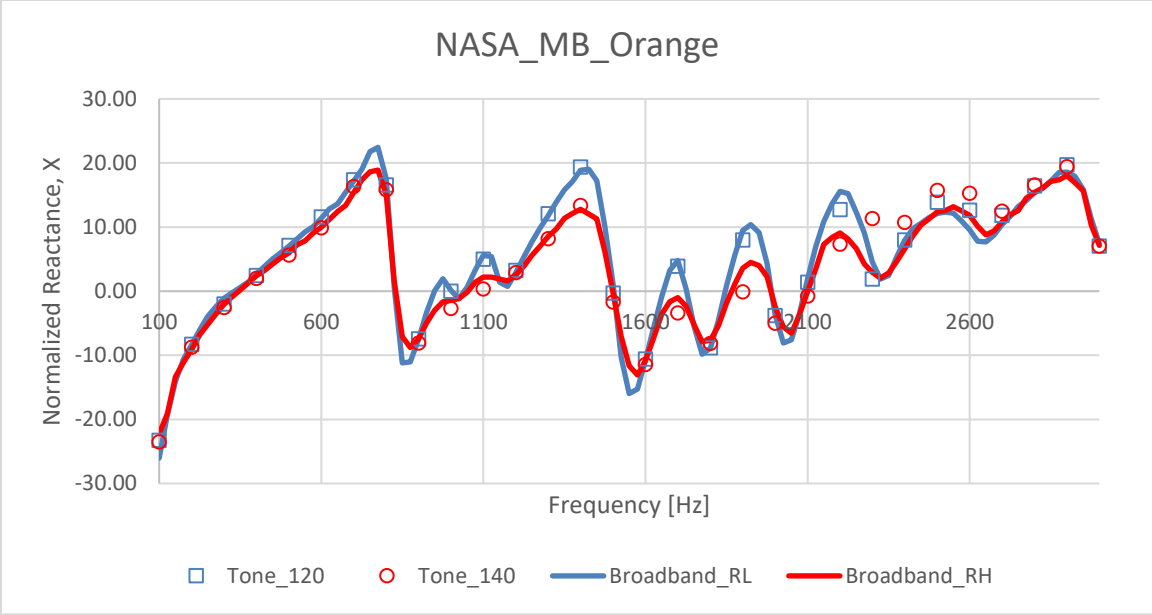

Figure 85: Impedance plots for the MB_Orange article for broadband and tonal tests conducted in the NASA NIT.

Figure 85 shows that good correlation between tone tests and broadband tests exist for the entire impedance spectrum for the MB_Orange test article. Similar correlation is seen between tone and broadband tests for the other test articles. Estimation of errors for the experiments on the Optimized 3D Folded Cavity Liner designs arising from effects of repeatability, fabrication, and the eduction process is given in Appendix A.2. Uncertainty analysis for both the NASA NIT [43] and the NASA GFIT [44] has been conducted, and is reported in detail in the literature. Significant nonlinearity is noticed when the sound intensity was increased from 120 dB to 140 dB in the NASA NIT for each of the four test articles tested. Based on previous research by Ingard and Labate [42], it is conjectured that this observed nonlinear behavior is dependent on vortex shedding at the face sheet hole, and the convection velocity of the shed vortices. While good correlation is observed between the predicted and actual absorption spectra, the resonance peaks seen in the predictions due to the tuning of the folded cavity lengths for each of the three pairs of

clusters in the final configuration are indistinguishable in the experiments. It was noted that the 3D printed face sheet dimensions would be slightly altered from the design specifications. The average dimension changes were accounted for in the ZKTL simulation to more accurately predict the performance, but smearing was still not seen in the simulations. In an attempt to try and replicate the smearing effect seen in the experimental results, the face sheet hole sizes were perturbed in the ZKTL code so that each hole is slightly different for each of the six cavities in the test article. By systematically changing the face sheet hole size for each of the six cavities through a trial and error process, the smeared experimental absorption coefficient spectrum was more closely matched. Figure 86 shows that by slightly changing the diameter of each of the six face sheet holes, a smeared peak can be predicted using the ZKTL code. The experimental results from the PR_Yellow test article were used in Figure 86 because for each of the three NIT tests, the absorption spectrum from that test article most closely matched with the previous ZKTL simulation in the low-frequency range.

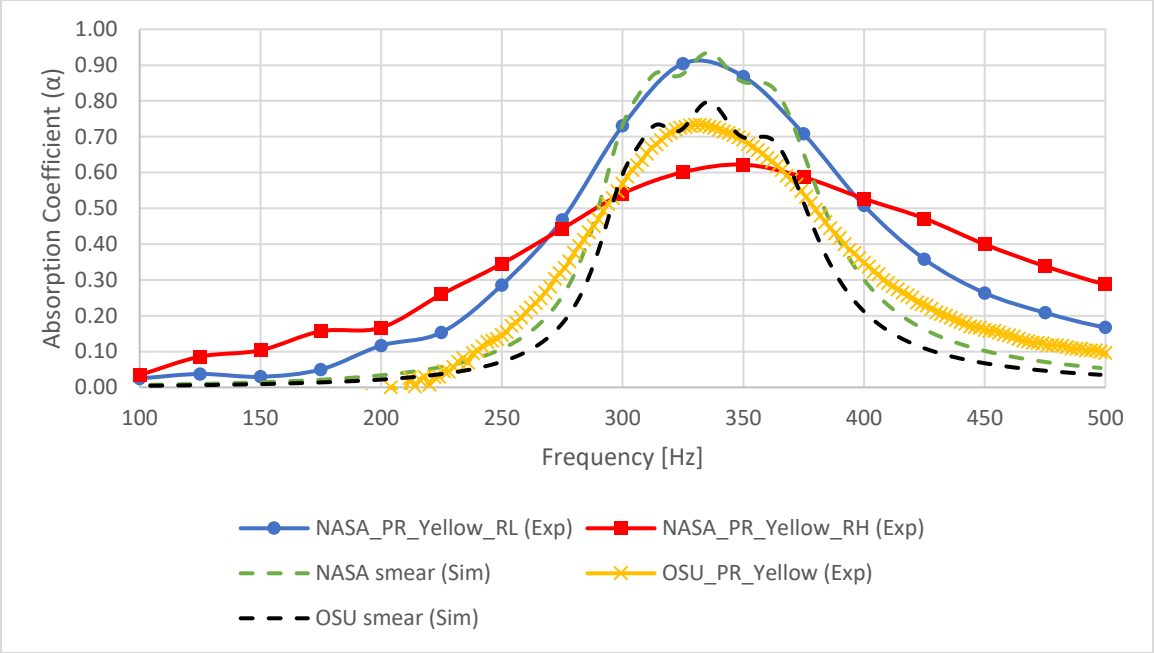

Figure 86: Comparison of experiments to simulations with perturbed face sheet hole diameters. (NASA Δf =25 Hz; OSU Δf =2 Hz)

Owing to the non-uniformity arising from the printing process for the face sheet whose key dimensions are comparable to the print resolution and other unexpected variations for the printing process, it is reasonable to explore their effects in the simulations. Each face sheet hole was examined closely using a microscope and differences were observed (Figure 87). Based on observed variations in the printed face sheets, the face sheet hole diameters for each cluster in the 6-cluster configuration were perturbed by amounts within +/-20%. Therefore, instead of having 3 pairs of identical clusters, the simulation inputs were changed so that there were 6 distinct clusters.

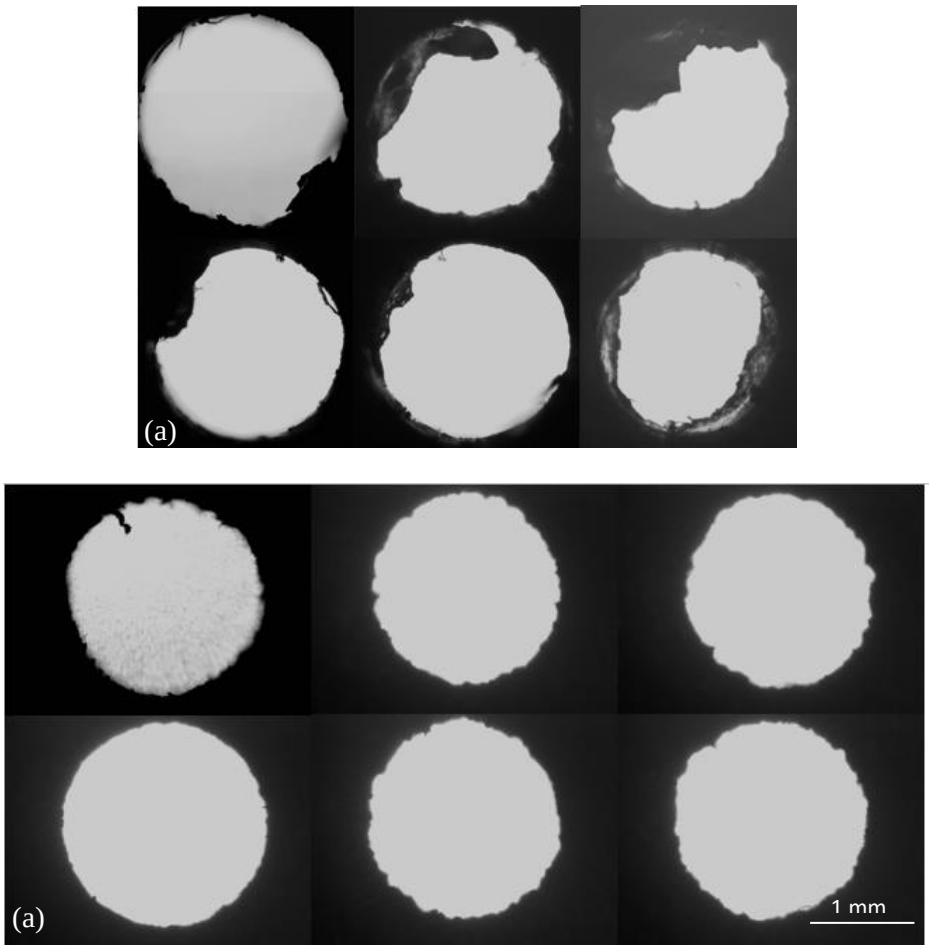

Figure 87: Observed face sheet hole differences as seen in a microscope for (a) the ABS face sheet and (b) the Sintered face sheet.

Comparison with experiments shown in Figure 86 reveals that the predicted absorption coefficient spectrum does indeed become more smeared as seen in the experiments when the type of variation in the face sheet hole diameter arising from the printing process is accounted for. Peak absorption within the targeted bandwidth shows close agreement with tuned resonances in the simulations. However, as is typical of viscous effects unaccounted for in the model but to be expected in practice, dissipative contributions to absorption over the entire frequency range renders the measured absorption higher than the prediction outside of the resonance-driven

bandwidth. Thus, it is found that the ZKTL-based optimization procedure using the LFP factor provides a fairly accurate design methodology to realize 3D folded cavity acoustic liners that could provide lightweight, compact and structurally-integrated solutions to effectively mitigate low-frequency noise.

3.3.13 Optimized 3D Folded Cavity Design GFIT Results

The acoustic performance of a liner in the presence of air flow is important to understand, especially if that liner is intended to be used in aircraft engines. In order to get an idea how the Optimized 3D Folded Cavity design would perform in the presence of flow, a GFIT test article was designed that is essentially ten of the 2 inch x 2 inch Optimized liners stacked in line with each other within a 3D printer holder that fits inside the testing rig. A 1/16 inch thick Aluminum face sheet (Figure 88) with 2 mm diameter holes was machined and used for testing. Four 0.25 inch diameter alignment holes with corresponding pegs were used to ensure proper alignment of the face sheet to the core. Like the NIT test articles, the face sheet was attached with double-sided tape. In addition to testing the perforated aluminum face sheet configuration, the test article was tested without a face sheet, and with a 27 Rayl (cgs) wire mesh face sheet (R27). Each variation was tested with no flow at 120 dB and 140 dB. The perforated aluminum face sheet variation was additionally tested with Mach 0.3 flow at 120 dB and 140 dB, and Mach 0.5 flow at 140 dB. The R27 wire mesh was additionally tested with Mach 0.3 flow at 140 dB. The nomenclature for these different configurations include the type (No Face Sheet (NF), Perforated (Perf), Wire Mesh (R27)), Mach number (0, 0.3, 0.5), and dB level (120, 140). Each of these nomenclature distinctions are separated by an underscore "_" in their respective names.

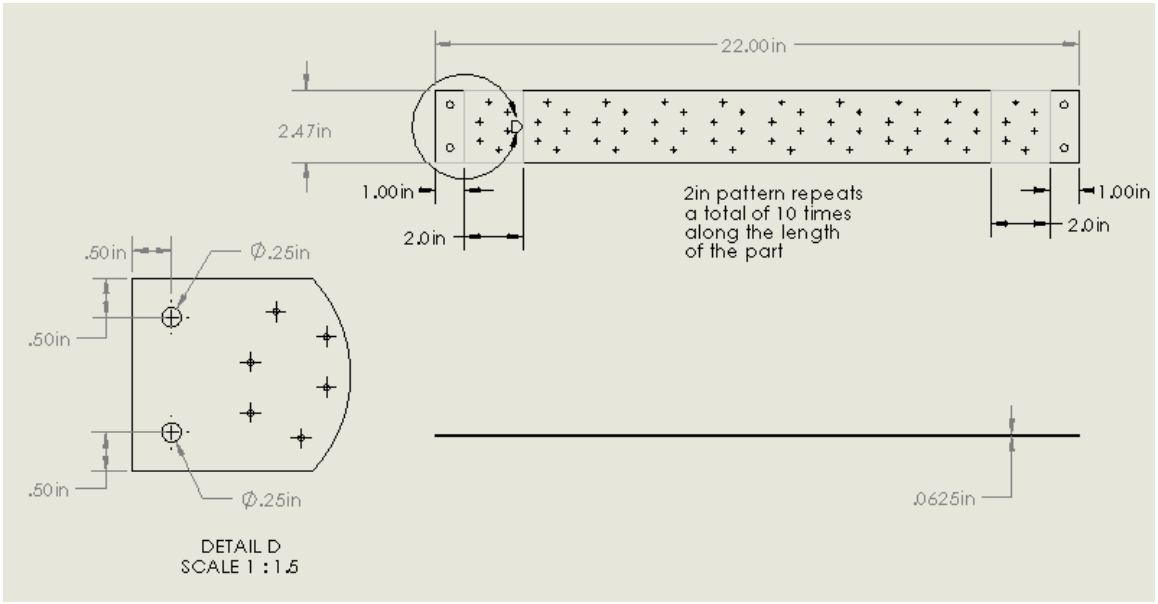

Figure 88: GFIT perforated aluminum face sheet CAD drawing.

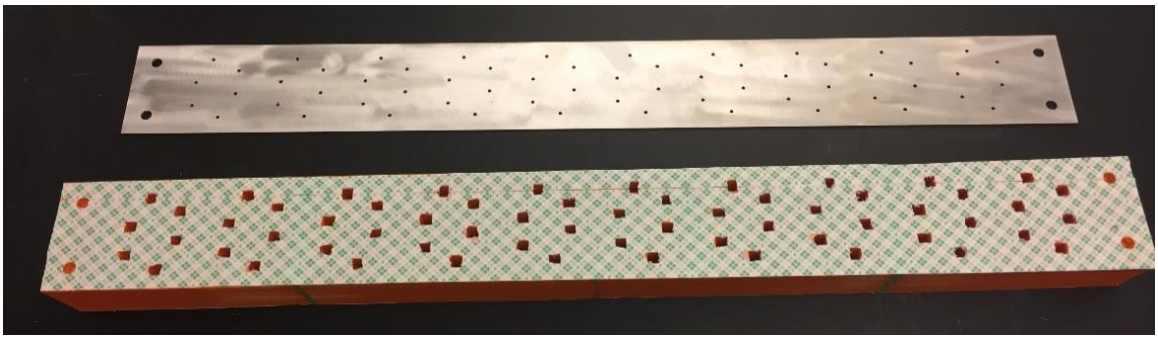

Figure 89: Photograph of GFIT test article core and perforated aluminum face sheet.

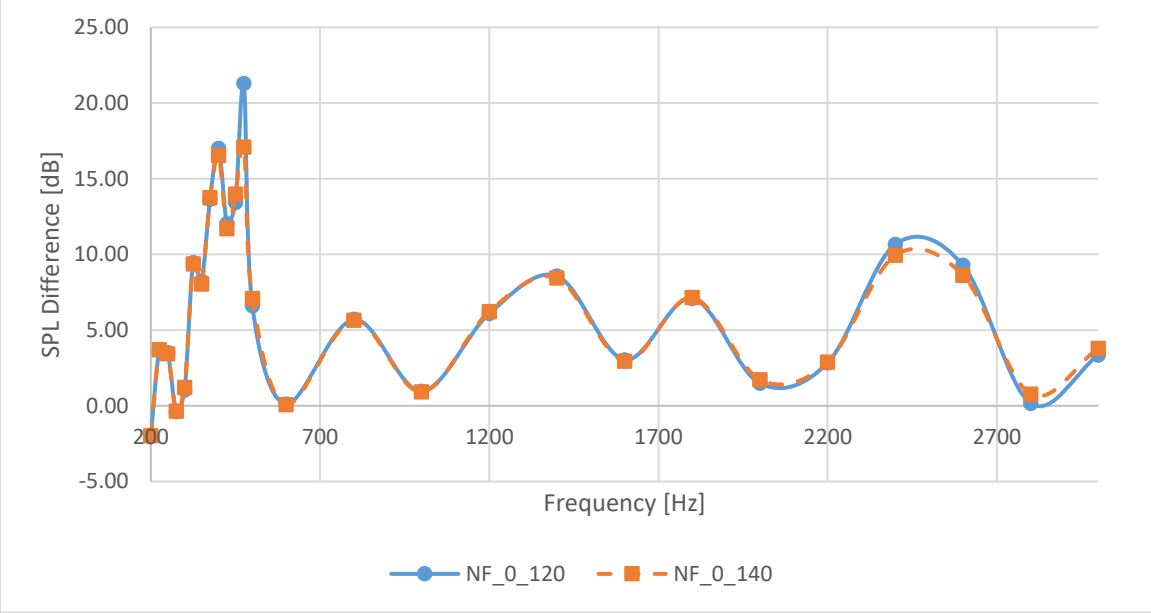

Figure 90: No face sheet GFIT test results showing SPL difference between upstream and downstream microphones.

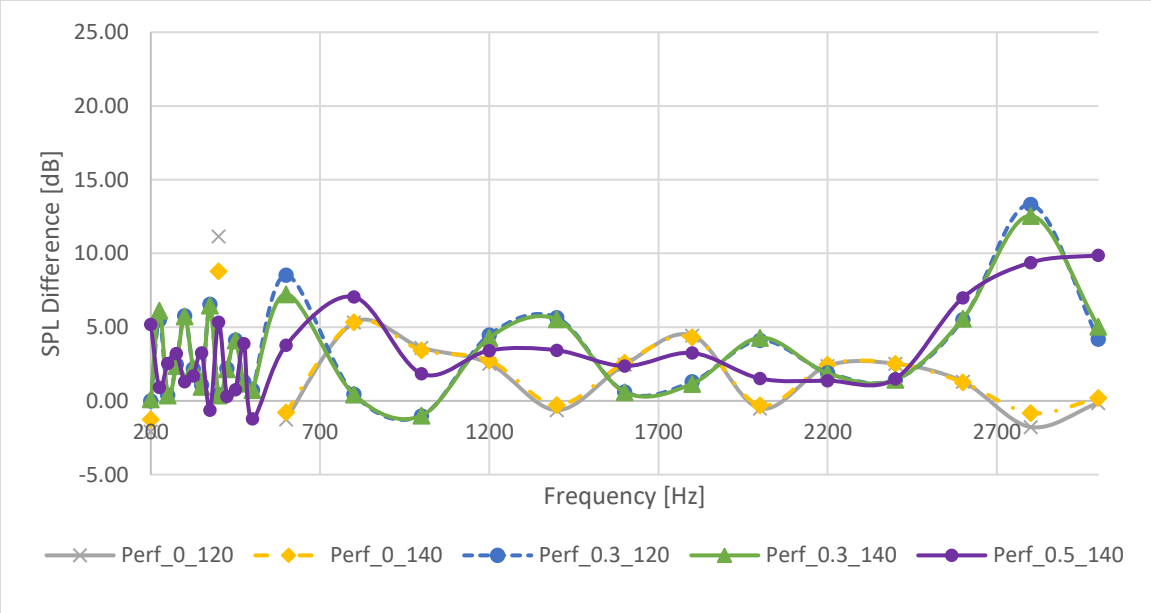

Figure 91: Perforated aluminum face sheet GFIT test results showing SPL difference between upstream and downstream microphones.

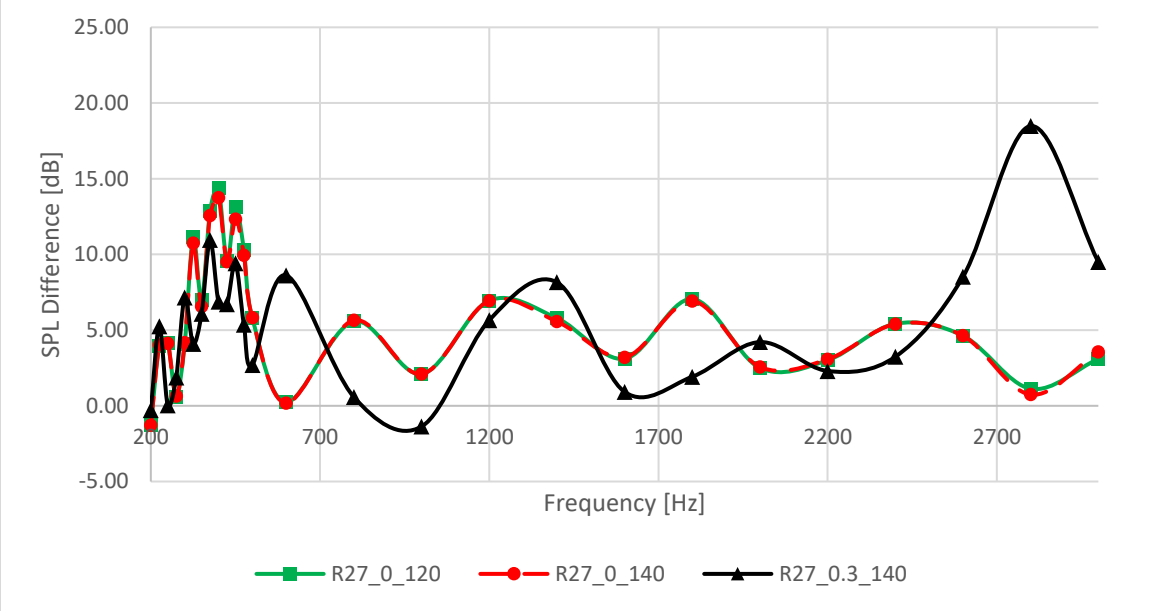

Figure 92: R27 wire mesh GFIT test results showing SPL difference between upstream and downstream microphones.

As shown in Figures 90-92, the decrease in SPL varies depending on the tonal frequency emitted in the tube. Figure 90 shows that a relatively equal SPL decrease is seen in the no-face sheet case with no flow at both 120 dB and 140 dB. Because there is no flow, and the GFIT test article is simply multiple Optimized 3D Folded Cavity design NIT test articles added together, the peak performance should occur in the low-frequency range predicted by the ZKTL code for the NIT test article without a face sheet. Figure 90 shows that the largest decrease in SPL is in fact observed in that predicted low-frequency range. In Figure 91, when the perforated face sheet is added, it is observed that the decrease in SPL level in the low-frequency range is not as large as it was for the no face sheet configuration. A slight decrease in the magnitude of the SPL difference is seen when flow is introduced to the tube. At Mach 0.3, the perforated configuration performed approximately the same for both the 120 dB and 140 dB levels. This suggests that the Mach number has a greater influence over the liner performance than the starting SPL level does. The

no flow tests for the perforate configuration also match well for both SPL levels. This trend is seen not only for the no face sheet case and the perforated face sheet case, but for the R27 wire mesh configuration as well. Figure 92 shows that this is the case, and that when flow at Mach 0.3 is introduced, the magnitude of SPL drop across the liner is decreased from the no flow case at the same reference dB level.

3.4 Chapter Summary

Chapter 3 examines the experimental testing setup for the OSU and NASA normal incidence impedance tubes and the NASA grazing flow impedance tube. All NIT experiments conducted satisfy the requirements as specified by ISO 10534-2:1998 [37]. Two different 3D printing processes were utilized, fused filament fabrication, and selective laser sintering. The by-hand manufacturing process used to create the Helmholtz Baseline 1 design is also discussed in detail. Resulting absorption coefficient spectrums from the various experimental tests are compared to their respective predicted simulations. Excellent agreement is seen between experimental and simulation results for each of the designs, with the exception of the Sintered designs. Shift to the low-frequency regime is shown to occur as the length of the folded cavities are increased. Lastly, results from the GFIT design configurations show good SPL decrease across the liner in the presence of flow within the expected low-frequency range below 500 Hz.

CHAPTER 4

CONCLUSIONS AND RECOMMENDATIONS

4.1 Conclusions

It was demonstrated that by efficiently packing folded cavities into a prescribed liner volume, exceptional broadband absorption can be achieved at frequencies below 500 Hz. Excellent agreement between the ZKTL simulation results and experimental results for each of the designs tested was observed. The combination of the Low-frequency Performance (LFP) factor and the Folded Cavity Packing Optimization Code was used to efficiently pack 3D folded cavities into a given volume to obtain noise absorption solutions tailored for a specific low-frequency bandwidths. The LFP factor provided an excellent way to compare different liner designs that exhibited absorption in the low-frequency range below 500 Hz. Table 4 shows a detailed comparison of each of the designs discussed in this thesis. Note that the Sintered design test articles (S7, S2, S6, and S5) are shown with parameters corresponding to the best LFP configuration exhibited by the experimental absorption results. The parameters listed for the Sintered design in Table 4 do not match the parameters listed in Table 3, because of the discrepancy between experimental and simulation results discussed. Also note that the Triangle 10-Fold Insert design and the two Hypothetical Teardrop designs were not manufactured, therefore were not able to be experimentally tested. The parameters listed in Table 4 for those designs are from their respective ZKTL simulation results.

Design (Experimental)	1st peak location [Hz]	β	LFP	t [in]	t_w [mm]	Material	nc	d_c [mm]	Active Area [in^2]
Quarter Wave Baseline	2002	N/A	N/A	1.7485	5.29	ABS	25	6.35	6.2
Helmholtz Baseline	588	212	N/A	2.125	0.07	Aluminum	10	14.224	6.2
L-Liner Baseline	2002	N/A	N/A	1.7485	3.63	ABS	30	*varries	6.2
L-Liner	926	760	N/A	1.7485	3.63	ABS	30	*varries	6.2
U-Liner Baseline	1930	138	N/A	1.7485	1.59	ABS	25	4.5974	6.2
U-Liner	1054	170	N/A	1.7485	1.59	ABS	25	4.5974	6.2
U-Liner Face Sheet	714	184	N/A	1.811	1.59	ABS	25	4.5974	6.2
PSU Baseline	978	122	N/A	1.7485	1.59	ABS	20	4.5974	6.2
PSU	1148	162	N/A	1.7485	1.59	ABS	20	4.5974	6.2
PSU Face Sheet	750	136	N/A	1.811	1.59	ABS	20	4.5974	6.2
W-Liner Baseline	1944	212	N/A	1.7485	1.59	ABS	25	4.2926	6.2
W-Liner	500	78	15.76	1.7485	1.59	ABS	25	4.2926	6.2
W-Liner Face Sheet	422	94	24.35	1.811	1.59	ABS	25	4.2926	6.2
Circle Spiral	364	30	5.82	1.7485	1.52	ABS	25	2.6924	6.2
Square Spiral	300	N/A	N/A	1.7485	1.52	ABS	25	2.6416	6.2
Broadband Spiral Insert	404	N/A	N/A	2	1.52	ABS	25	3.556	6.2
S7 - 2.5mm Face Sheet	458	124	30.9	1.5625	1.00	Sintered Plastic	9	5.5118	6.2
S2 - 2.5mm Face Sheet	372	122	29.36	1.5625	1.00	Sintered Plastic	10	5.5118	6.2
S6 - 3mm Face Sheet	486	198	41.28	1.5625	1.00	Sintered Plastic	9	5.5118	6.2
S5 - 2mm Face Sheet	312	N/A	N/A	1.5625	1.00	Sintered Plastic	7	5.5118	6.2
Opt (NASA, PR_Yellow)	335	100	31.6	1.5625	1.50	ABS	6	6.7	4
Design (Simulation)									
Triangle 10-Fold Insert	255	30	10.88	2	0.2	N/A	14	5.6	6.2
Hyp.Teardrop Sim 12	165	119	83.58	2.125	0.07	N/A	150	~ 4	6.2
Hyp.Teardrop Sim 10	166	105	65.91	2.125	0.07	N/A	150	~ 4	6.2

Table 4: Comparison of parameters for various designs considered in this study.

The baseline designs provided a point of comparison for improved low-frequency folded cavity liner designs. The 2D folded cavity designs (L-Liner and U-Liner) demonstrated that a 2D folded cavity behaves as a straight cavity of equal length, and that introducing folds can shift absorption to lower frequencies. The Phased Slanted U-Liner showed that by creating non-linearity in a folded cavity liner, the bandwidth of absorption can be increased. The W-Liner demonstrated that targeted absorption below 500 Hz can be achieved by folding cavities in a 3D volume representative of a typical acoustic liner (1.59 inches). The spiral designs showed the importance of accuracy in the additive manufacturing process, and that broadband absorption can be achieved by using a combination of different 3D folded cavity lengths in the same liner article. The Sintered designs shed light on the importance of ensuring the acoustic rigidity of internal walls

separating the distinct cavities within a liner. The ZKTL simulation results from the Sintered designs showed that the peak spacing required to achieve a continuous bandwidth changes depending on the frequency range. At lower frequencies, cavity lengths need to be spaced closer together, and at higher frequencies the cavity lengths can be spaced further apart. Optimizing the relative lengths of the folded cavities to tune the peak locations in the absorption coefficient spectrum helps enhance the bandwidth of absorption that the liner exhibits. More than 100 Hz of continuous bandwidth with absorption coefficient greater than 0.6 is shown to be possible in the 300 to 400 Hz range with the Optimized 3D Folded Cavity Design. The introduction of flow to the GFIT test article showed that as the speed of the air flow increased, the amount of noise attenuated decreased. When flow is considered, the resistance of the face sheet drives the amount of attenuation achieved. It was found through a parametric numerical study on liner porosity, that for quarter wave liners, the porosity can be optimized to achieve a maximum absorption coefficient peak. As the cavity size decreases, the absorption mechanism transitions from purely resonance dependent, to predominately dissipation driven.

It was demonstrated that the ZKTL-based optimization procedure using the LFP factor as a performance metric provides a fairly accurate design methodology to realize 3D folded cavity acoustic liners that could provide lightweight, compact and structurally-integrated solutions to effectively mitigate low-frequency noise. With additive and hybrid manufacturing techniques attaining critical commercial maturity in recent times, 3D folded cavity liners could provide a promising practical solution to mitigate low-frequency airborne noise, especially in aerospace applications.

4.2 Recommendations for Future Work

A study of the mechanical properties of the 3D printed liners should be conducted to determine the stiffness as well as the weight of the liners. It is important to determine the amount of weight that would be added if 3D printed folded cavity liners were to replace traditional honeycomb liners being used today. By using metal instead of plastic as the 3D printed material, perhaps the wall thickness could be decreased such that acoustic rigidity is maintained while minimum weight is added. Hybrid manufacturing techniques could also potentially provide adequate strength while retaining a lightweight characteristic.

To determine the minimum wall thickness needed to maintain acoustic rigidly for different 3D printed materials, and in-depth experimental study should be conducted. A selection of potential 3D printed materials (aluminum, ABS plastic, etc.) should be printed in sheets of different thicknesses and tested in a transmission loss tube. The acoustic rigidity of the different sheets could be determined by the amount of sound allowed to pass through the material.

A Finite Element Analysis (FEA) model capable of introducing non-rigid elements within optimized folded cavity liners could provide a new mechanism to study non-locally reacting liners capable of reaching even lower frequencies.

The LFP factor could be extended to include mechanical properties. The addition of weights to the various parameters in the metric could emphasize importance on the most desired low-frequency performance characteristics.

Lastly, the Folded Cavity Packing Optimization Code could be further advanced so that at the end of the optimization process, nodal coordinates of the optimized liner could be directly exported to

3D CAD software so that the liner could be modeled quickly and accurately after the final optimized liner design is determined.

REFERENCES

[1] United States Environmental Protection Agency Noise Control Act, 42 U.S.C § 4901 et seq. (1972).

[2] European Parliament Directive 2002/49/EC, Declaration by the Commission in the Conciliation Committee on the Directive relating to the assessment and management of environmental noise, p. 12-25. (2002)

[3] Federal Aviation Administration, e-CFR Title 14, Chapter 1, Subchapter C, Part 36.

[4] NoiseQuest: Sources of Noise. (n.d.). Retrieved October 18, 2016.

[5] Perdue University, Noise Control (Suppression), (n.d.). Retrieved October 18, 2016.

[6] Charles E. Feiler and E. William Conrad. "Fan Noise from Turbofan Engines," Journal of Aircraft, Vol. 13, No. 2 (1976), pp. 128-134.

[7] Andrew Kempton. "Acoustic Liners for Modern Aero-Engines," Rolls-Royce. (2011)

[8] Rie Sugimoto et al. "Low-frequency liners for turbofan engines," Proceedings of the 20th International Congress on Acoustics. (2010)

[9] H. V. Helmholtz and A. J. Ellis. "On the sensations of tone as physiological bias for the theory of music," Dover Publications. (1954)

[10] Lydia Patton. "Hermann von Helmholtz," The Stanford Encyclopedia of Philosophy. (2016)

[11] G. Kirchhoff. "Ueber den Einfluss der Wärmeleitung in einem Gase auf die Schallbewegung," Ann. Phys., Vol. 210, Issue 6 (1868), pp. 177-193.

[12] Lord Rayleigh. “Theory of Sound: Volume II,” The MacMillan Co. (1896) pp. 319-326.

[13] D. E. Weston. “The Theory of the Propagation of Plane Sound Waves in Tubes,” Imperial College, London. (1953)

[14] C. Zwikker and C. W. Kosten. “Sound Absorbing Materials,” Elsevier. (1949)

[15] H. Tijdeman. “On the Propagation of Sound Waves in Cylindrical Tubes,” Journal of Sound and Vibration Vol. 39, No. 1 (1975), pp. 1-33

[16] R. A. Mangiarotty. “Acoustic-Lining Concepts and Materials for Engine Ducts,” The Journal of the Acoustical Society of America, Vol. 48, No. 3, (1970), pp. 783-794\

[17] R. A. Mangiarotty. “The Reduction of Aircraft Engine Fan-Compressor Noise Using Acoustic Linings,” Journal of Sound and Vibration Vol. 18, No. 1 (1971) pp. 553-576

[18] Ali H. Nayfeh et al. “Acoustics of Aircraft Engine-Duct Systems,” AIAA Journal Vol. 13, No. 2 (1975), pp. 130-153

[19] L. W. Dean. “Coupling of Helmholtz Resonators to Improve Acoustic Liners for Turbofan Engines at Low-frequency,” NASA CR-134912. (1975)

[20] Kenneth J. Baumeister. “Evaluation of Optimized Multisectioned Acoustic Liners,” AIAA Journal Vol. 17, No. 11 (1979) pp. 1185-1192

[21] O. Bschorr and E. Laudien. “The Silator-A Small Volume Resonator,” Journal of Sound and Vibration Vol. 158, No. 1 (1992) pp. 81-92

[22] Jia Yu and Eugene Chien. “Folding Cavity Acoustic Liner for Combustion Noise Reduction,” Proceedings of the 27th AIAA Aeroacoustics Conference. (2006)

[23] M. G. Jones, B. M. Howerton, and E. Ayle. “Evaluation of Parallel-Element, Variable-Impedance Broadband Acoustic Liner Concepts,” AIAA Journal. (2012)

[24] Tony L. Parrott and Michael G. Jones. “Parallel-element liner impedances for improved absorption of broadband sound in ducts,” Noise Control Engineering Journal Vol. 43, No. 6 (1995) pp. 183-195

[25] Hexcel. HexWeb® Acousti-Cap® Sound Attenuation Honeycomb. http://www.hexcel.com/Products/Honeycomb/HexWeb-Acousti-Cap (2017)

[26] Benjamin S. Beck, Noah H. Schiller, and Michael G. Jones. “Impedance assessment of a dual-resonance acoustic liner,” Applied Acoustics Vol. 93, (2105) pp. 15-22

[27] Le Fan et al. “An acoustic metamaterial composed of multi-layer membrane-coated perforated plates for low-frequency sound insulation,” Applied Physics Letters Vol. 106 .(2015)

[28] Guancong Ma et al. “Low-frequency narrow-band acoustic filter with large orifice,” Applied Physics Letters Vol. 103. (2013)

[29] Adam C. Slagle. “Low-frequency Noise Reduction using Novel Poro-Elastic Acoustic Metamaterials,” Master of Science Thesis, Virginia Polytechnic Institute and State University. (2014)

[30] Xiaoxiao Wu et al. “Low-frequency tunable acoustic absorber based on split tube resonators,” Applied Physics Letters Vol. 109. (2016)

[31] Yong Li and Badreddine M. Assouar. “Acoustic metasurface-based perfect absorber with deep subwaelength thickness,” Applied Physics Letters Vol. 108. (2016)

[32] Uno Ingard. “On the Theory and Design of Acoustic Resonators,” Journal of Acoustical Society of America. Vol. 25, No. 6 (1953) pp. 1037-1061

[33] J. J. Kelly and H. Abu-Khajeel. “A User’s Guide to the Zwikker-Kosten Transmission Line Code (ZKTL) ,” NASA CR-97-206901. (1997)

[34] J. C. Hanan, “Teardrop Lattice Structure for High Specific Strength Materials,” Patent Application No. 20120291618, Nov 22, (2012).

[35] Jeffrey R. Callicoat. “Evaluation of Composite Materials Providing Improved Acoustic Transmission Loss for UAVs,” Doctor of Philosophy Thesis, Oklahoma State University. (2016)

[36] ASTM E1050-12, “Standard Test Method for Impedance and Absorption of Acoustical Materials Using a Tube, Two Microphones and a Digital Frequency Analysis System.”

[37] ISO 10534-2: 1998, “Acoustics-Deterination of sound absorption coefficient and impedance in impedance tubes-Part 2: Transfer-function method.”

[38] Jones, M.G. and Parrott, T.L. “Evaluation of a multi-point method for determining acoustic impedance,” Journal of Mechanical Systems and Signal Processing, Vol. 3, No. 1 (1989) pp. 15-35.

[39] Chung, J.Y. and Blaser, D.A.: “Transfer function method of measuring in-duct acoustic properties: I. Theory,” Journal of Acoustical Society of America, Vol. 68, (1980) pp. 907-921.

[40] M. G. Jones et al. “Uncertainty and Sensitivity Analysis of a Two-Parameter Impedance Prediction Model,” 29th AIAA Aeroacoustics Conference. (2008)

[41] Watson, W., Jones, M., Tanner, S. and Parrott, T.: “Validation of a Numerical Method for Extracting Liner Impedance,” AIAA Journal Vol. 34 No. 3, (1996) pp. 548-554.

[42] U. Ingard and S. Labate, “Acoustic circulation effects and the nonlinear impedance of orifices,” Journal of the Acoustical Society of Vol. 22 (1950)

[43] Michael Jones, Tony Parrott, and Willie Watson, “Uncertainty and Sensitivity Analyses of a Two-Parameter Impedance Prediction Model,” Proceedings of the 29th AIAA Aeroacoustics Conference. (2008)

[44] Martha C. Brown, Michael G. Jones, and Willie R. Watson, “Uncertainty Analysis of the Grazing Flow Impedance Tube,” 18th AIAA/CEAS Aeroacoustics Conference. (2012)

APPENDICES

A.1 Impedance and Absorption Plots for the NIT Test Articles

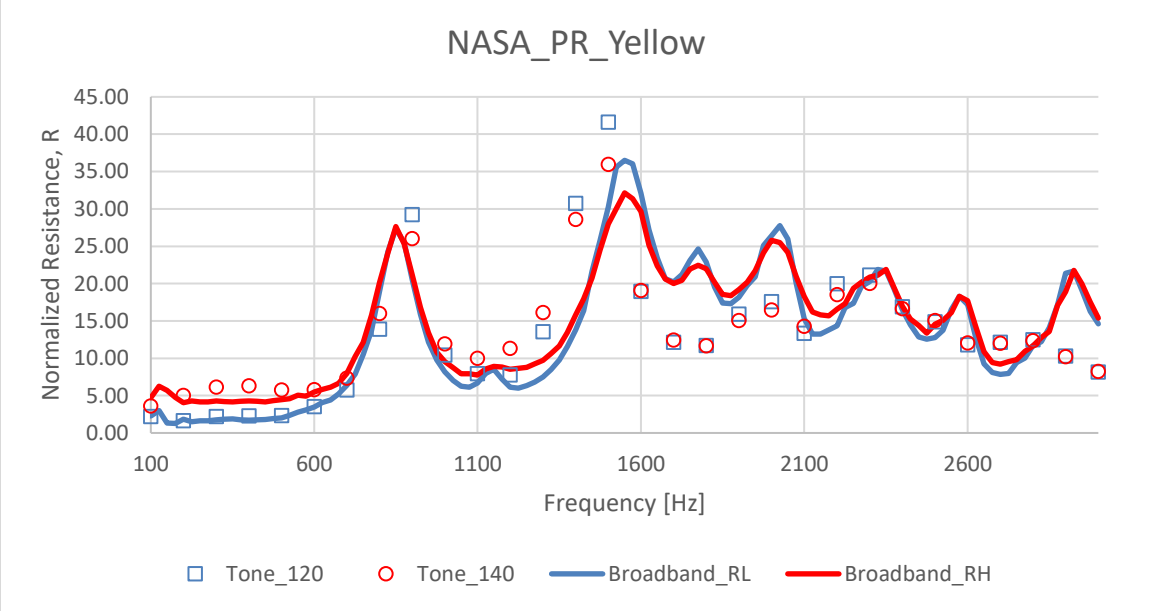

Figure A.1.1: Resistance spectrum for the PR_Yellow test article in the NASA NIT. Broadband and tone data shown at 120 dB (RL) and 140 dB (RH)

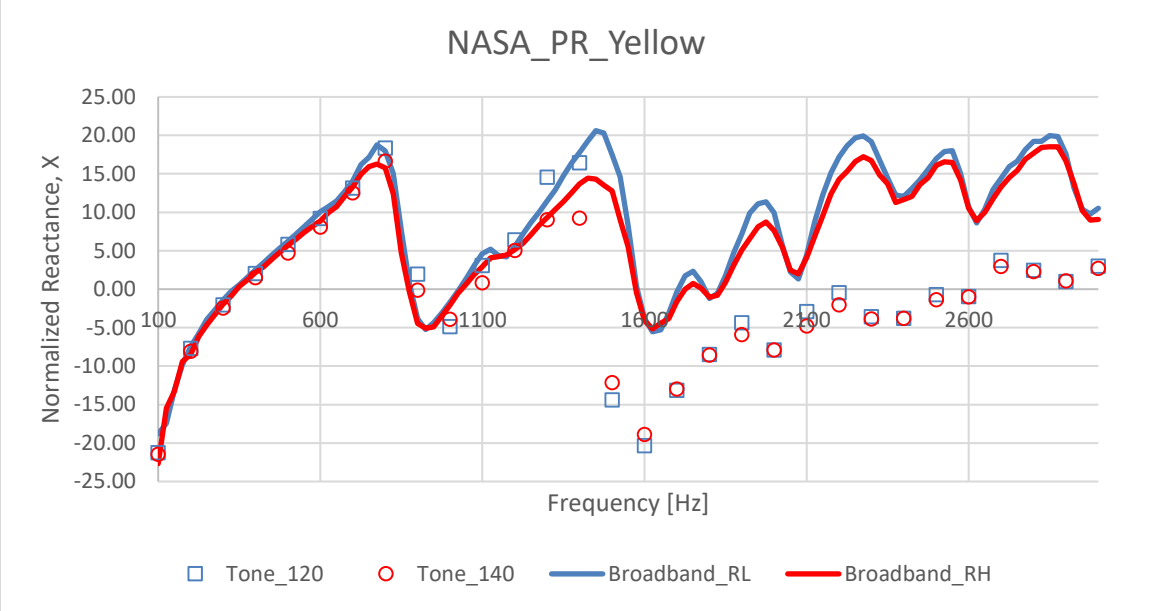

Figure A.1.2: Reactance spectrum for the PR_Yellow test article in the NASA NIT. Broadband and tone data shown at 120 dB (RL) and 140 dB (RH)

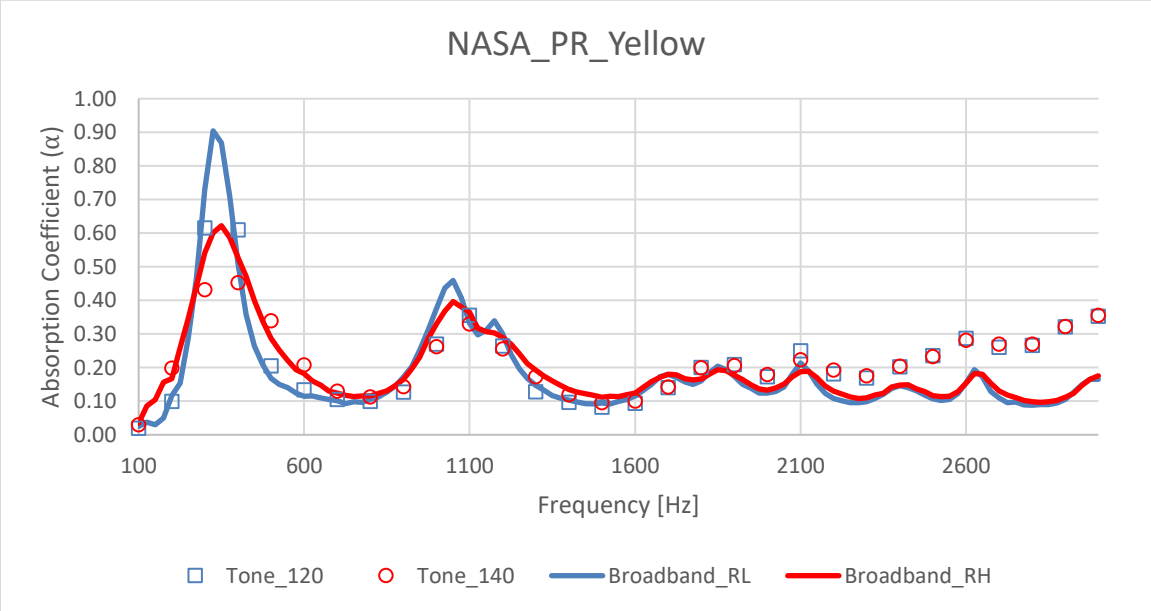

Figure A.1.3: Absorption coefficient spectrum for the PR_Yellow test article in the NASA NIT. Broadband and tone data shown at 120 dB (RL) and 140 dB (RH)

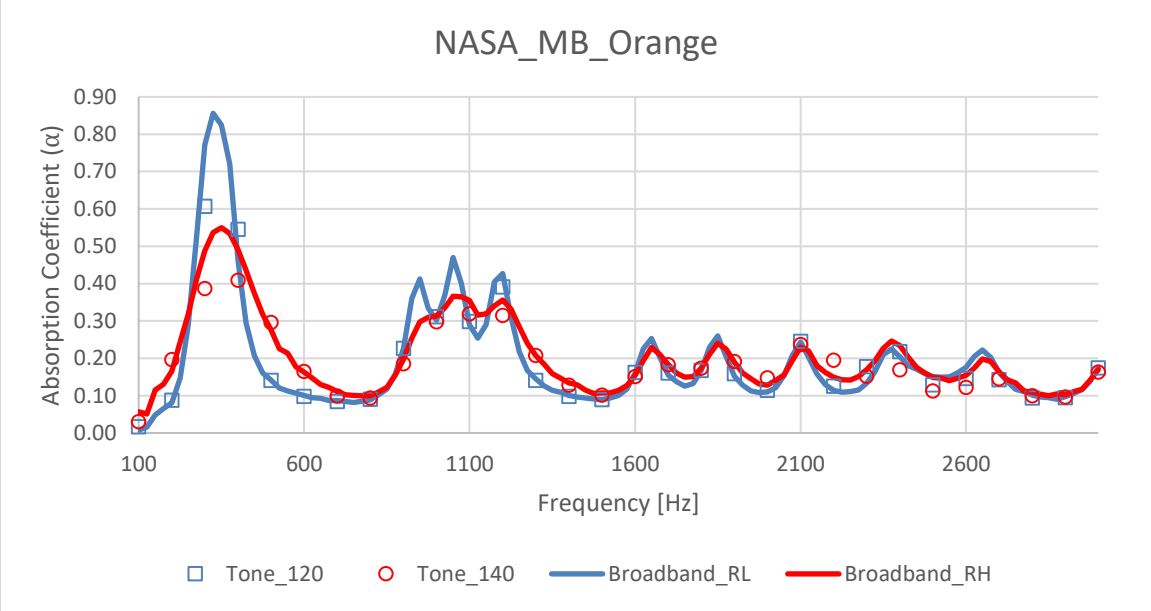

Figure A.1.4: Absorption coefficient for the MB_Orange test article in the NASA NIT. Broadband and tone data shown at 120 dB (RL) and 140 dB (RH)

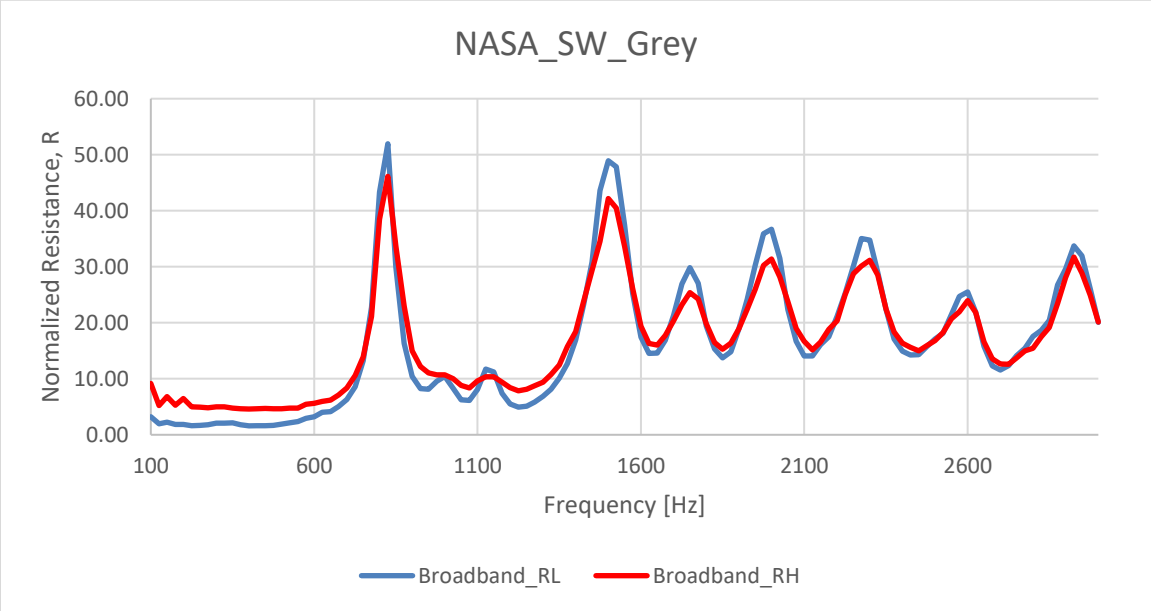

Figure A.1.5: Resistance spectrum for the SW_Grey test article in the NASA NIT. Broadband and tone data shown at 120 dB (RL) and 140 dB (RH)

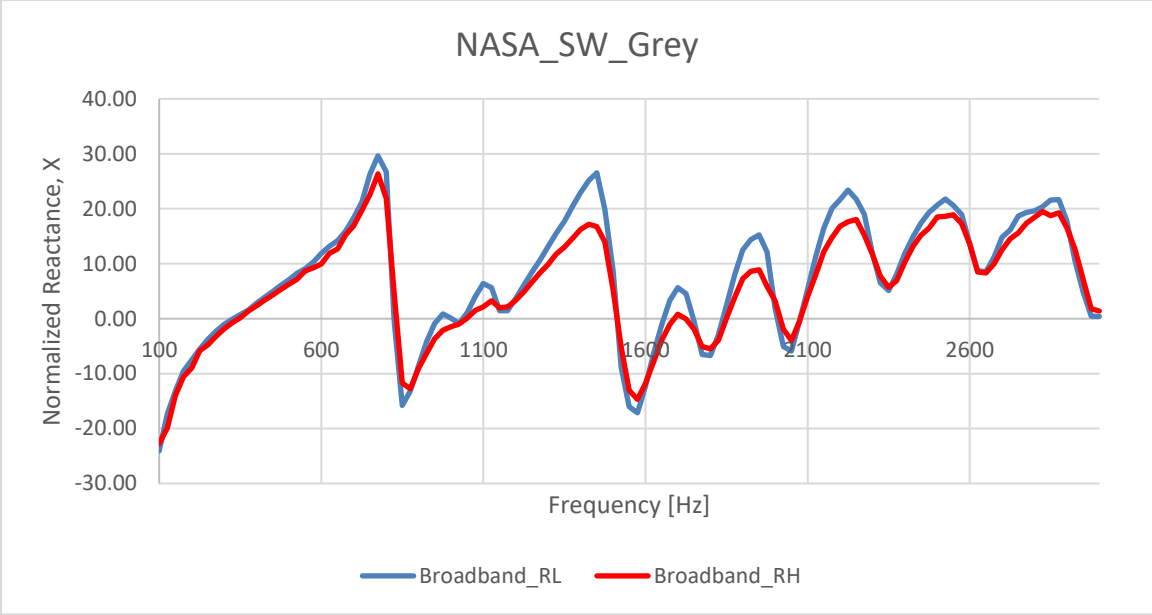

Figure A.1.6: Reactance spectrum for the SW_Grey test article in the NASA NIT. Broadband and tone data shown at 120 dB (RL) and 140 dB (RH)

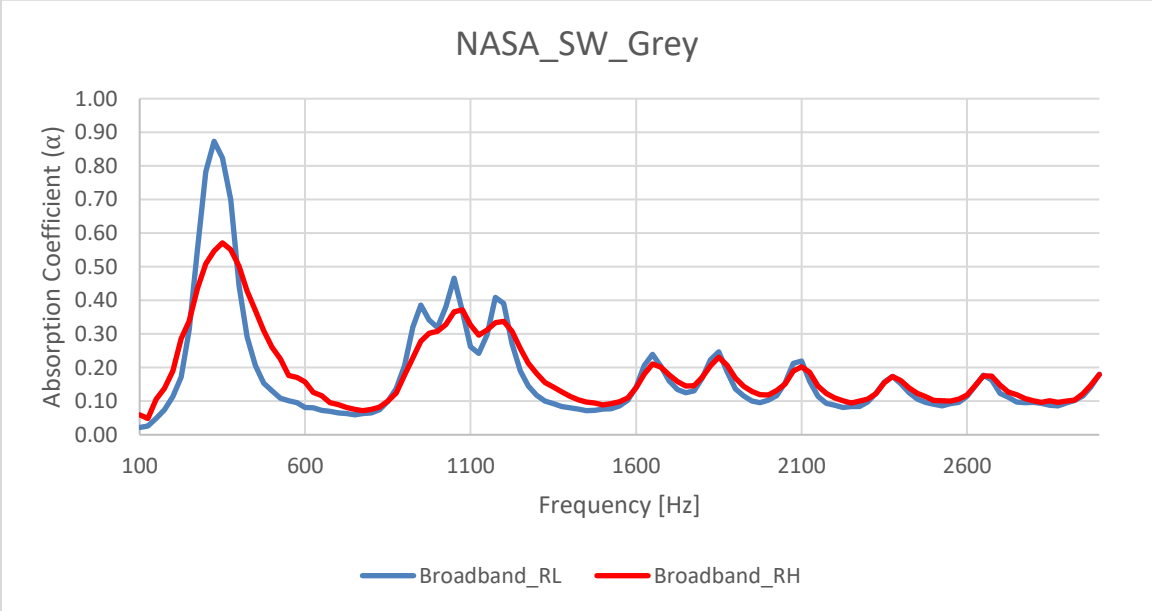

Figure A.1.7: Absorption coefficient spectrum for the SW_Grey test article in the NASA NIT. Broadband and tone data shown at 120 dB (RL) and 140 dB (RH)

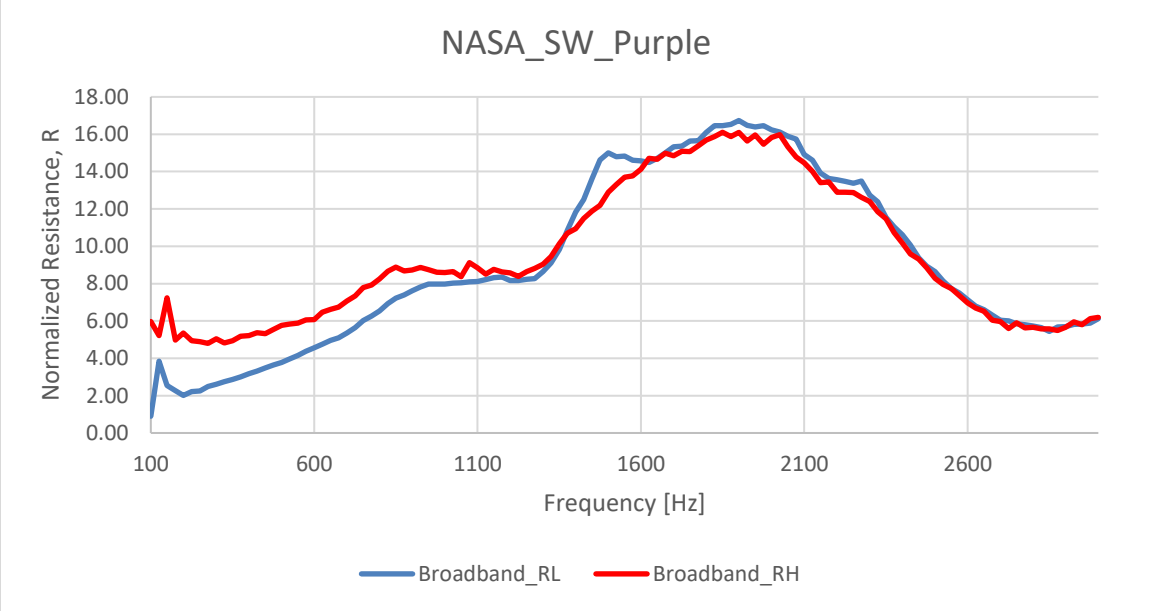

Figure A.1.8: Resistance spectrum for the SW_Purple test article in the NASA NIT. Broadband and tone data shown at 120 dB (RL) and 140 dB (RH)

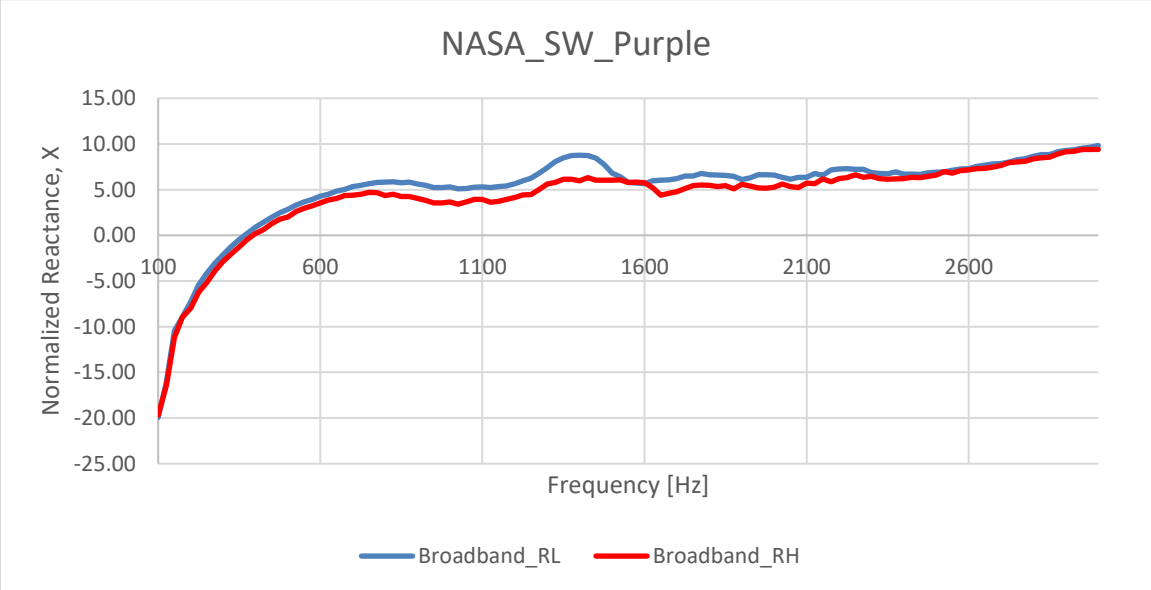

Figure A.1.9: Reactance spectrum for the SW_Purple test article in the NASA NIT. Broadband and tone data shown at 120 dB (RL) and 140 dB (RH)

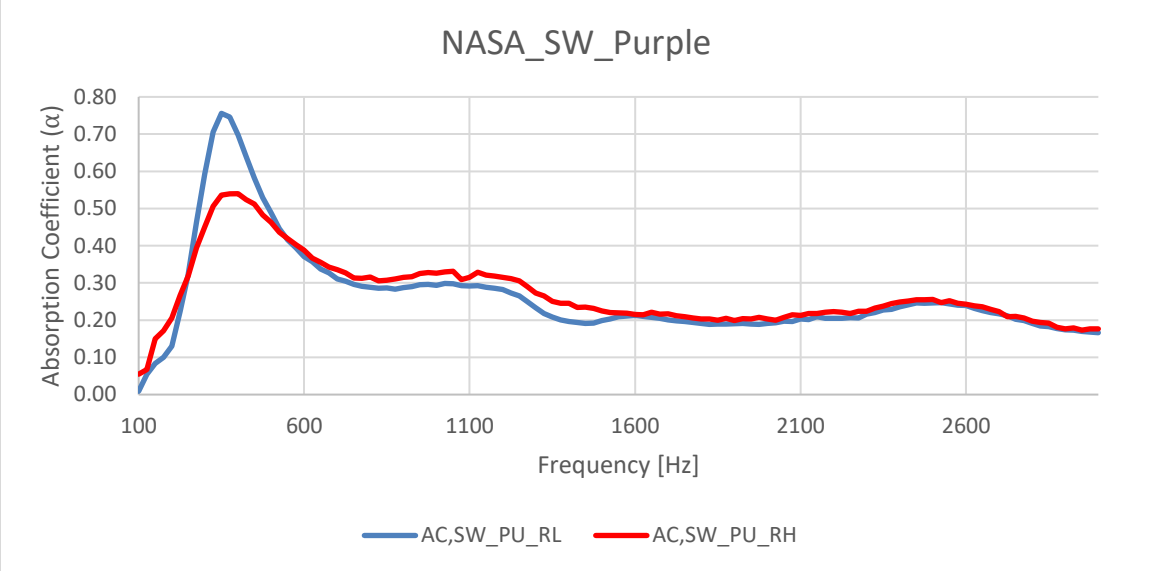

Figure A.1.10: Absorption coefficient spectrum for the SW_Purple test article in the NASA NIT. Broadband and tone data shown at 120 dB (RL) and 140 dB (RH)

A.2 Error Estimation

In order to quantify the reliability of the experimental data presented, an error estimation study was conducted. Repeatability (same test article, same impedance tube), fabrication error (same liner design, different fabrication methods), and propagation of error through the eduction process were explored further using the Optimized 3D Folded Cavity Liner design test articles.

A.2.1 Estimation of Repeatability Error

For the repeatability study, three separate OSU NIT trials for each of the three test articles (MB_Orange, PR_Yellow, and SW_Grey) were compared. The average in the absorption coefficient spectrum in the low-frequency range for the three trials of each of the test articles was calculated, then the maximum and minimum absorption coefficient measured at each frequency for the three trials is shown using error bars.

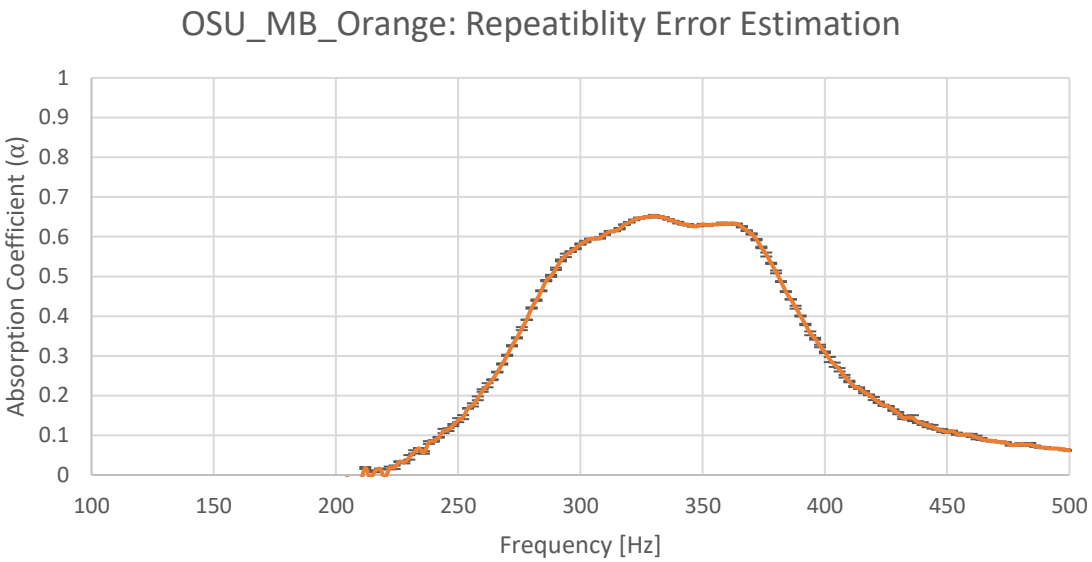

Figure A.2.1: Average absorption coefficient spectrum from three trials for the MB_Orange test article in the OSU NIT with error bars representing maximum and minimum absorption deviation from the average.

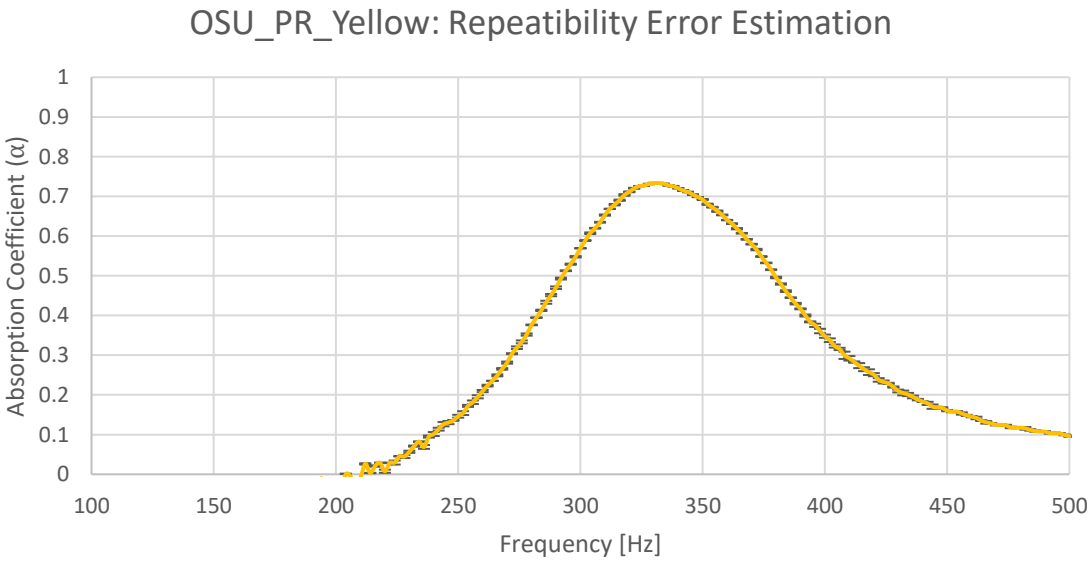

Figure A.2.2: Average absorption coefficient spectrum from three trials for the PR_Yellow test article in the OSU NIT with error bars representing maximum and minimum absorption deviation from the average.

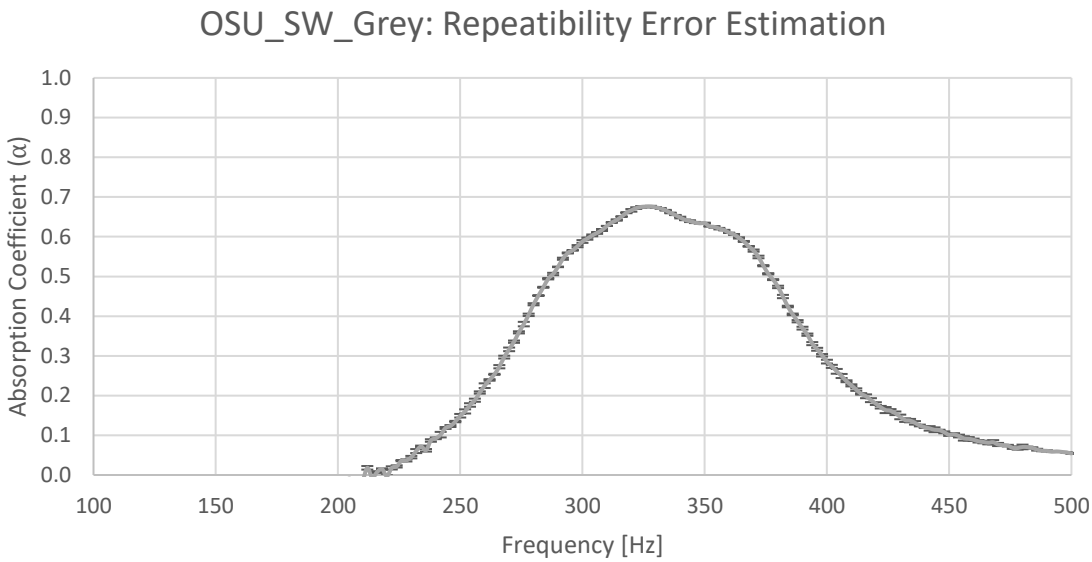

Figure A.2.3: Average absorption coefficient spectrum from three trials for the SW_Grey test article in the OSU NIT with error bars representing maximum and minimum absorption deviation from the average.

Maximum deviation in the absorption coefficient spectrum for the three trials for each of the three test articles lies well within the repeatability error intervals specified by ASTM 1050 [36]. In the resonance bandwidth (~275 Hz - ~400 Hz), the percent error between repeated trials for each of the three test articles is less than 1.7%. Therefore, there is very little error in the experimental absorption coefficient data attributable to variations between trials in the OSU normal incidence impedance tube, indicating excellent repeatability.

A.2.2 Effect of Fabrication Process

For the estimation of error due to the fabrication processes, the absorption coefficient spectrums for the MB_Orange, PR_Yellow, and SW_Grey test articles were averaged together, for the three separate NIT tests (OSU, NASA 120 dB, and NASA 140 dB). The maximum and minimum absorption coefficient measured at each frequency from among these three test articles for each

test is shown using error bars. Thus, the error induced in the absorption coefficient spectrum due to variations between test articles arising from fabrication methods could be quantified.

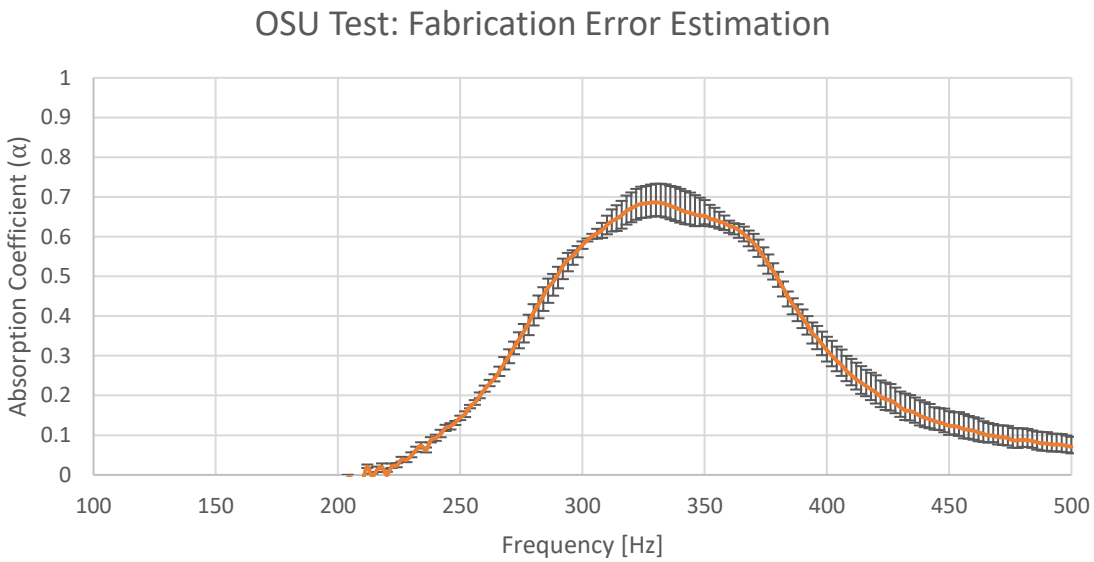

Figure A.2.4.: Average absorption coefficient spectrum for the three different test articles in the OSU NIT with error bars representing maximum and minimum absorption measured from among the three test articles.

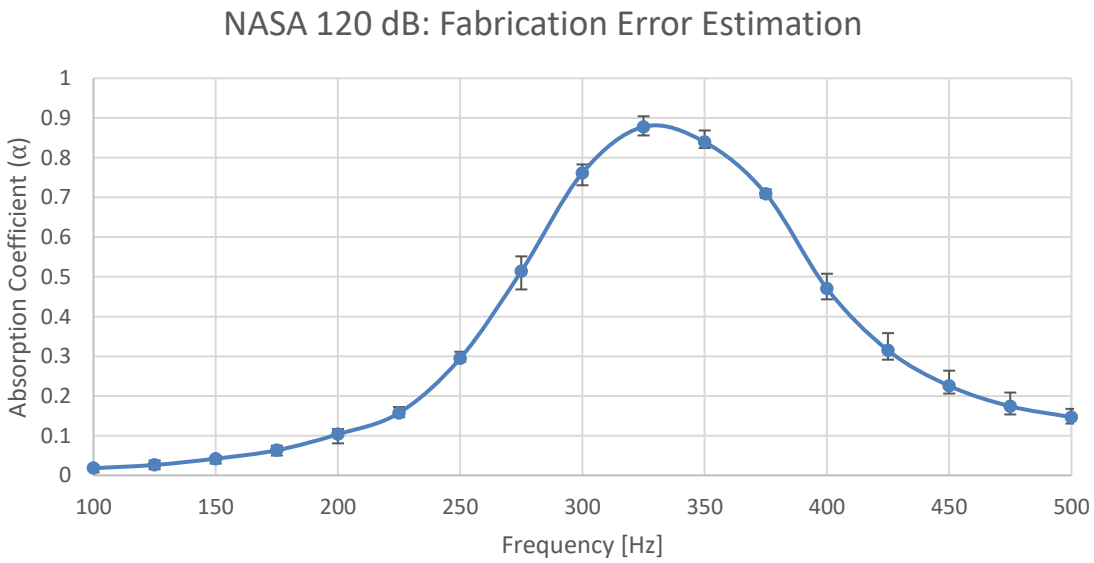

Figure A.2.5.: Average absorption coefficient spectrum for the three different test articles in the NASA NIT at 120 dB, with error bars representing maximum and minimum absorption measured from among the three test articles.

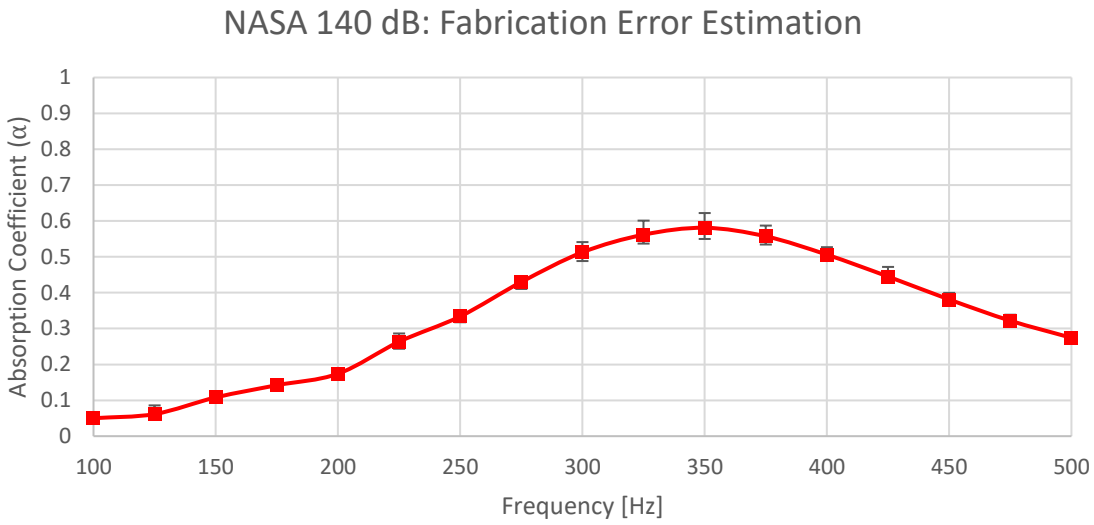

Figure A.2.6.: Average absorption coefficient spectrum for the three different test articles in the NASA NIT at 140 dB, with error bars representing maximum and minimum absorption measured from among the three test articles.

Results show that the amount of error introduced in the absorption spectrum due to fabrication differences is higher than the error shown from the repeatability study. The maximum error in absorption magnitude is seen near the peak location for all three tests indicating a resonant effects-driven contribution. For the three samples in the OSU tube, the maximum error due to fabrication in the resonance bandwidth of 275 Hz – 400 Hz is $\alpha \pm 12.3\%$. In the NASA tube at 120 dB, the maximum fabrication error in the same resonance bandwidth is $\alpha \pm 9\%$. Lastly, in the NASA tube at 140 dB, in the same resonance bandwidth, the maximum fabrication error is $\alpha \pm 7\%$. Thus, the fabrication error has a more significant effect on the measured absorption coefficient than the repeatability error which is expected owing to the irregularities in the 3D printing process.

A.2.3 Propagation of Error Through Eduction Process

To estimate the error introduced in the absorption coefficient spectrum when the measured SPL is slightly off, the measured SPL levels from the two microphones used in the OSU impedance tube are varied slightly for the MB_Orange test article test. The microphone pressures are uniformly varied by $\pm 2\%$ of their measured values, and the resulting absorption coefficient spectrums are compared. 2% was chosen to represent a reasonable potential error from microphone SPL measurements based on the analysis of the repeatability errors from multiple trials.

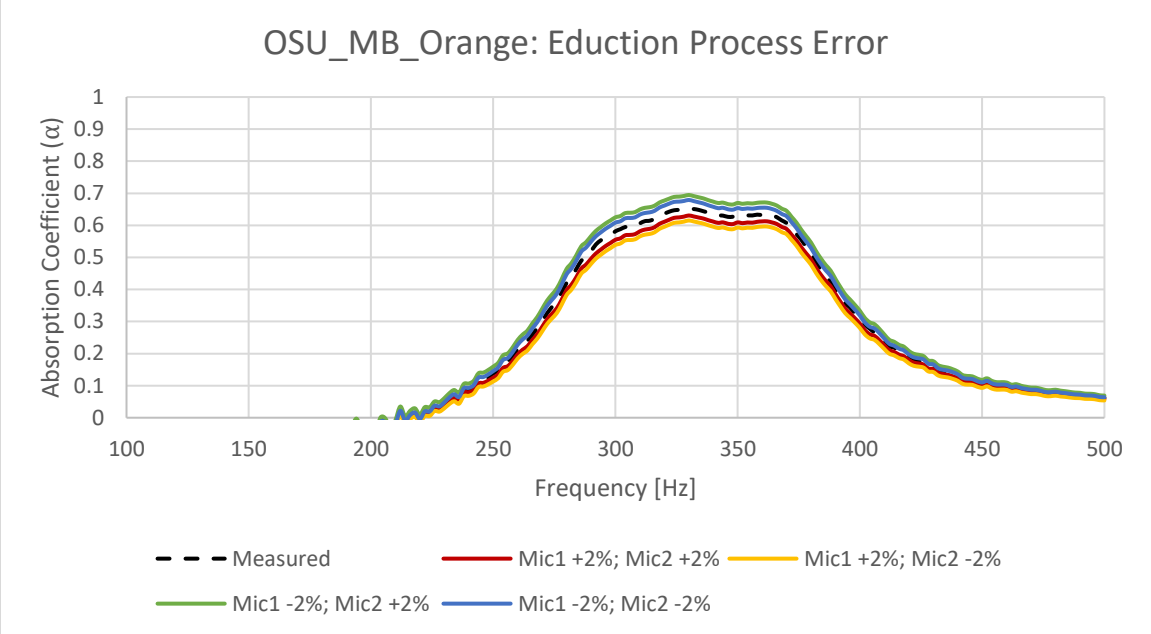

Figure A.2.7.: Educed absorption coefficient spectrum of the MB_Orange test article from the OSU NIT, with ±2% change in measured sound pressure from the two microphones.

Results show that the absorption coefficient spectrum changes noticeably only in the resonance bandwidth when the input measured pressures are varied $\pm 2\%$. A combination of positive and negative variation (one microphone +2% with the other -2%) gives a larger deviation from the

measured absorption than when both microphones are varied the same (both +2% or both -2%). The maximum percent deviation in the absorption coefficient spectrum for each of the four cases within the 275 Hz – 400 Hz resonance bandwidth is given below. Thus, a combination of small but opposite error trends in the two mics could result in the greatest amplification of the propagated error in the educed absorption coefficient.

Case	Max % deviation in α
Mic1 +2%; Mic2 +2%	7.4%
Mic1 +2%; Mic2 -2%	11.4%
Mic1 -2%; Mic2 +2%	10.5%
Mic1 -2%; Mic2 -2%	6.4%

A.3 3D Folded Cavity Packing Optimization Code

Note: Modular sections of the 3D Folded Cavity Packing Optimization Code are given here, instead of the full code implemented in the spreadsheet tool.

Inputs

```
l=Excel["F7"];
width=Excel["G7"];
h=Excel["H7"]*0.0254;
beta=Excel["G10"];
mue=Excel["G11"];
targetf=Excel["G12"];
minthickness=Excel["F15"];
numcellslength=Excel["G15"];
numcellswidth=Excel["H15"];
numcells=numcellslength*numcellswidth;
maxmass=Excel["H20"];
nfr=250;

thresh=Excel["G11"];
t0=273;
c0=331;
gamma=1.402;
dcold=0;
psi=Excel["F18"];
tk=Excel["G18"];
```

Cavity Size and Aspect Ratio

```
d1=((width*0.0254)-((numcellswidth+1)*minthickness/1000))/(numcellswidth);
d2=((l*0.0254)-((numcellslength+1)*minthickness/1000))/(numcellslength);

If[d1<d2, {d=d1, asp=d2/d1}, {d=d2, asp=d1/d2}];
Excel["B9"]=asp;
Excel["B8"]=d;
```

Potential Cavity Lengths

```
firstcell=(h)-(minthickness/1000)-(d/2);
lastcell=(h)-(2*minthickness/1000)-(d/2);
midcell=(h)-(2*minthickness/1000)-d;
center=d+(minthickness/1000);

L1=firstcell;
```

```
L2=firstcell+lastcell+(1*center);
L3=firstcell+(1*midcell)+lastcell+(2*center);
L4=firstcell+(2*midcell)+lastcell+(3*center);
L5=firstcell+(3*midcell)+lastcell+(4*center);
L6=firstcell+(4*midcell)+lastcell+(5*center);
L7=firstcell+(5*midcell)+lastcell+(6*center);
L8=firstcell+(6*midcell)+lastcell+(7*center);
L9=firstcell+(7*midcell)+lastcell+(8*center);
L10=firstcell+(8*midcell)+lastcell+(9*center);
L11=firstcell+(9*midcell)+lastcell+(10*center);
L12=firstcell+(10*midcell)+lastcell+(11*center);
ExcelWrite["K40",L1];
ExcelWrite["K41",L2];
ExcelWrite["K42",L3];
ExcelWrite["K43",L4];
ExcelWrite["K44",L5];
ExcelWrite["K45",L6];
ExcelWrite["K46",L7];
ExcelWrite["K47",L8];
ExcelWrite["K48",L9];
ExcelWrite["K49",L10];
ExcelWrite["K50",L11];
ExcelWrite["K51",L12];
Ltab=ExcelRead["K40:K51"];
```

Configuration Possibilities

```
configuration={};
wallstop=2/1000;
xmin=(d/2);
xmax=midcell-(d/2)-wallstop;
deltax=(xmax-xmin)/9;
Lxtab={};
Lytab={};
LFP2={};
config2={};
mca={}; (*middle cluster array*)
betaarray={};
Marray={};
zetaarray={};
quantity1={};
quantity2={};
quantity3={};
ExcelWrite["D6", 1];
Do[
```

```
config={{0,0,0},{0,0,0}};
M=0;
bandwidth=0;
low=1;
high=1;
LFP=0;
ExcelClear["D40:D289"]
        Do[
                Do[
                z=(x-1)*(i-y)+(x*i)+(x+1)*(i-y);
                If[ z==numcells, config={{x-1,x,x+1},{i-y,i,i-y}}];
                If[ z==numcells,
                clus1=x-1; (*cluster number*)
                clus2=x;
                clus3=x+1;
                quan1=i-y; (*Quantity*)
                quan2=i;
                quan3=i-y; ];

                ,{y,0,1,1}];
        ,{i,1,12,1}];
configuration=Append[configuration,config];
If[clus2==2, ExcelWrite["B10",L1]; ExcelWrite["B16",L2]; ExcelWrite["B22",L3];
ExcelWrite["C6",quan1]; ExcelWrite["C12",quan2];  ExcelWrite["C18",quan3]; ];
If[clus2==3, ExcelWrite["B10",L2]; ExcelWrite["B16",L3]; ExcelWrite["B22",L4];
ExcelWrite["C6",quan1]; ExcelWrite["C12",quan2];  ExcelWrite["C18",quan3]; ];
If[clus2==4, ExcelWrite["B10",L3]; ExcelWrite["B16",L4]; ExcelWrite["B22",L5];
ExcelWrite["C6",quan1]; ExcelWrite["C12",quan2];  ExcelWrite["C18",quan3]; ];
If[clus2==5, ExcelWrite["B10",L4]; ExcelWrite["B16",L5]; ExcelWrite["B22",L6];
ExcelWrite["C6",quan1]; ExcelWrite["C12",quan2];  ExcelWrite["C18",quan3]; ];
If[clus2==6, ExcelWrite["B10",L5]; ExcelWrite["B16",L6]; ExcelWrite["B22",L7];
ExcelWrite["C6",quan1]; ExcelWrite["C12",quan2];  ExcelWrite["C18",quan3]; ];
If[clus2==7, ExcelWrite["B10",L6]; ExcelWrite["B16",L7]; ExcelWrite["B22",L8];
ExcelWrite["C6",quan1]; ExcelWrite["C12",quan2];  ExcelWrite["C18",quan3]; ];
If[clus2==8, ExcelWrite["B10",L7]; ExcelWrite["B16",L8]; ExcelWrite["B22",L9];
ExcelWrite["C6",quan1]; ExcelWrite["C12",quan2];  ExcelWrite["C18",quan3]; ];
If[clus2==9, ExcelWrite["B10",L8]; ExcelWrite["B16",L9]; ExcelWrite["B22",L10];
ExcelWrite["C6",quan1]; ExcelWrite["C12",quan2];  ExcelWrite["C18",quan3]; ];
If[clus2==10, ExcelWrite["B10",L9]; ExcelWrite["B16",L10]; ExcelWrite["B22",L11];
ExcelWrite["C6",quan1]; ExcelWrite["C12",quan2];  ExcelWrite["C18",quan3]; ];
If[clus2==11, ExcelWrite["B10",L10]; ExcelWrite["B16",L11]; ExcelWrite["B22",L12];
ExcelWrite["C6",quan1]; ExcelWrite["C12",quan2];  ExcelWrite["C18",quan3]; ];
If[clus2==12, ExcelWrite["B10",L11]; ExcelWrite["B16",L12]; ExcelWrite["B22",L13];
ExcelWrite["C6",quan1]; ExcelWrite["C12",quan2];  ExcelWrite["C18",quan3]; ];
midcav=ExcelRead["B16"];
```

Sub-Integral Cavity Length Determination

```
Do[
(*change x as a % of the midcell length, y will change accordingly*)
y=midcell-xx-wallstop;
Lx=Ltab[[clus2-1]]-(d/2)+center+xx; (*upper frequency length*)
Ly=Ltab[[clus2]]-(d/2)+center+y;(*lower frequency length*)
ExcelWrite["B10", Ly];
ExcelWrite["B22", Lx];

ExcelSave["Liner Optimization8.xlsm"];
(*At this point the code runs the ZKTL portion of the code, shown below in blue. It also
calculated the LFP, which is also shown below*)
```

ZKTL Portion of the Code (Based on the code by NASA)

```
        t0=273;
        c0=331;
        gamma=1.402;
        dcold=0;
        psi=Excel["F18"];
        tk=Excel["G18"];
        indata=Import["/Users/Andrew/Documents/Research/Misc/Liner Optimization/Liner
Optimization6.xlsm"];
        sa=l*width*(0.0254^2);
        LFP=beta*mue/upsilon;
        iae = 0;
        mu[t_] := ((1.183*t^3)/10^7 - (3.808*t^2)/10^4 + 0.6738*t + 13.554)/10^7;
        σ = (-((5.232*tk^3)/10^10) + (1.234*tk^2)/10^6 - (8.488*tk)/10^4 + 0.865)^0.5;
        c = c0*Sqrt[tk/t0];
        ρ = (6895.*psi)/(287.6*tk);
        ftab = {};
        ztab = {};
        Do[
        freq = indata[[1,ifr+39,1]];
        ω = 2*Pi*freq;
        k = ω/c;
        betat = 0; nset = indata[[1,5,2]];

        Do[
        betabp = indata[[1,ifr+39,2]] + I*indata[[1,ifr+39,3]];
        {{p1}, {u1}} = {{1}, {1*betabp}};
        nc = indata[[1,6*(iset - 1) + 6,3]];
        nlay = indata[[1,6*(iset - 1) + 6,4]];
```

```
Do[
itype = indata[[1,6*(iset - 1) + 7, ilay + 1]];
asprat = indata[[1, 6*(iset - 1) + 9,ilay + 1]];
tmp = indata[[1,6*(iset - 1) + 8, ilay + 1]];
If[Abs[asprat - 1] < 0.001,
dc = tmp, {wc = asprat*tmp,
dc = (4*(tmp*wc))/(2*(tmp + wc))}];
lc = indata[[1,6*(iset - 1) + 10, ilay + 1]];
rf = (mu[tk]*indata[[1, 6*(iset - 1) + 11,ilay + 1]])/mu[t0 + (5*(70 - 32))/9];

If[ilay > 1 && Abs[dc - dcold] > 1/10^10,
{u1 = u1*(dcold/dc)^2}];
If[itype == 1,
{s = (1/2)*dc*Sqrt[(ρ*ω)/mu[tk]],
        Γ = Sqrt[(gamma*BesselJ[0, I^1.5*s]*(1 + ((gamma - 1)*BesselJ[2,
I^1.5*σ*s])/(gamma*BesselJ[0, I^1.5*σ*s])))/BesselJ[2, I^1.5*s]],
        zc = -((I*BesselJ[0, I^1.5*s])/(Γ*BesselJ[2, I^1.5*s])),
        If[iae != 0, {zc = Re[zc], Γ = I}],
        t11 = Cosh[Γ*k*lc],
t12 = zc*Sinh[Γ*k*lc],
t21 = Sinh[Γ*k*lc]/zc}];
If[itype == 2,
{t11 = 1,
t12 = rf/(c*ρ),
t21 = 0}];
If[itype == 3, {r1 = rf/lc,
        Γ = 0.189/((freq*ρ)/r1)^0.593 + I*(0.0978/((freq*ρ)/r1)^0.7 + 1),
        zc = (0.0571/((freq*ρ)/r1)^0.754 + 1) - (I*0.087)/((freq*ρ)/r1)^0.732,
        t11 = Cosh[Γ*k*lc],
t12 = zc*Sinh[Γ*k*lc],
t21 = Sinh[Γ*k*lc]/zc}];
{{p2}, {u2}} = {{t11, t12}, {t21, t11}} . {{p1}, {u1}};
{{p1}, {u1}} = {{p2}, {u2}};
dcold = dc,
{ilay, 1, nlay, 1}];
betac = u2/p2;
asprat = indata[[1,6*(iset - 1) + 9,nlay + 1]];
tmp = indata[[1,6*(iset - 1) + 8,nlay + 1]];
If[Abs[asprat - 1] < 0.001,
{dc = tmp,
 sigmac = (Pi*dc^2)/(4*sa)},
{wc = asprat*tmp, sigmac = (tmp*wc)/sa}];
betat = betac*nc*sigmac + betat,
{iset, 1, nset, 1}];
```

```
ftab = Append[ftab, freq];
ztab = Append[ztab, 1/betat],
{ifr, 1, nfr, 1}]
ftab;
ztab;
res = Table[{ftab[[i]], Re[ztab][[i]]}, {i, 1, nfr}];
rea = Table[{ftab[[i]], Im[ztab][[i]]}, {i, 1, nfr}];
ac = Table[(4*Re[ztab][[i]])/((Re[ztab][[i]] + 1)^2 + Im[ztab][[i]]^2), {i, 1, nfr}];

ExcelWrite["D40:D289",ac]
```

LFP Calculation

```
If[ac[[i]] > thresh, {low = ftab[[i]], Break[]}];

,{i,1,nfr-1}];
Do[
If[ac[[i]] > thresh && ac[[i+1]] < thresh, {high=ftab[[i]], Break[]}];
,{i,1,nfr-1}];
If[ac[[250]]>thresh && high==1, high=500];

bandwidth=high-low;
Excel["K7"]=bandwidth;
Excel["K9"]=low;
M=Excel["K8"];
LFP=(bandwidth*M)*100/low;
Excel["K10"]=LFP;
If[configuration[[x]]=={{0,0,0},{0,0,0}}, LFP=0];

LFP2=Append[LFP2,LFP];
config2=Append[config2, config];
Lxtab=Append[Lxtab, Lx];
Lytab=Append[Lytab,Ly];
mca=Append[mca, midcav];
betaarray=Append[betaarray, bandwidth];
Marray=Append[Marray, M];
zetaarray=Append[zetaarray, low];
quantity1=Append[quantity1, quan1];
quantity2=Append[quantity2, quan2];
quantity3=Append[quantity3, quan3];

,{xx,xmin,xmax,deltax}];
,{x,1,12,1}];
```

Determine best configuration and output the no face sheet case

```
config2;
ExcelWrite["J36:J155", config2];
LFP2;
ExcelWrite["K36:K155", Lxtab];
Lxtab;
ExcelWrite["L36:L155", mca];
Lytab;
ExcelWrite["M36:M155", Lytab];
mca;
ExcelWrite["N36:N155", betaarray];
betaarray;
ExcelWrite["O36:O155", Marray];
Marray;
ExcelWrite["P36:P155", zetaarray];
zetaarray;
ExcelWrite["Q36:Q155", LFP2];
(*Find Best Configuration From LFP*)
maxLFP=Max[LFP2];
Do[
If[LFP2[[i]] == maxLFP, maxloc=i];
,{i,1,120}];
(*Set final config*)
Llow=Lytab[[maxloc]];
Lhigh=Lxtab[[maxloc]];
Lmid=mca[[maxloc]];
finconfig=config2[[maxloc]];
finalbeta=betaarray[[maxloc]];
finalM=Marray[[maxloc]];
finalzeta=zetaarray[[maxloc]];
q1=quantity1[[maxloc]];
q2=quantity2[[maxloc]];
q3=quantity3[[maxloc]];
Llowin=Llow/0.0254;
Lmidin=Lmid/0.0254;
Lhighin=Lhigh/0.0254;
ExcelWrite["B10", Llow];
ExcelWrite["B16", Lmid];
ExcelWrite["B22", Lhigh];
ExcelWrite["C6", q1];
ExcelWrite["C12", q2];
ExcelWrite["C18", q3];
ExcelWrite["K16", Llowin];
ExcelWrite["L16", Lmidin];
```

```
ExcelWrite["M16", Lhighin];
ExcelWrite["J16", finconfig];
ExcelWrite["K19", finalbeta];
ExcelWrite["L19", finalM];
ExcelWrite["M19", finalzeta];
ExcelWrite["N19", maxLFP];
(*Output no face sheet case*)
ExcelWrite["D6", 2];
ExcelSave["Liner Optimization8.xlsm"]; (*File name must be changed to this current file name
before running*)
faceholed={};
LFPface={};
betaface={};
Mface={};
zetaface={};
M=0;
bandwidth=0;
low=1;
high=1;
LFP=0;

Determine optimum face sheet

hole=h/1000;
If[hole<d, ExcelWrite["C8", hole];
ExcelSave["Liner Optimization8.xlsm"];


(* Run ZKTL portion*)

Calculate final LFP and output final design

If[ac[[i]] > thresh, {low = ftab[[i]], Break[]}];
,{i,1,nfr-1}];
Do[
If[ac[[i]] > thresh && ac[[i+1]] < thresh, {high=ftab[[i]], Break[]}];
,{i,1,nfr-1}];
If[ac[[250]] > thresh && high==1, high=500];

bandwidth=high-low;
Excel["K7"]=bandwidth;
Excel["K9"]=low;
M=Excel["K8"];
LFP=(bandwidth*M)*100/low;
Excel["K10"]=LFP;
```

```
LFPface=Append[LFPface, LFP];
betaface=Append[betaface, bandwidth];
Mface=Append[Mface, M];
zetaface=Append[zetaface, low];
faceholed=Append[faceholed, h];
 , LFPface=Append[LFPface, 0];
betaface=Append[betaface, 0];
Mface=Append[Mface, 0];
zetaface=Append[zetaface, 0];
faceholed=Append[faceholed, 0];
];

,{h,1,7,0.5}];
ExcelWrite["J20:J32", faceholed];
ExcelWrite["K20:K32", betaface];
ExcelWrite["L20:L32", Mface];
ExcelWrite["M20:M32", zetaface];
ExcelWrite["N20:N32", LFPface];
(*Find final design*)
maxLFPface=Max[LFPface];
Do[
If[LFPface[[i]] == maxLFPface, maxloca=i];
,{i,1,13}];
finalfaced=faceholed[[maxloca]];
finalfacemm=finalfaced/1000;
finalbeta=betaface[[maxloca]];
finalM=Mface[[maxloca]];
finalzeta=zetaface[[maxloca]];
finalLFP=LFPface[[maxloca]];
(*final output*)
ExcelWrite["K7", finalbeta];
ExcelWrite["K8", finalM];
ExcelWrite["K9", finalzeta];
ExcelWrite["K10", finalLFP];
ExcelWrite["C8", finalfacemm];
ExcelSave["Liner Optimization8.xlsm"];
```

VITA

Andrew T. Chambers

Candidate for the Degree of

Master of Science

Thesis: DEVELOPMENT OF LIGHTWEIGHT, COMPACT, STRUCTURALLY-INTEGRATED ACOUSTIC LINERS FOR BROADBAND LOW-FREQUENCY NOISE MITIGATION.

Major Field: Mechanical and Aerospace Engineering

Biographical:

Education:

Completed the requirements for the Master of Science in Mechanical and Aerospace Engineering at Oklahoma State University, Stillwater, Oklahoma in May, 2017.

Completed the requirements for the Bachelor of Science in Mechanical Engineering at Oklahoma State University, Stillwater, Oklahoma in May, 2015.

Experience:

Research Assistant — August 2015 – May 2017
Oklahoma State University
Stillwater, OK

Engineering Intern — May 2015 - August 2015
Northwest Crane Service — May 2014 - August 2014
Oklahoma City, OK

Professional Memberships:

AIAA Member